DISSERTATION

Temperature Dependence of Carrier Lifetime, Recombination, and Gain in 1.3 μm InAsP/InGaAsP Multiple Quantum Well Lasers

Submitted by

Jon M. Pikal

Electrical Engineering

In Partial fulfillment of the requirements

for the Degree of Doctor of Philosophy

Colorado State University

Fort Collins, Colorado

Fall 1999

UMI Number: 9950905

Bell & Howell Information and Learning Company
300 North Zeeb Road
P.O. Box 1346
Ann Arbor, MI 48106-1346

COLORADO STATE UNIVERSITY

AUGUST 16, 1999

WE HEREBY RECOMMEND THAT THE DISSERTATION PREPARED UNDER OUR SUPERVISION BY JON M. PIKAL ENTITLED TEMPERATURE DEPENDENCE OF CARRIER LIFETIME, RECOMBINATION AND GAIN IN 1.3 μM InAsP/InGaAsP MULTIPULE QUANTUM WELL LASERS BE ACCEPTED AS FULFILLING IN PART REQUIREMENTS FOR THE DEGREE OF DOCTOR OF PHILOSOPHY.

Committee on Graduate Work

James R. Sites

Adviser

Department Head

Abstract of Dissertation

Temperature Dependence of Carrier Lifetime, Recombination, and Gain in 1.3 μm InAsP/InGaAsP Multiple Quantum Well Lasers

In this dissertation we investigate the root causes of the strong temperature dependence of the threshold current in 1.3 μm InAsP/InGaAsP Multiple Quantum Well (MQW) Lasers. We accomplish this through measurements of the carrier lifetime, recombination coefficients, and material gain as a function of temperature. We then analyze the temperature dependence of the threshold current by building a mathematical model of the threshold current using the measured parameters and their temperature dependence.

In order to accomplish this goal we developed a new method for measuring the carrier lifetime, which has several advantages over the previously available techniques, and a new analysis for determining the recombination coefficients from the measured carrier lifetime, which is valid for QW lasers. This novel analysis corrects the measured differential carrier lifetime to account for carrier population in both the barrier and separate confinement heterostructure (SCH) regions of quantum well (QW) lasers. The analysis uses information obtained from the measured spontaneous emission spectra to correct the measured lifetime and obtain the intrinsic well lifetime. Once the intrinsic well lifetime is obtained the intrinsic well recombination coefficients can also be obtained. We show that the carrier population in the barrier/SCH layers can significantly affect the measured carrier lifetime and the extracted recombination coefficients. In particular, we show that the Auger recombination coefficient increases with the new QW

analysis and has a positive temperature dependence. We also show that this analysis yields material gain parameters that are very different from those obtained with the traditional analysis and much closer to what is predicted for highly strained QW lasers. These differences indicate the importance of accounting for barrier/SCH carriers on the measurement of basic QW laser material properties.

The model calculation of the threshold current is found to be in excellent agreement with the experimentally measured threshold current from our deep well InAsP/InGaAsP lasers. This model is then used to show that the dominant cause of the temperature dependence of these lasers is Auger recombination, but that the material gain also plays an important role.

Jon M. Pikal
Electrical Engineering Department
Colorado State University
Fort Collins, CO 80523
Fall 1999

Acknowledgments

I would like to first thank my advisor Dr. Carmen Menoni, whose guidance, advice, and patience were instrumental in completing this work. Dr. Menoni not only provided excellent technical guidance but also considerable personal support throughout this difficult process. I would also like to thank Dr. Henryk Temkin for getting me started in semiconductor lasers and for starting me on the road to successful completion of this project. Thanks also to Dr. Carl Wilmsen and Dr. Jim Sites for their time and effort in serving on my graduate committee.

I would also like to thank Dr. Gary Robinson and Dr. Prabhuram Thiagarajan for growing the material that was used throughout this work. In addition, there are also several people in both Dr. Temkin's and Dr. Menoni's labs who were very helpful. Dr. Dmitri Koksenkov, Dr. Mari Ochiai, Dr. Dinesh Patel, and Georgiy Vaschenko all spent many hours listening, discussing, and making suggestions on overcoming the problems, experimental and theoretical, that were encountered during this work.

I would like to thank my parents for instilling in me the desire to obtain this degree as well as providing the confidence required to try. Finally, I would like to thank my wife Eva, who not only proof read all of my work, but also provided the daily moral support and encouragement needed for the completion of this work.

Table of Contents

List of Figures

List of Tables

Chapter I

Introduction

Long haul communication systems generally operate at either the zero dispersion wavelength of silica fibers, 1.3 μm, or the minimum loss wavelength of 1.55 μm. One of the largest obstacles for reducing the cost of the long wavelength communication systems is the current need for active cooling of the semiconductor lasers. This need arises due to the large increase in laser threshold current that is observed with an increase in device operating temperature. Therefore a great deal of effort has been expended in trying to understand the origin of the strong temperature dependence of these lasers in hopes of reducing it. The temperature sensitivity of long wavelength lasers has most recently been associated with an increased contribution of Auger recombination [1]-[4] and to changes in the differential gain, dg/dn, [5]-[8]. In addition, the groups that find dg/dn as the dominant cause also find that the Auger recombination current is very low. On the other hand, the groups that find Auger as the dominant cause of the temperature sensitivity find that as much as 80% of the current flowing through the device is due to Auger recombination. While the data supporting each mechanism as the dominant contribution to the temperature sensitivity is strong, clearly both scenarios cannot be correct. In order to study the temperature dependence of the threshold current one must identify the recombination mechanisms that comprise the current as well as the gain and loss properties that determine the carrier density at which one achieves lasing. While gain can be measured without direct knowledge of the carrier density, determining the material gain parameters, dg/dn and n_0, the transparency carrier density, requires a method of determining carrier density in the active region. The most direct method of examining carrier recombination processes and determining carrier density is through measurement of the carrier lifetime [9].

It is therefore necessary to be able to measure carrier lifetime inside QW active regions to fully understand the origin of the temperature sensitivity of long wavelength lasers. However, several difficulties have arisen when trying to measure the carrier lifetime in QW lasers. The changing laser impedance with bias and frequency complicates extracting the carrier lifetime from measurements [10],[11]. In addition, high frequency poles and zeros created by carrier transport across the separate confinement heterostructure region, and capture and escape into and out of the QW [12], [13] can also effect the determination of the carrier lifetime. Even if these effects can be removed from the carrier lifetime measurement there has been no way of accounting for the distribution of carriers in the barrier and separate confinement heterostructure region. These carriers have a much longer lifetime due to the reduced carrier density in these regions and therefore affect the measured carrier lifetime and extracted recombination parameters [14]-[16].

In this dissertation we develop methods for measuring and analyzing the carrier lifetime in QW lasers. The measurement technique we develop has many advantages over the currently available techniques [17]. It requires only two fitting parameters, enables extraction of the carrier lifetime from data taken at lower frequencies, and does not require additional measurements to account for laser impedance changes. The analysis we develop is based on a two carrier level system of rate equations for the well and barrier/SCH population instead of the traditional single level analysis. This analysis shows that the measured lifetime is actually an effective lifetime that is a function of the well carrier lifetime, the barrier/SCH carrier lifetime, and the distribution of carriers between the two regions [18]. We then use the measured spontaneous emission spectra to estimate the ratio of well carriers to barrier/SCH carriers thus enabling us to obtain the intrinsic well lifetime from the measured effective lifetime. Once the well carrier lifetime is obtained we also obtain the intrinsic recombination parameters of the well material. We will see that the recombination coefficients and the temperature dependence of the coefficients obtained from the QW analysis are very different from the values obtained from the bulk analysis.

We also measure the material gain and use our QW rate equation analysis to determine the intrinsic material gain parameters. Once we have obtained these basic material parameters and their temperature dependence, we build a model that enables us to calculate the threshold current and its temperature dependence. By eliminating, one at a time, the processes that we believe to be contributing to the temperature dependence of the laser we can evaluate the effect of that process. Thus we can identify the laser property or properties that determine the temperature dependence and hopefully use this information to design and build better lasers.

References for Chapter I

[1] W. Fang, M. Hattendorf, S. L. Chuang, J. Minch, C. S. Chang, C. G. Bethea, and Y. K. Chen, "Analysis of Temperature Sensitivity in Semiconductor Lasers Using Gain and Spontaneous Emission Measurements," Appl. Phys. Lett., Vol. 70, No. 7, pp. 796-798, 1997

[2] S. J. Sweeney, A. F. Phillips, A. R. Adams, E. P. O'Reilly, and P. J. A. Thijs, "The Effect of Temperature Dependent Processes on the Performance of 1.5 μm Compressively Strained InGaAs(P) MQW Semiconductor Diode Lasers," IEEE Photon. Technol. Lett., Vol. 10, No. 8, pp. 1076-1078, 1998

[3] J. Braithwaite, M. Silver, V. A. Wilkinson, E. P. O'Reilly, and A. R. Adams, "Role of Radiative and Nonradiative Processes on the Temperature Sensitivity of Strained and Unstrained 1.5 μm InGaAs(P) Quantum Well Lasers," Appl. Phys. Lett., Vol. 67, No. 24, pp. 3546-3548, 1995

[4] T. Higashi, S. J. Sweeney, A. F. Phillips, A. R. Adams, E. P. O'Reilly, T. Uchida, and T. Fujii, "Observation of Reduced Nonradiative Current in 1.3-m AlGaInAs-InP Strained MQW Lasers," IEEE Photon. Technol. Lett., Vol. 11, No. 4, pp. 409-411, 1999

[5] Y. Zou, J. S. Osinski, P. Grodzinski, P. D. Dapkus, W. C. Rideout, W. F. Sharfin, J. Schlafer, and F. D. Crawford, "Experimental Study of Auger Recombination, Gain, and Temperature Sensitivity of 1.5μm Compressively Strained Semiconductor Lasers," IEEE J. Quantum Electron., Vol. **29**, No. 6, pp. 1565-1575, 1993

[6] D. A. Ackerman, P. A. Morton, G. E. Shtengel, M. S. Hybertsen, R. F. Kazarinov, T. Tanbun-Ek, and R. A. Logan, "Analysis of T_0 in 1.3 μm Multi-Quantum-Well and Bulk Active Lasers," Appl. Phys. Lett., Vol. 66, No. 20, pp. 2613-2615, 1995

[7] D. A. Ackerman, G. E. Shtengel, M. S. Hybertsen, P. A. Morton, R. F. Kazarinov, T. Tanbun-Ek, and R. A. Logan, "Analysis of Gain in Determining T_0 in 1.3 μm Semiconductor Lasers," IEEE J. Selected Topics Quantum Electron., Vol., 1, No. 2, pp. 250-263, 1995

[8] A. A. Bernussi, J. Pikal, H. Temkin, D. L. Coblentz, and R. A. Logan, "Rate Equation Model of High-Temperature Performance of InGaAsP Quantum Well Lasers," Appl. Phys. Lett., Vol. 66, No. 26, pp. 3606-3608, 1995

[9] R. Olshansky, C. B. Su, J. Manning, and W. Powazinik, "Measurement of Raditive and Nonradiative Recombination Rates in InGaAsP and AlGaAs Light Sources," IEEE J. Quantum Electron., Vol., QE-20, No. 8, pp. 838-854, 1984

[10] G. E. Shtengel, D.A. Ackerman and P.A. Morton, "True Carrier Lifetime Measurements of Semiconductor Lasers," Electron. Lett., Vol. 31, No. 20, pp. 1747-1748, 1995

[11] G. E. Shtengel, D.A. Ackerman, P.A. Morton, E. J. Flynn, and M. S. Hybertsen, "Impedance-Corrected Carrier Lifetime Measurements in Semiconductor Lasers," Appl. Phys. Lett., Vol. 67, No. 11, pp. 1506-1508, 1995

[12] S. Weisser, I. Esquivias, P. J. Tasker, J. D. Ralston, B. Romero, and J. Rosenzweig, "Impedance Characteristics of Quantum-Well Lasers," IEEE Photon. Technol. Lett., Vol. 6, No. 12, pp. 1421-1423, 1994

[13] I. Esquivias, S. Weisser, B. Romero, J. D. Ralston, and J. Rosenzweig, "Carrier Capture and Escape Times in $In_{0.35}Ga_{0.65}As$-GaAs Multiquantum-Well Lasers Determined from High-Frequency Electrical Impedance Measurements," IEEE Photon. Technol. Lett., Vol. 8, No. 10, pp. 1294-1296, 1996

[14] A. P. Ongstad, D. J. Gallant, and G. C. Dente, "Carrier Lifetime Saturation in InGaAs Single Quantum Wells," Appl. Phys. Lett., Vol. 66, No. 20, pp. 2730-2732, 1995

[15] Y. C. Chen, P. Wang, J. J. Coleman, D. Bour, K. K. Lee, and R. G. Waters, "Carrier Recombination Rates in Strained-Layer InGaAs-GaAs Quantum Wells," IEEE J. Quantum Electron., Vol. 27, No. 6, pp. 1451-1454, 1991

[16] T. Yamamoto, T. Odagawa, K. Tanaka, and S. Ogita, "Influence of Separate Confinement Heterostructures on the Effective Carrier Recombination Coefficient in Quantum Well Laser Structures," Appl. Phys. Lett., Vol. 71, No. 11, pp. 1543-1545, 1997

[17] J. M. Pikal, C. S. Menoni, H. Temkin, P. Thiagarajan, and G. Y. Robinson, "Impedance Independent Optical Carrier Lifetime Measurements in Semiconductor Lasers," Rev. of Sci. Instrum., Vol. 69, No. 12, Dec. 1998

[18] J. M. Pikal, C. S. Menoni, H. Temkin, P. Thiagarajan, and G. Y. Robinson, "Carrier Lifetime and Recombination in Long Wavelength Quantum Well Lasers," IEEE J. Selected Topics Quantum Electron., 1999

Chapter II

Background

There are three sections to this chapter, the first provides a very simple introduction to the properties of semiconductor lasers that are important for understanding this dissertation. The second section outlines the problem that this dissertation addresses, namely the temperature dependence of the threshold current, and gives some background on other work done in this area. The final section describes the laser structures used in this thesis and how they were grown.

2.1) Semiconductor Laser Fundamentals

Semiconductor lasers are a very important building block for many opto-electronic systems. They provide direct electrical to optical energy conversion, and do so efficiently. The semiconductor laser is just like any other laser in that it requires a region of optical gain and mirrors to provide optical feedback. The advantage of the semiconductor laser is that the semiconductor itself can be used for both purposes. A PN junction provides a means of direct electrical control over the material gain and the cleaved edges of a piece of this semiconductor provide the mirrors. In addition the large density of electronic states in a semiconductor allows for reasonable optical gain (few thousand/cm) from a small length of material. A diagram of a simple PN junction laser is shown in figure 2.1. Typical laser lengths are 200 μm to 500 μm and the width of the active region can be as small as about 1 μm for a buried heterostructure laser to 100 μm for the metal stripe laser shown in the figure. Thus a small piece of semiconductor material a few hundred microns long with cleaved edges is all that is needed for a complete laser.

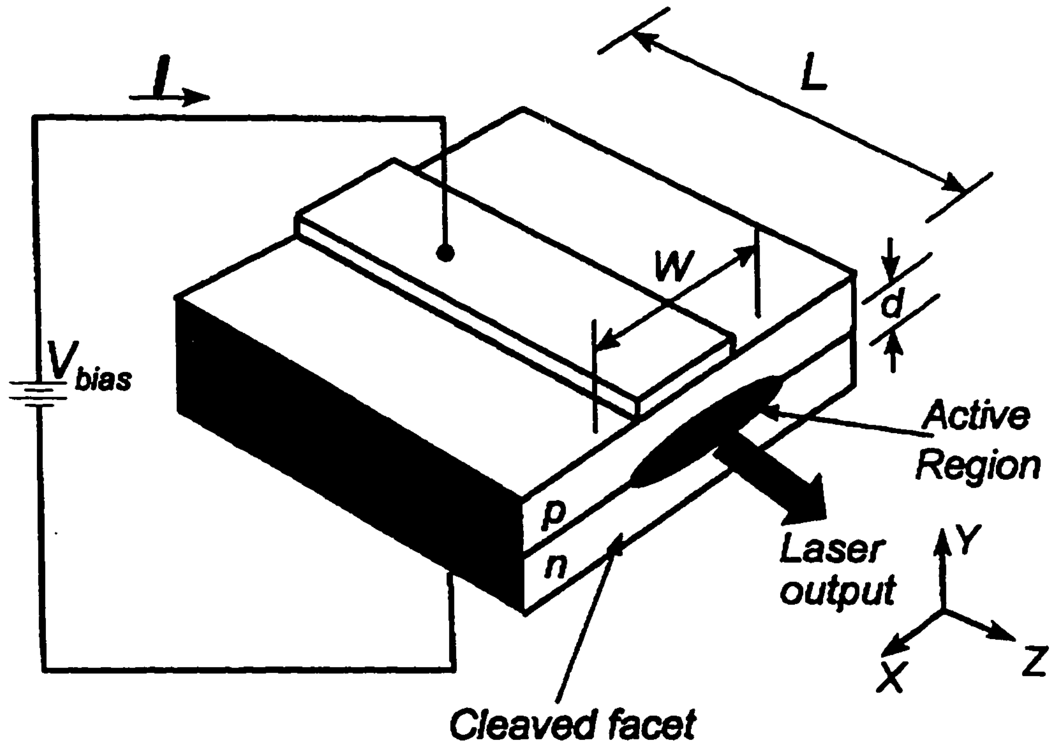

Fig. 2.1 – Schematic of a simple semiconductor PN junction stripe laser [1]

To understand what is needed to achieve lasing we must first look at the optical losses that occur in a semiconductor laser. These losses are normally broken up into two terms, the mirror losses α_m and the internal losses α_i. The mirror losses are due to less than 100% reflection at the cleaved mirrors and we normally write them as a distributed loss using eqn. (2.1) [2].

$$\alpha_m = \frac{1}{L}\ln\left(\frac{1}{R}\right) \tag{2.1}$$

where $$R = \left(\frac{\eta_{eff} - 1}{\eta_{eff} + 1}\right)^2$$

In these equations L is the cavity length, R is the mirror reflectivity (~0.28 for our uncoated lasers), and η_{eff} is the effective index of refraction for the cavity mode. Equation (2.1) assumes equal reflectivity for both mirrors and yields a mirror loss of ~26 cm^{-1} for a 500 μm long laser. From this equation we see that the mirror losses can be made smaller by simply using a longer laser. However, longer lasers have a larger gain region to pump, in addition, eventually the internal losses will dominate the total losses and further increase in laser length will yield no real improvement in total losses. The internal loss includes all other losses such as light scattering at interfaces or defects, free-carrier absorption, and inter-valence band absorption. It is usually between 5 and 40 cm^{-1} (~27 cm^{-1} as we will see later for our deep well InAsP/InGaAsP lasers) and depends on the laser material, structure, and operating conditions.

The material gain g is obtained directly by applying a forward bias to a PN junction diode. The applied bias creates, near the junction, an excess electron and hole population in the conduction and valence band, respectively. These changes are measured through the quasi-Fermi levels, which allow calculation of the carrier population in the bands. When the applied bias is large enough such that the Fermi level separation is equal to the band-gap energy, the joint probability that a pair of states separated by that energy will be occupied is ½. A photon with this energy, traversing the cavity, will have an equal probability of being absorbed or stimulating a recombination event and generating an additional photon. This condition is called material transparency and the carrier density at which this occurs is the transparency carrier density n_{tr}.

However, in order for a device to reach lasing the material gain must be large enough to overcome the total losses. Thus the threshold gain can be expressed as [3]:

$$\Gamma g_{th} = \alpha_m + \alpha_i \tag{2.2}$$

where g_{th} is the material gain at threshold and Γ, the optical confinement factor, is the overlap between the optical mode and the gain region. While the threshold gain can be found from (2.2) we generally express the material gain as a linear function of carrier density n above transparency as [3]:

$$g = a(n - n_{tr}) \tag{2.3}$$

where a is the differential gain dg/dn. We will see in chapter 5 that the gain in strained QW lasers generally follows more of a natural log dependence on carrier density but for now we will use the simpler form of (2.3). By combining equation (2.3) with equation (2.2) at threshold, where n becomes the threshold carrier density n_{th}, we can solve for n_{th}.

$$n_{th} = \frac{\alpha_m + \alpha_i}{\Gamma a} + n_{tr} \tag{2.4}$$

Since stimulated emission is such an efficient process any attempt to increase the carrier density above n_{th} results in additional light output and the carrier density is pinned at n_{th}.

The carrier and photon processes in semiconductor lasers are generally described by a set of rate equations for the carrier concentration n and photon density s [2]-[5].

$$\frac{dn}{dt} = \frac{\eta_{inj} I}{qV} - \frac{n}{\tau} - v_g a(n - n_{tr})s \tag{2.5}$$

$$\frac{ds}{dt} = v_g a(n - n_{tr})s + \beta\frac{n}{\tau} - \frac{s}{\tau_p} \tag{2.6}$$

In this equation η_{inj} is the injection efficiency, I is the injected current, q is the electronic charge, V is the volume of the active region, τ is the spontaneous recombination lifetime, v_g is the group velocity, β is the fraction of spontaneous emission which couples into the cavity mode, and τ_p is the photon lifetime. The first term on the right hand side of (2.5) represents the increase in carrier density due to injected current while the second is carrier loss to spontaneous recombination and the third term is the loss to stimulated emission. The photon density increases due to stimulated emission, first term in (2.6), and spontaneous emission, the second term. The third term represents photon loss and is related to the total loss $\alpha_m + \alpha_i$ described earlier.

A steady state or DC analysis of equations (2.5) and (2.6) leads to a relationship between the photon density and the bias current.

$$s = \frac{\eta_{inj}\tau_p}{qV}\left(I - \frac{n}{\tau}\frac{qV}{\eta_{inj}}\right) + \beta\tau_p\frac{n}{\tau} \tag{2.7}$$

Because n is pinned above threshold at the threshold carrier density, n_{th}, the spontaneous lifetime τ is also pinned at τ_{th}. By defining the second term in the brackets as the threshold current [4]:

$$I_{th} = \frac{n_{th}}{\tau_{th}}\frac{qV}{\eta_{inj}} \tag{2.8}$$

we can rewrite (2.7) as.

$$s = \frac{\eta_{inj}\tau_p}{qV}(I - I_{th}) + \beta\tau_p\frac{n_{th}}{\tau_{th}} \tag{2.9}$$

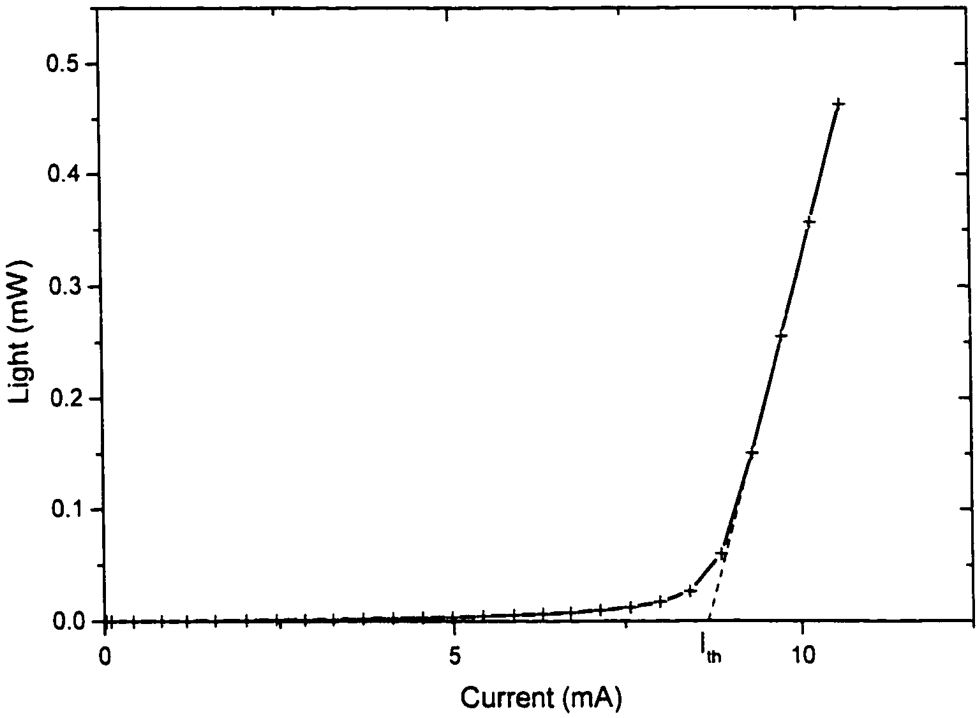

Fig. 2.2 - Light-Current curve for 500μm long deep well InAsP laser

This equation is only valid above threshold since we have assumed that the carrier density is pinned at n_{th}. The last term in equation (2.9) is the spontaneous emission term, which is also pinned above threshold since the carrier density is pinned. The first term is the stimulated emission term, which quickly overcomes the spontaneous emission above threshold. Once this has occurred we see that the light increases linearly with increasing current. Figure 2.2 is a typical light versus current curve obtained from an InAsP/InGaAsP laser at 20°C. The figure shows the linear region above threshold as well as the transition region from spontaneous emission to stimulated emission. From the definition of the threshold current (2.8) we can see that either an increase in n_{th} or a decrease in τ_{th} or η_{inj} can lead to an increase in the threshold current. η_{inj} is a measure of the amount of current leaking around or over the active region. As such it is a fundamental parameter based on material and structural properties of the laser and we will discuss it in more detail later. The threshold carrier density was written as a function of material and structural parameters in equation (2.4) and we now turn our attention to a description of the carrier lifetime so that we may understand its role in the threshold current on a more fundamental level.

The injected excess carrier population can recombine in several different ways and the most common approach is to use a simple polynomial expression for the recombination rate [6].

$$R(n) = An + Bn^2 + Cn^3 = \frac{n}{\tau} \tag{2.10}$$

Generally the A coefficient is associated with Shockley-Hall-Read or defect recombination due to the expected linear dependence of this type of recombination on excess carrier density. Radiative recombination requires both an electron and a hole and is therefore dependent on the carrier density squared and assigned to the B coefficient. Auger recombination requires three carriers, an electron in the conduction band recombines with a hole in the valence band and the excess energy is given off to either another conduction band electron or a valence band hole kicking higher up in the band. This type of recombination therefore depends on the carrier density cubed and is associated with the C coefficient in eqn. (2.10). Thus the carrier lifetime contains information about the recombination processes going on in the laser and allows us to evaluate which recombination processes dominate. Later in this dissertation we will also utilize the differential carrier lifetime which is defined in equation (2.11) [6].

$$\frac{1}{\tau'} = \frac{dR(n)}{dn} = A + 2Bn + 3Cn^2 \tag{2.11}$$

This lifetime is a very useful parameter because it is the carrier lifetime that is obtained using the small signal measurement techniques described in chapter 3. By comparing (2.10) and (2.11) we see that the differential lifetime is the same as the total lifetime if B and C are zero, but can be a factor of 2 or 3 lower if the radiative or Auger recombination dominates, respectively.

Using (2.10) in (2.8) yields a more fundamental expression for the threshold current in terms of the recombination coefficients and n_{th}, who's relationship to fundamental material parameters we repeat here for convenience.

$$I_{th} = \frac{qV}{\eta_{inj}}\left(An_{th} + Bn_{th}^{2} + Cn_{th}^{3}\right) \qquad \text{where} \qquad n_{th} = \frac{\alpha_m + \alpha_i}{\Gamma a} + n_{tr} \tag{2.12}$$

We see from the above analysis that the cavity losses determine the gain necessary to reach threshold and the material gain determines at what carrier density this gain is achieved. The current is determined from the recombination processes at that carrier density and the amount of current that leaks around the active region, η_{inj}. This is a complete description of the process involved in determining the threshold current of a semiconductor laser and clearly if any of these parameters are temperature dependent then the threshold current will also be temperature dependent.

2.2) Temperature Dependence of Threshold Current

As discussed in Chapter 1, the temperature dependence of the threshold current is one of the biggest problems in long wavelength semiconductor lasers. In the previous section we described what is required for a laser to reach threshold concluding with equation (2.12) which contained all of the relevant material and device parameters contributing to the threshold current. Despite the complexity of this equation, the threshold current is typically found to follow the exponential dependence on temperature shown in equation (2.13) [2],[3].

$$I_{th} = I_0 \exp\left(\frac{T}{T_0}\right) \tag{2.13}$$

T_0 is the characteristic temperature, with a low value indicating a strong temperature dependence. A great deal of work has been done investigating the origin of the low T_0 found in long wavelength communication lasers and nearly every parameter in equation (2.12) has at one time or another been cited as the main cause.

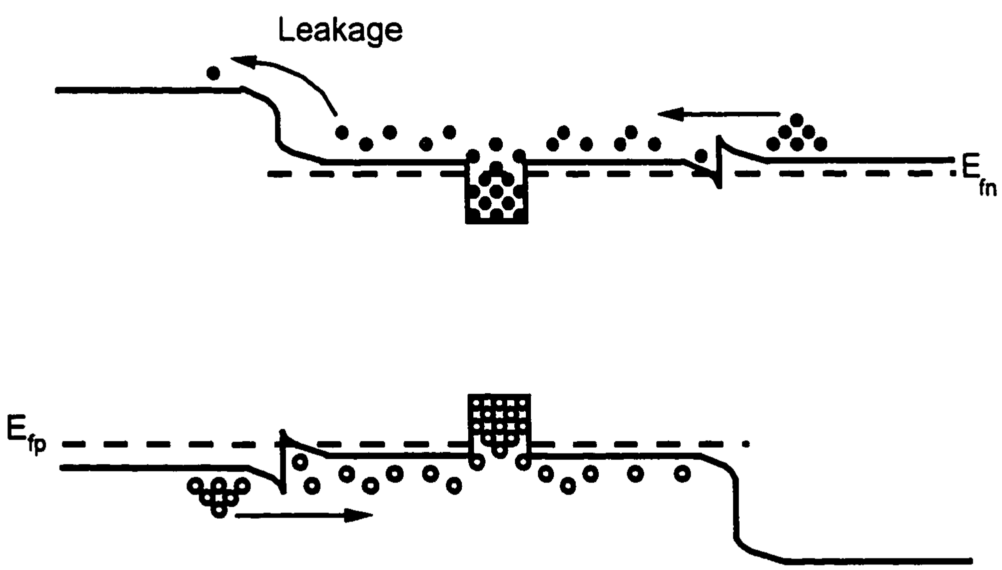

Fig. 2.3 - Schematic showing carrier leakeage over the heterobarrier

Temperature dependent optical loss [7]-[9], heterobarrier leakage [10]-[12], and Auger [13]-[17] were originally thought to be the main culprit of the low T_0 in long wavelength lasers. Heterobarrier leakage, illustrated in figure 2.3, is the drift of high energy particles, usually electrons, over the heterobarrier defining the active region. Once these carriers reach the other side of the junction they are minority carriers and recombine either in the cladding region or at the contact, thus they contribute to the device current but not to active region carrier population. This process is temperature dependent since only carrier with sufficient kinetic energy can clear the heterobarrier on the other side of the active region.

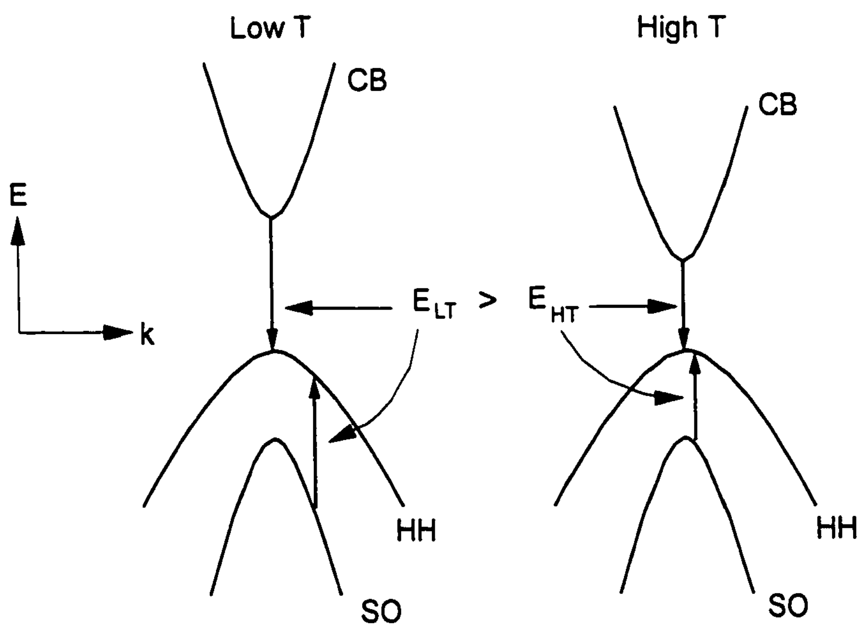

Fig 2.4 - Temperature dependence of Intervalence band absorption

The temperature dependence of the optical losses comes mainly from Intervalence Band Absorption (IVBA) which is shown in figure 2.4. In this process a photon is absorbed giving its energy to an electron in the split off band and raising it to the heavy hole band. The strong temperature dependence of this process arises from the reduction of the band gap energy with increasing temperature. This results in emitted photons of lower energy, $E_{LT} > E_{HT}$ in the figure, thus lowering the wavevector, k, at which this absorption process can occur. Since there are more heavy holes at low k this process becomes more efficient at higher temperatures.

Equation (2.12) tells us that there are two ways that Auger recombination can increase the threshold current. First, since the Auger rate is proportional to the carrier density cubed, anything that increases the threshold carrier density also increases Auger, including all of the gain and loss parameters in (2.4). Second, the Auger coefficient C also increases with temperature for reasons similar to the IVBA increase. As discussed earlier, Auger recombination involves three particles, an electron that recombines with a hole and gives off the energy to either another electron or a hole. The shrinking band gap with temperature means less energy for the third particle making it easier to conserve energy and momentum in the transition and thus increasing the Auger coefficient.

Theoretically the introduction of highly strained QW lasers was predicted to reduce both the optical loss and the Auger recombination [18]-[20] due to changes in the valence band structure. However while reduction in these loss mechanisms has been confirmed experimentally [21]-[23] no significant improvement in T_0 has been achieved. Recently the focus has concentrated on the temperature dependence of the gain [22]-[25] along with numerous studies maintaining that Auger recombination is to blame [26]-[29]. The fact that the material gain (2.3) decreases with temperature is expected. If we calculate the material gain from the transition probability assuming that the k selection rules hold we obtain [3]:

$$g(E,T) \propto DOS \times [f_c(E,T) + f_v(E,T) - 1] \tag{2.14}$$

DOS is the joint density of electronic states between the conduction and valence bands, which is independent of temperature. f_c and f_v are the Fermi distribution functions for the electrons and holes, respectively, which broaden in energy as the temperature increases. This broadening also lowers the peak values of these functions, lowering the peak gain at a given carrier density, and thus resulting in increased transparency carrier density and decreased differential gain parameters of equation (2.3). However, because this effect is related to the broadening of the Fermi distribution functions and not a material parameter, it should be the same for long wavelength lasers as it is for shorter wavelength lasers. Experimentally this is not the case as shorter wavelength lasers have much higher T_0 values.

Looking at the most recent studies on T_0 we see a pattern develop. All of the studies that find the gain responsible for the temperature sensitivity are on QW lasers and use carrier lifetime measurements to determine the recombination mechanisms that make up the current and the active region carrier density [22]-[25]. While this is a very direct method of examining the makeup of the device current, all of these studies neglect the effect of barrier/SCH carrier population on the carrier lifetime and thus incorrectly measure the recombination coefficients and the carrier density. This leads directly to an underestimation of the Auger recombination and an overestimation of the active region carrier density and thus the incorrect analysis of the temperature dependence.

The recent studies that determine Auger to be dominant use spontaneous emission measurements, sometimes coupled with gain measurements, to determine the nonradiative current contribution to T_0 [26]-[29]. This is accomplished by estimating the fraction of spontaneous emission collected in order to determine the total radiative current. The amount of nonradiative current is then determined by subtracting the radiative current from the total measured current. Accurately measuring the fraction of spontaneous emission collected is obviously very important in these studies and is accomplished in one of two ways. If it is assumed that collection efficiency is constant and that all of the current is radiative at low temperatures [27]-[29] the collection efficiency can be determined from the low temperature spontaneous emission data. The collection efficiency can also be obtained by fitting the relationship relating the gain and spontaneous emission spectra [26], however this fit also requires two other fitting parameters, the total losses and the quasi-Fermi level separation. These measurements are less direct since they do not measure the Auger recombination current but infer its importance from the radiative emission. These measurements show that up to 80% of the threshold current is due to Auger recombination and despite their problems are probably more accurate than the previous lifetime studies on QW lasers. Unfortunately spontaneous emission measurements, even coupled with gain measurements, do not provide an accurate means for determining active region carrier density making it very difficult to estimate the effect the material gain parameters have on T_0. We show in this work how to correct the carrier lifetime measurements for the barrier/SCH carrier population and therefore extract intrinsic recombination and gain parameters in QW lasers.

2.3) Laser Materials and Structures for Long Wavelength Communication Lasers

The most common material system for 1.3 μm lasers is the InGaAsP system. In this material system there is a great deal of flexibility since the active material can be either lattice matched to InP or strained. In addition the QW barrier and SCH region can be made lattice matched with a variety of different band gap wavelengths. The QW barriers can even be made with strain opposite to the active material strain in order to produce a strain compensated system. However, recently there has been considerable interest in highly strained InAsP as the alternative active material for such lasers. Not only is this a ternary alloy which should allow for better growth, but InAsP/InGaAsP also has a higher conduction band offset, $0.7\Delta E_g$ [30],[31] versus approximately $0.4\Delta E_g$ [32] for the quaternary alloy. This improves the electron confinement in the wells, particularly at high temperatures, and should improve the performance of these lasers. Several groups, including our own, have reported excellent threshold currents and efficiencies even at elevated temperatures for these InAsP based lasers [31],[33],[34].

In the work described in this dissertation we perform measurements on two different InAsP separate confinement heterostructure multiple quantum well (SCH-MQW) lasers. The general laser structure consists of a 1.0 μm n-type InP cladding layer (1×10^{18} cm^{-3}), the active region, a p-type InP cladding layer (7×10^{17} cm^{-3}), and finally a 0.2 μm p-type InGaAs contact layer (2×10^{19} cm^{-3}). The active region consists of six wells of $InAs_{0.45}P_{0.55}$, 4.5 nm thick, with lattice matched InGaAsP barriers, and 110 nm thick InGaAsP separate confinement layers on both sides of the MQW region. The differences between the two samples are illustrated in figure 2.5 (a) and (b) with the biggest difference being the band-gap wavelength of the barrier/SCH regions.

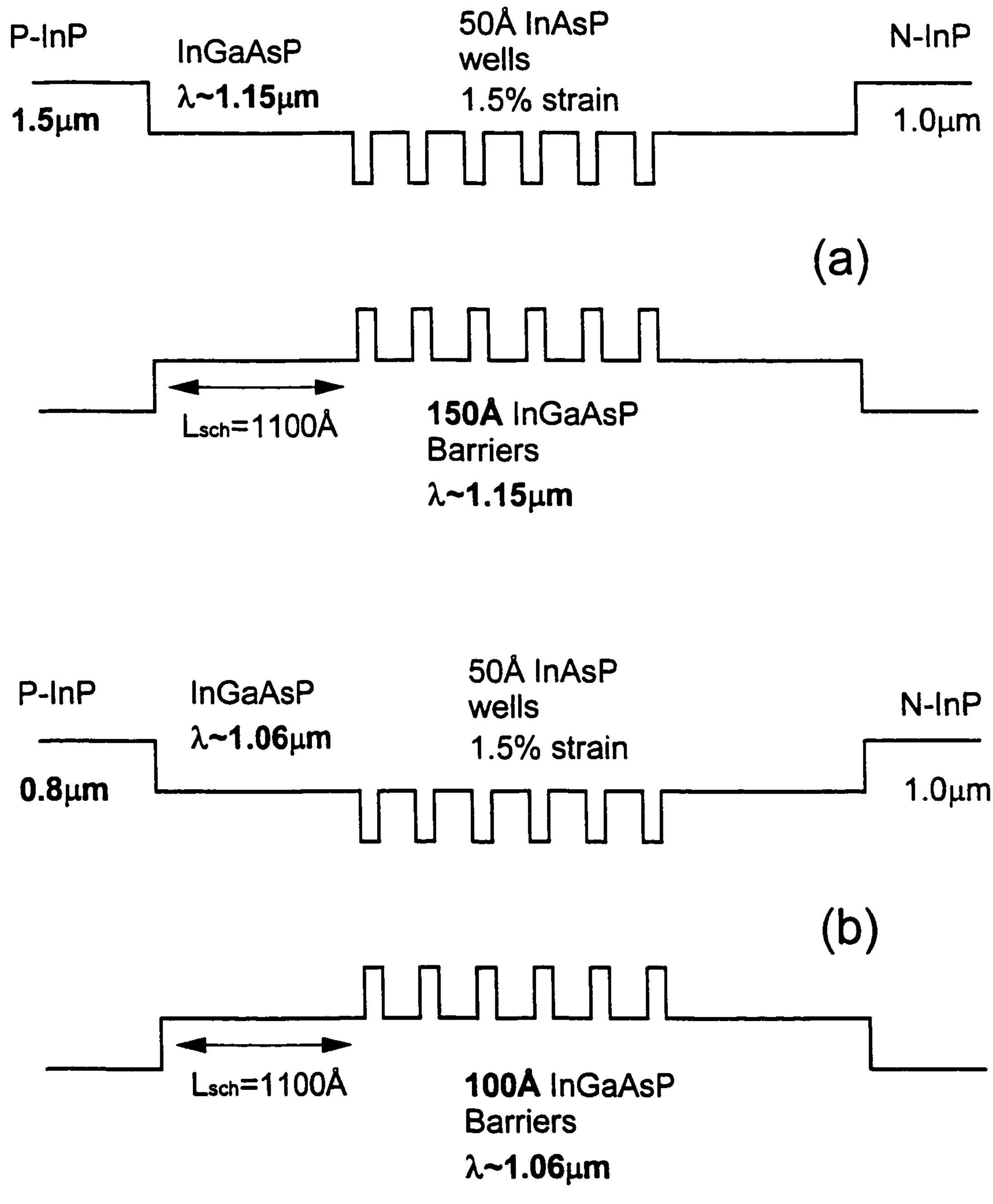

Fig 2.5 - Shallow (a) and deep well (b) InAsP/InP MQW SCH lasers used in this study

Throughout this dissertation we will refer to the two structures as the shallow well, λ_b = 1.15 μm, and deep well, λ_b = 1.06 μm, lasers, referring to the difference in quantum confinement this provides. The deep well lasers also have narrower barriers, which

Parameter	Shallow Well	Deep Well
Length	500 μm	500 μm
Width	1.7 μm	1.4 μm
I_{th}	~8 mA	~10 mA
Γ	0.0636 [1]	0.05486
η_i	0.7 [1]	.906
α_i	10.5 cm^{-1} [1]	27.5 cm^{-1}
A	4.5 x 10^7 s^{-1}	3.5 x 10^7 s^{-1}
B_w	7.2 x 10^{-11} cm^3/s	6.8 x 10^{-11} cm^3/s
C_w	5.1 x 10^{-29} cm^6/s	3.4 x 10^{-29} cm^6/s
n_{tr}	1.8 x 10^{18} cm^{-3}	2.35 x 10^{18} cm^{-3}
dg/dn (at n_{tr})	.967 x 10^{-15} cm^2	1.09 x 10^{-15} cm^2

Table 2.1 – Comparison of material and structural properties of the shallow well and deep well InAsP buried heterostructure (BH) lasers used in this study.

results in a larger effective strain [1], and a shorter P cladding layer that may increase the leakage current [3]. All lasers were grown at CSU by gas-source molecular beam epitaxy (GSMBE) as described in [1],[33],[35] and buried with an InP current blocking structure grown by MOCVD as described in [36]. Typical threshold currents for the 500 μm long devices investigated were around 8 mA and 10 mA for the shallow and deep well lasers, respectively. Table 1 summarizes the material and structural parameters for the shallow and deep well buried heterostructure (BH) lasers at 20°C that are obtained from this, and in a few cases, previous work [1] with these lasers.

References for Chapter II

[1] P. Thiagarajan, "InAsP/InGaAsP Multiple Quantum Well Lasers," Doctoral Dissertation, Colorado State University, 1996

[2] L. A. Coldren and S. W. Corzine, "*Diode Lasers and Photonic Integrated Circuits*," John Wiley and Sons, New York, NY, 1995

[3] G. P. Agrawal and N. K. Dutta, "*Semiconductor Lasers*," 2nd ed., Van Nostrand Reinhold, New York, NY, 1993

[4] J. T. Verdeyen, "*Laser Electronics*," 2nd ed., Prentice-Hall, Englewood Cliffs, NJ, 1989

[5] P. S. Zory, Jr., "*Quantum Well Lasers*," Academic Press, San Diego, CA, 1993

[6] R. Olshansky, C. B. Su, J. Manning, and W. Powazinik, "Measurement of Raditive and Nonradiative Recombination Rates in InGaAsP and AlGaAs Light Sources," IEEE J. Quantum Electron., Vol., QE-20, No. 8, pp. 838-854, 1984

[7] M. Asada, A. R. Adams, K. E. Stubkjaer, Y. Suematsu, Y. Itaya, and S. Arai, "Temperature Dependence of the Threshold Current of GaInAsP/InP DH Lasers," IEEE J. Quantum Electron., Vol., QE-17, No. 8, pp. 611-618, 1981

[8] M. Asada, A. Kameyama, and Y. Suematsu, "Gain and Intervalence Band Absorption in Quantum-Well Lasers," IEEE J. Quantum Electron., Vol., QE-20, pp. 745-753, 1984

[9] A. R. Adams, M. Asada, Y. Suematsu, and A. Arai, "The Temperature Dependence of the efficiency and Threshold Current of $In_{1-x}Ga_xAs_yP_{1-y}$ Lasers Related to Intervalence Band Absorption," Jap. J. Appl. Phys., Vol. 19, pp. L621-L624, 1980

[10] H. C. Casey, Jr., "Temperature Dependence of the Threshold Current Density in InP- $Ga_{.28}In_{.72}As_{.6}P_{.4}$ (λ=1.3μm) Double Heterostructure Lasers," J. Appl. Phys., vol. 56, pp. 1959-1964, 1984

[11] M. Ettenberg, C. J. Nuese, and H. Kressel, "The Temperature Dependence of Threshold Current for Double-Heterojunction Lasers," J. Appl. Phys., vol. 50, pp. 2249-2950, 1979

[12] M. Yano, H. Imai, and M. Takusagawa, "Analysis of Threshold Temperature Characteristics for InGaAsP/InP Double-Heterojunction Lasers," J. Appl. Phys., vol. 52, pp. 3172-3175, 1981

[13] N. K. Dutta and J. Nelson, "The Case for Auger Recombination in $In_{1-x}Ga_xAs_yP_{1-y}$," J. Appl. Phys., vol. 53, pp. 74-92, 1982

[14] N. K. Dutta and J. Nelson, "Temperature Dependence of Threshold of InGaAsP Double Heterostructure Lasers and Auger Recombination," Appl. Phys. Lett., vol. 38, pp. 407-409, 1981

[15] B. Sermage, J. P. Heritage, and N. K. Dutta, "Temperature Dependence of Carrier Lifetime and Auger Recombination in 1.3 μm InGaAsP," J. Appl. Phys., vol. 57, pp. 5443-5449, 1985

[16] P. L. Liu, J. P. Heritage, and O. E. Martinez, "Temperature Dependence of Threshold Current of an InGaAsP Laser Under 130-ps Electrical Pulse Pumping," Appl. Phys. Lett., vol. 44, pp. 370-372, 1984

[17] C. B. Su, R. Olshansky, J. Manning, and W. Powazinik, "Temperature Dependence of Threshold Current in III-V Semiconductor Lasers: Experimental Prediction and Explanation," Appl. Phys. Lett., vol. 44, pp. 1030-1032, 1984

[18] E. Yablonovitch and E. O. Kane, "Reduction of Lasing Threshold Current Density by the Lowering of the Valence Band Effective Mass," J. Lightwave Technol., Vol. 4, pp. 504-506, 1986

[19] A. R. Adams, "Band Structure Engineering for Low-Threshold High Efficiency Semiconductor Lasers," Electron. Lett., Vol. 22, pp. 249-250, 1986

[20] E. P. O'Reilly and A. R. Adams, "Band Structure Engineering in Strained Semiconductor Lasers," IEEE J. Quantum Electron., Vol., QE-30, pp. 366-379, 1994

[21] G. Fuchs, J. Horer, A. Hangleiter, V. Harle, F. Scholz, R. W. Glew, and L. Goldstein, "Intervalence Band Absorption in strained and unstrained InGaAs Multiple Quantum Well Structures," Appl. Phys. Lett., Vol. 60, pp. 231-233, 1992

[22] D. A. Ackerman, G. E. Shtengel, M. S. Hybertsen, P. A. Morton, R. F. Kazarinov, T. Tanbun-Ek, and R. A. Logan, "Analysis of Gain in Determining T_0 in 1.3 μm Semiconductor Lasers," IEEE J. Selected Topics Quantum Electron., Vol., 1, No. 2, pp. 250-263, 1995

[23] Y. Zou, J. S. Osinski, P. Grodzinski, P. D. Dapkus, W. C. Rideout, W. F. Sharfin, J. Schlafer, and F. D. Crawford, "Experimental Study of Auger Recombination, Gain, and Temperature Sensitivity of 1.5μm Compressively Strained Semiconductor Lasers," IEEE J. Quantum Electron., Vol. **29**, No. 6, pp. 1565-1575, 1993

[24] D. A. Ackerman, P. A. Morton, G. E. Shtengel, M. S. Hybertsen, R. F. Kazarinov, T. Tanbun-Ek, and R. A. Logan, "Analysis of T_0 in 1.3 μm Multi-Quantum-Well and Bulk Active Lasers," Appl. Phys. Lett., Vol. 66, No. 20, pp. 2613-2615, 1995

[25] A. A. Bernussi, J. Pikal, H. Temkin, D. L. Coblentz, and R. A. Logan, "Rate Equation Model of High-Temperature Performance of InGaAsP Quantum Well Lasers," Appl. Phys. Lett., Vol. 66, No. 26, pp. 3606-3608, 1995

[26] W. Fang, M. Hattendorf, S. L. Chuang, J. Minch, C. S. Chang, C. G. Bethea, and Y. K. Chen, "Analysis of Temperature Sensitivity in Semiconductor Lasers Using Gain And Spontaneous Emission Measurements," Appl. Phys. Lett., Vol. 70, No. 7, pp. 796-798, 1997

[27] S. J. Sweeney, A. F. Phillips, A. R. Adams, E. P. O'Reilly, and P. J. A. Thijs, "The Effect of Temperature Dependent Processes on the Performance of 1.5 μm Compressively Strained InGaAs(P) MQW Semiconductor Diode Lasers," IEEE Photon. Technol. Lett., Vol. 10, No. 8, pp. 1076-1078, 1998

[28] J. Braithwaite, M. Silver, V. A. Wilkinson, E. P. O'Reilly, and A. R. Adams, "Role of Radiative and Nonradiative Processes on the Temperature Sensitivity of Strained and Unstrained 1.5 μm InGaAs(P) Quantum Well Lasers," Appl. Phys. Lett., Vol. 67, No. 24, pp. 3546-3548, 1995

[29] T. Higashi, S. J. Sweeney, A. F. Phillips, A. R. Adams, E. P. O'Reilly, T. Uchida, and T. Fujii, "Observation of Reduced Nonradiative Current in 1.3-m AlGaInAs-InP Strained MQW Lasers," IEEE Photon. Technol. Lett., Vol. 11, No. 4, pp. 409-411, 1999

[30] R. P. Schneider, JR. And B. W. Wessels, "Photoluminescence Excitation Spectroscopy of $InAs_{0.67}P_{0.33}$/InP Strained Single Quantum Wells," J. Electron. Mater., Vol. 20, No. 12, pp. 1117-1123, 1991.

[31] M. Yamamoto, N. Yamamoto, and J. Nakano, "MOVPE Growth of Strained InAsP/InGaAsP Quantum-Well Structures for Low-Threshold 1.3-μm Lasers," IEEE J. Quantum Electon., Vol. 30, No. 2, pp. 554-560, 1994.

[32] E. A. Montie, P. J. A. Thijs, and G. W. 't Hooft, "Photoluminescence excitation spectroscopy of $Ga_xIn_{1-x}As_yP_{1-y}$/InP quantum wells," Appl. Phys. Lett., Vol. 53, No. 17, pp. 1611-1613, 1988.

[33] P. Thiagarajan, G. E. Giudice, H. Temkin, G. Y. Robinson, "Low Threshold Current 1.3 μm InAsP/InGaAsP Lasers grown by Gas-Source Molecular Beam Epitaxy," Electron. Lett., Vol. 32, No. 12, pp. 1103-1105, 1996

[34] H. Oohashi, S. Seki, T. Hirono, H. Sugiura, T. Amano, M. Ueki, J. Nakano, M. Yamamoto, Y. Tohmori, M. Fukuda, and K. Yokoyama, "High-power and high-efficiency 1.3μm InAsP compressively-strained MQW lasers at high temperatures," Electron. Lett., Vol. 31, No. 7, pp. 556-557, 1995.

[35] P. Thiagarajan, A. A. Bernussi, H. Temkin, G. Y. Robinson, A. M. Sergent, and R. Logan, "Growth of 1.3 μm InAsP/InGaAsP Laser Structures by Gas Source Molecular Beam Epitaxy," Appl. Phys. Lett., Vol. 67, No. 25, pp. 3676-3678, 1995

[36] T. Tanbun-Ek, R. A. Logan, and J. P. Van Der Ziel, "High Frequency Buried Heterostructure 1.5μm GaInAsP/InP Lasers, Grown Entirely by Metalorganic Vapour Phase Epitaxy in Two Epitaxial Growth Steps," Electron. Lett., Vol. 24, No. 24, pp. 1483-1484, 1988.

Chapter III

Carrier Lifetime Measurements in InAsP Lasers

Carrier lifetime measurements are fundamental to understanding the basic operation of semiconductor lasers. Many semiconductor laser parameters such as threshold current, internal loss, material gain, index of refraction, and line-width depend on carrier density. Unfortunately, carrier density is not a directly observable or controllable quantity. However, one can calculate the carrier density from a measurement of the carrier lifetime as a function of injection current. This is accomplished through the use of sub-threshold laser rate equations, and the results are therefore subject to all the limitations and assumptions of these equations. However, if done properly, the calculated carrier density as a function of current can be used to study the basic laser properties that are directly dependent on carrier density.

On an even more fundamental level, the carrier lifetime versus bias current allows us to extract the carrier recombination coefficients. These coefficients tell us the importance of the different recombination processes: defect, radiative, and Auger, which comprise the current flowing into the active region of the laser. Knowledge of the relative strength of these processes as a function of laser temperature, bias current, and structure is essential to designing and building better lasers. Different techniques have been implemented to measure carrier lifetime, such as, turn on delay, laser impedance, and optical. These techniques and the lifetime results of measurements on InAsP/InGaAsP QW lasers are presented next.

3.1) Turn on Delay

The lasing delay from the start of an injected current pulse has been used to determine carrier lifetimes in semiconductor lasers [1]-[4]. The experimental setup for this type of measurement is shown in figure 3.1 where a DC bias current and a current pulse are summed by the bias tee and applied to the laser diode. The optical response of the laser is measured by a fast photodiode using a sampling oscilloscope. The most critical aspect of this measurement is the pulse generation. Since the turn on delays can be as short as a few hundred picoseconds, very fast rise time pulses are needed. In addition to needing very fast rise times, we also need very large current pulses for one of the turn on delay measurements, as will be shown later. The combination of fast rise time

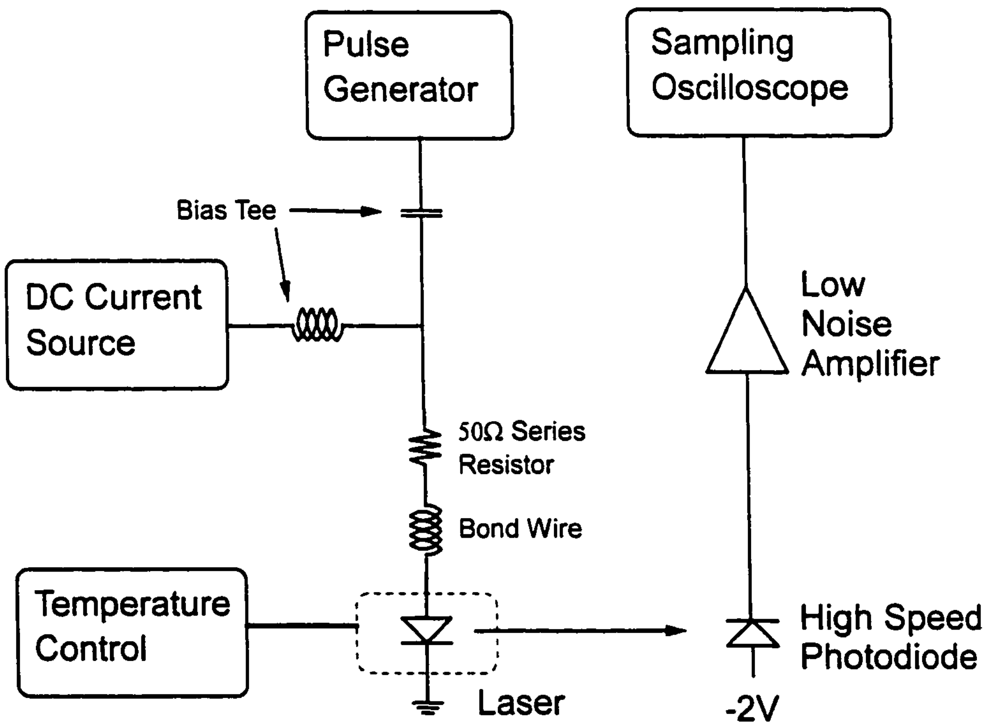

Fig 3.1 - Experimental setup of turn on delay measurement

and large current pulses is very difficult and expensive to achieve, limiting the usefulness of this type of measurement.

To understand how we get the carrier lifetime from a measurement of the turn on delay we must start from the sub-threshold carrier rate equation:

$$\frac{dn}{dt} = \frac{\eta_{inj} I}{qV} - \frac{n}{\tau(n)} \tag{3.1}$$

where I is the current pulse height and $\tau(n)$ is the carrier density dependent recombination lifetime as defined in eqn. (2.10). Rearranging this equation and integrating from the start of the current pulse at t=0 and carrier density n_0, to the onset of lasing at t=T and $n=n_{th}$ we obtain the turn on delay T.

$$\int_0^T dt = T = \int_{n_0}^{n_{th}} \frac{1}{\dfrac{\eta_{inj} I}{qV} - \dfrac{n}{\tau(n)}} dn \tag{3.2}$$

The general expression for turn on delay above can be simplified under various special conditions to yield either the carrier lifetime at threshold, τ_{th}, or the differential carrier lifetime at threshold, τ'_{th}, directly.

Dixon and Joyce showed that if the current pulse, I, is slightly higher than the threshold current, I_{th}, and the dc bias current, I_0, is allowed to approach I_{th}, then in this limit, eqn. (3.2) reduces to [1].

$$T = \tau'_{th} \ln\left(\frac{I - I_0}{I - I_{th}}\right) \qquad I_0 \to I_{th} \tag{3.3}$$

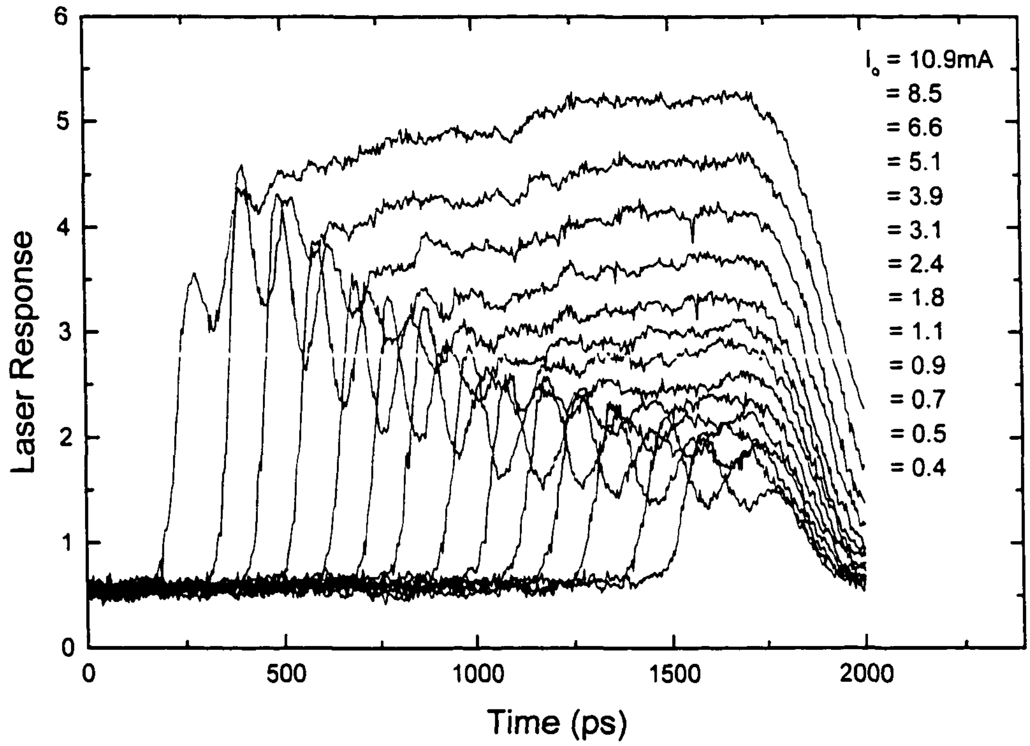

Fig. 3.2 - Typical turn on delay versus laser prebias

This approach to the turn on delay time produces the family of response curves shown in fig 3.2, where the turn on delay time is found from the 50% point of the rising edge of a given curve. As I_0 approaches I_{th} the quantity inside the natural log of eqn. (3.3) goes to zero and we can determine τ'_{th} from the slope of the data at this limit. In figure 3.3 we plot the turn on delay data collected from the shallow well InAsP buried heterostructure lasers versus the normalized laser prebias. As anticipated from eqn. (3.3) the data is nearly linear when I_0 is not too far from I_{th} (i.e. $I_0 > 0.5I_{th}$). The differential carrier lifetime at threshold, τ'_{th}, is found from the slope of this linear region and in these lasers is 1.7 ns.

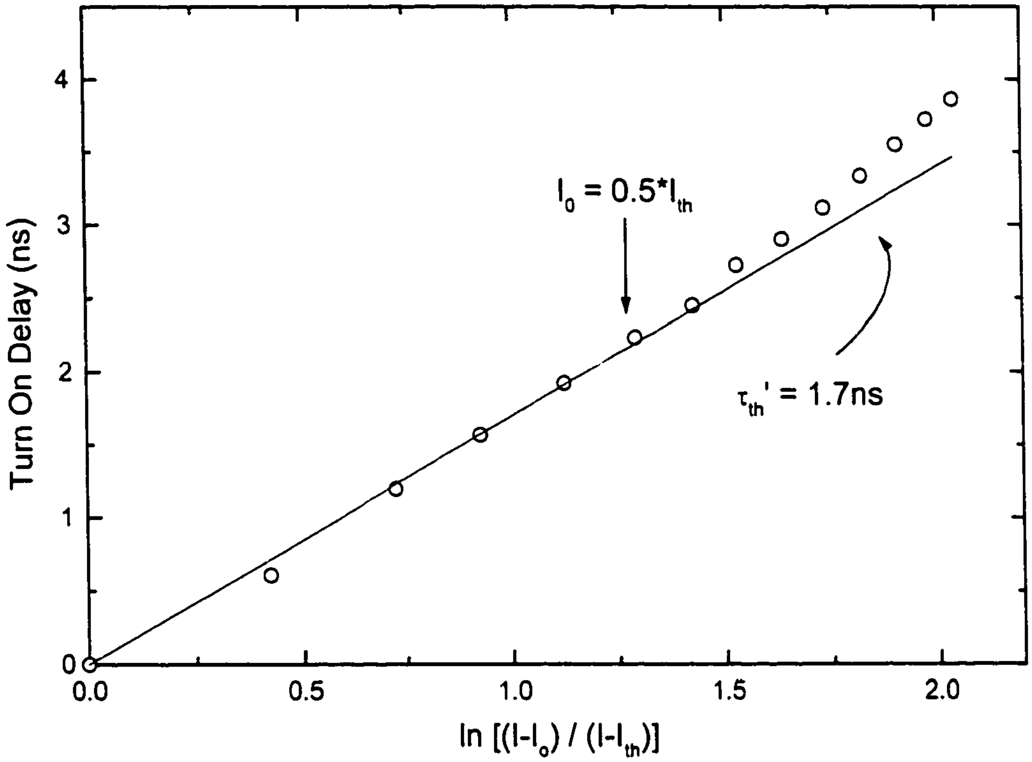

Fig. 3.3 - Turn on delay of shallow well InAsP laser vs. normalized laser prebias under conditions for differential lifetime extraction.

Using the turn on delay technique we can also measure the total carrier lifetime at threshold, τ_{th}. To accomplish this the DC prebias is set to zero and a progressively larger current pulse is injected ($I \rightarrow \infty$). Under these conditions the general turn on delay equation simplifies to [1]:

$$T = \tau_{th} \frac{I_{th}}{I} \qquad I \rightarrow \infty \tag{3.4}$$

and the limiting slope at large pulses is τ_{th}. This is inherently a more difficult experiment to control since the laser is not prebiased. The diode therefore has a dynamically changing differential resistance at the important region near the beginning of the current pulse. Since the current pulse is generated with a voltage pulse into a series resistor and

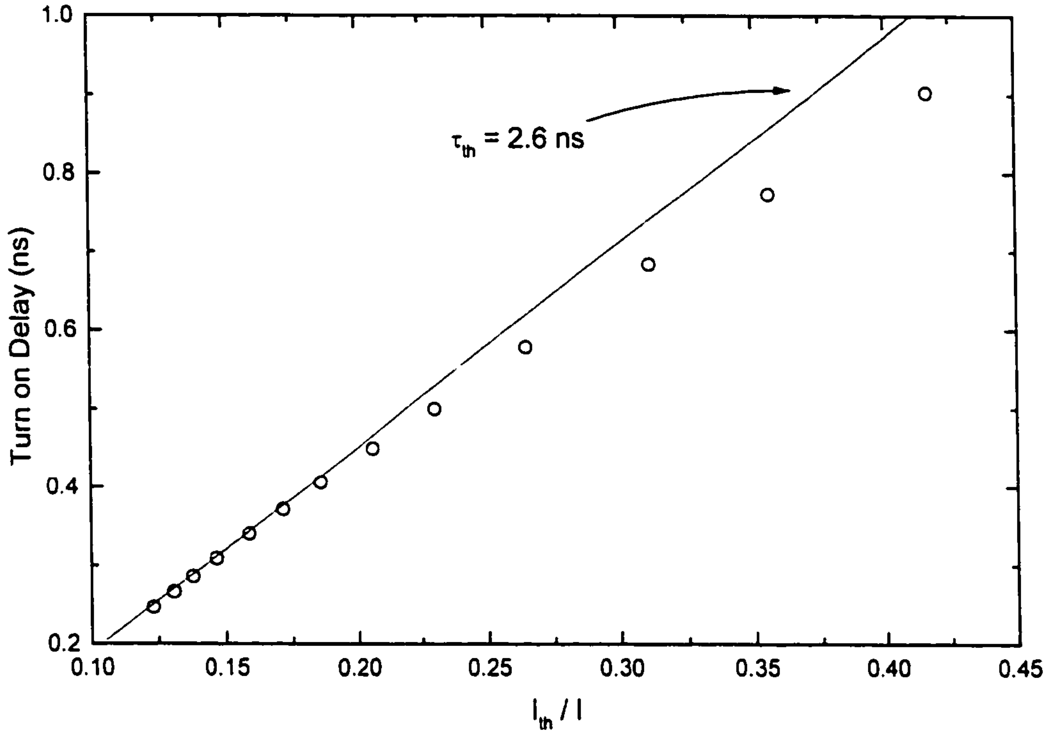

Fig. 3.4 - Turn on delay of shallow well InAsP laser versus normalized inverse pulse height as the pulse height is increased and zero prebias.

the laser diode, the changing diode resistance produces a changing current. Even so, with large current pulses we do find a linear region, as shown in Figure 3.4, where the fitted slope of 2.6 ns is the total carrier lifetime at threshold. We also see that the turn on delay data does not become linear until the pulse height is more than 5 times the threshold current. This can require a considerable voltage pulse into 50 Ω if the laser threshold current is high. The most limiting characteristic of measuring the carrier lifetime from the turn on delay data is that we only measure the carrier lifetimes at threshold. These numbers are somewhat useful, especially the total lifetime at threshold, which allows us to determine the carrier density at threshold through the steady state solution of eqn (3.1).

$$\frac{\eta_{inj} I_{th}}{qV} = \frac{n_{th}}{\tau_{th}} \tag{3.5}$$

We do not, however, get the carrier lifetime versus current and thus we cannot determine the recombination coefficient or obtain carrier density versus current relationship.

3.2) Small Signal Modulation Optical Response

Another frequently used method for obtaining the carrier lifetime is the small signal optical response technique [5]-[7]. In this method the differential carrier lifetime is obtained by fitting the measured sub-threshold small signal optical response to a single pole response derived from an analysis of the rate equations. A diagram of the experimental setup for this measurement is shown in figure 3.5. As in the turn on delay measurement a bias tee is used to sum the DC and AC components of the signal to be fed

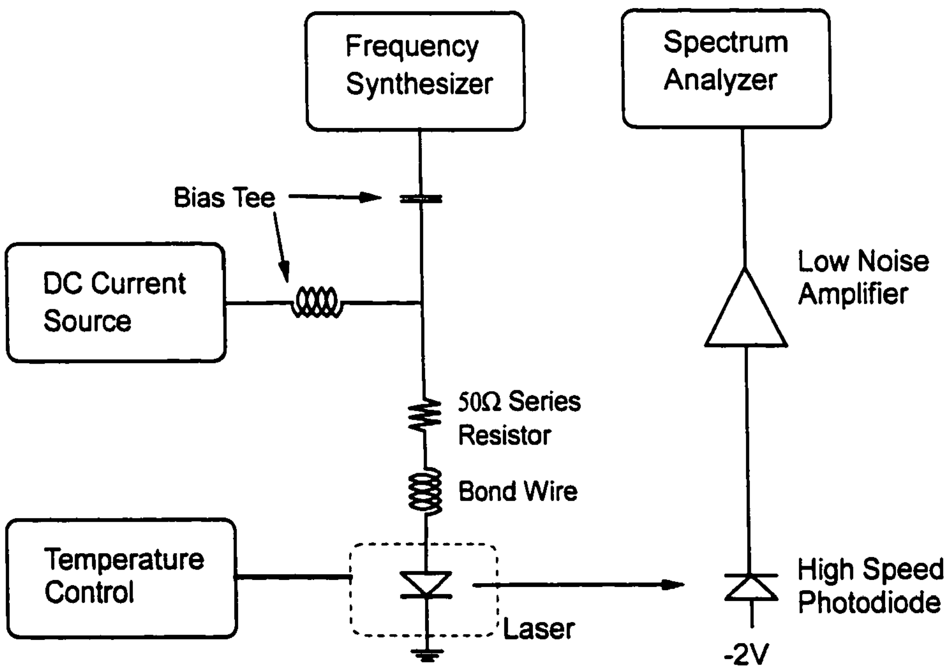

Fig 3.5 - Experimental setup of small signal optical response measurement used to obtain carrier lifetime

to the laser, the difference is that the AC component is a "small" sinusoid instead of a pulse. In the rate equation analysis to follow we assume that the AC signal is small compared to the DC signal and we find experimentally that keeping the AC component to 10% or less of the DC bias was sufficient to provide good results. The output of the laser is focused onto a photodiode, amplified by a low noise preamplifier, and measured on a spectrum analyzer that is frequency locked to the signal source. This technique has many advantages over the turn on delay technique mainly stemming from the fact that it is a small signal AC measurement instead of a large signal pulse measurement. This greatly relaxes the signal generation and detection equipment requirements, and since it is a synchronous measurement, the noise can be made quite low simply by decreasing the detection bandwidth. In addition, since the AC signal is small compared to the DC bias the carrier density does not change appreciably during the measurement and the lifetime we measure is the differential carrier lifetime at the carrier density determined by the DC bias. Thus by measuring the response at different DC bias currents we obtain the differential carrier lifetime as a function of current. This allows the determination of the actual recombination coefficients by simultaneous curve fitting of the lifetime as a function of carrier density and the current as a function of carrier density equations as is described in chapter 4.

The theory used to obtain the carrier lifetime from the sub-threshold laser rate equations is again developed from the rate equations, but unlike the turn on delay this analysis requires both the carrier and the photon rate equation. Since we are interested in the sub-threshold behavior the stimulated terms are left out and we write the rate equations as.

$$\frac{dn}{dt}=\frac{I}{qV}-\frac{n}{\tau} \tag{3.6a}$$

$$\frac{ds}{dt}=\frac{\beta n}{\tau}-\frac{s}{\tau_p} \tag{3.6b}$$

For a small signal analysis we can write the current (I), carrier density (n), and photon density (s) as a DC term plus a small AC term:

$$I = I_0 + i_1 e^{j\omega t} \qquad n = n_0 + n_1 e^{j\omega t} \qquad s = s_0 + s_1 e^{j\omega t} \tag{3.7}$$

where $i_1 \ll I_0$, $n_1 \ll n_0$, and $s_1 \ll s_0$. If we substitute these expressions into equations (3.6a) and (3.6b) and separate the time dependent and time independent terms the time dependent equations are.

$$j\omega n_1 = \frac{i_1}{qV}-\frac{n_1}{\tau'} \tag{3.8a}$$

$$j\omega s_1 = \frac{n_1}{\tau'}-\frac{s_1}{\tau_p} \tag{3.8b}$$

These two equations can be solved for the small signal optical response, s_1, yielding.

$$|s_1| = \frac{\beta i_1}{\tau q V}\left[\frac{1}{\left(\omega^2+\frac{1}{\tau_p{}^2}\right)\left(\omega^2+\frac{1}{\tau'^2}\right)}\right]^{1/2} \tag{3.9}$$

With the assumptions that i_1 is constant in frequency and that the pole due to the photon lifetime is at much higher frequencies than we are interested in, i.e $\omega \ll 1/\tau_p$, the above equation simplifies to.

$$|s_1| = \frac{\beta \tau_p i_1}{qV\tau'}\frac{1}{\sqrt{1/\tau'^2+\omega^2}} = \frac{R_o}{\sqrt{1+\omega^2\tau'^2}} \tag{3.10}$$

Equation (3.10) is a simple, single pole response function, with the pole being determined by the differential carrier lifetime. A typical laser frequency response curve with a fit to equation (3.10) is shown in figure 3.6 for the same InAsP/InGaAsP laser that was used for the turn on delay experiments. This curve has been calibrated by subtracting off the measured above threshold laser frequency response. This calibration removes source, cable, amplifier, and receiver non-linearity, in addition to parasitic laser capacitance and bond wire inductance. We see that the fit is very good across the frequency range indicating that the calibration was successful. This particular curve was taken very near threshold and the differential carrier lifetime is found to be 1.69 ns. This is in excellent

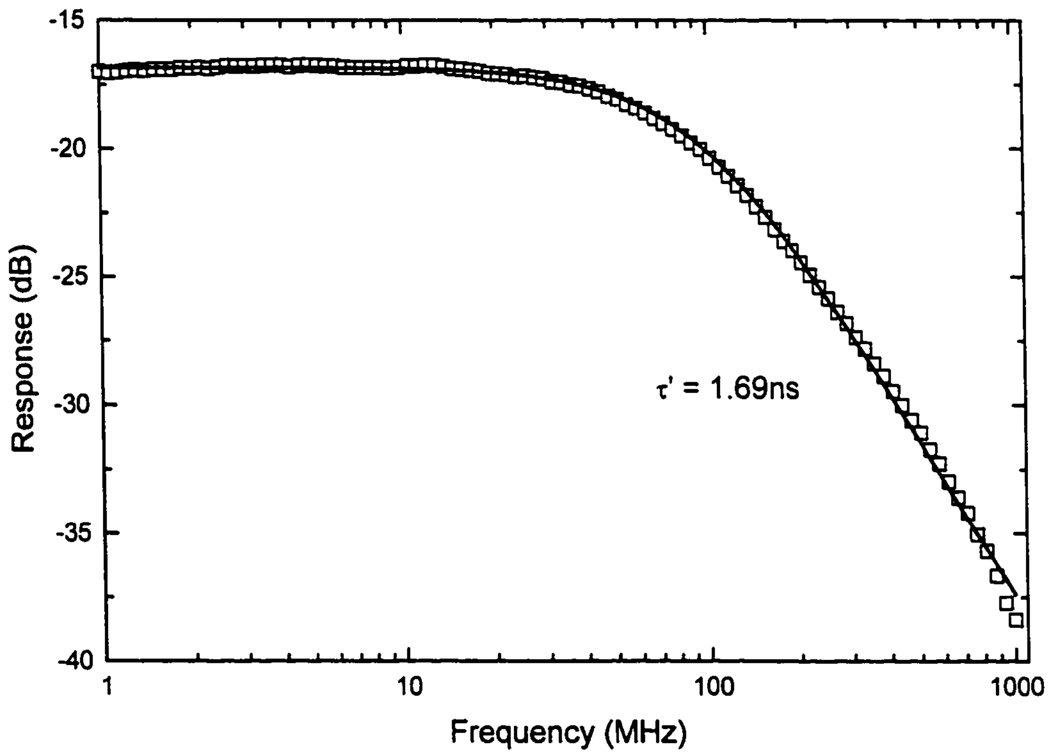

Fig. 3.6 - Typical sub-threshold frequency response curve of shallow well InAsP laser with single pole fit

agreement with the turn on delay data that indicated that the differential lifetime at threshold was 1.7 ns.

As discussed previously, the biggest advantage of this technique is that we can measure the differential carrier lifetime, τ', as a function of bias current. A plot of the variation of τ' with bias current is shown for the shallow well InAsP laser in figure 3.7, where we can see that the differential lifetime initially increases as the bias current

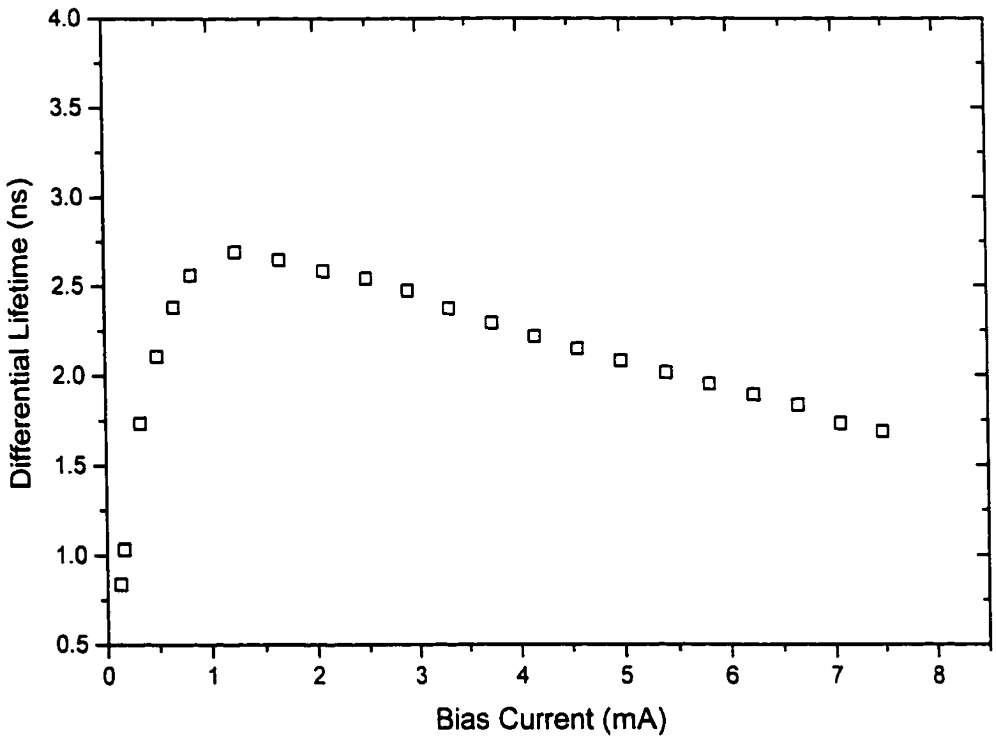

Fig. 3.7 - Differential carrier lifetime versus bias current of shallow well InAsP laser at T=20°C

decreases. However, at around 1.5 mA the lifetime reaches a peak and then begins to decrease as the bias current is decreased further. This effect was initially attributed to an unknown nonradiative recombination process that was dependent on the square root of carrier density [6]. It was not until considerably later that it was discovered that this

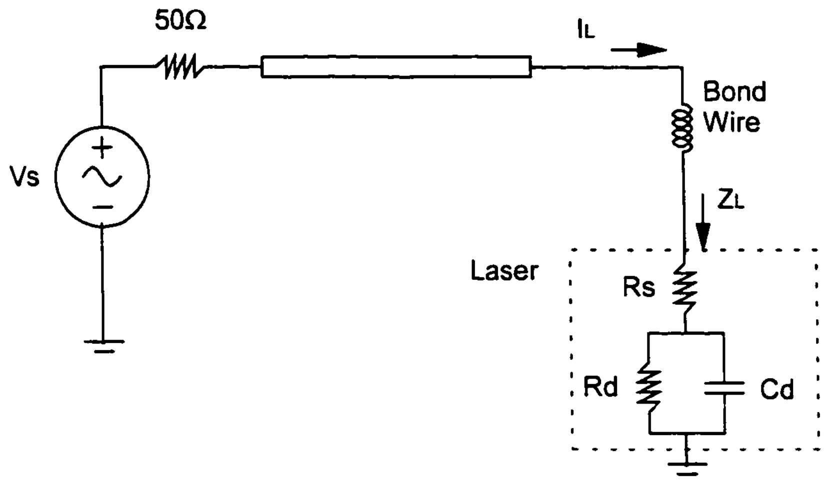

Fig. 3.8 - Electrical circuit model for laser and drive electronics

effect was really due to increasing laser impedance at low bias current [8],[9]. The laser impedance not only increases as the laser bias is lowered but also becomes increasingly frequency dependent. Since we assumed in equation (3.10) that the modulation current was frequency independent the lifetime we obtain from the fit is incorrect. We can correct for this effect if we assume that the laser diode has the equivalent circuit model shown in figure 3.8 and thus the frequency dependent laser impedance is of the form

$$Z_L(\omega) = R_s + \frac{R_d}{1 + j\omega R_d C_d} \qquad \text{with} \qquad \tau' = R_d C_d \tag{3.11}$$

where R_s is the series resistance of the diode, R_d is the current dependent diode resistance, and τ' is the differential lifetime. Assuming a 50 Ω voltage source driving the combination of the 50 Ω series resistor and laser diode impedance of eqn. (3.11), a correction to the measured lifetime for the laser impedance can be derived [9].

$$\tau'_{corr} = \tau'\left(1 + \frac{R_d}{R_s + 50\Omega}\right) \tag{3.12}$$

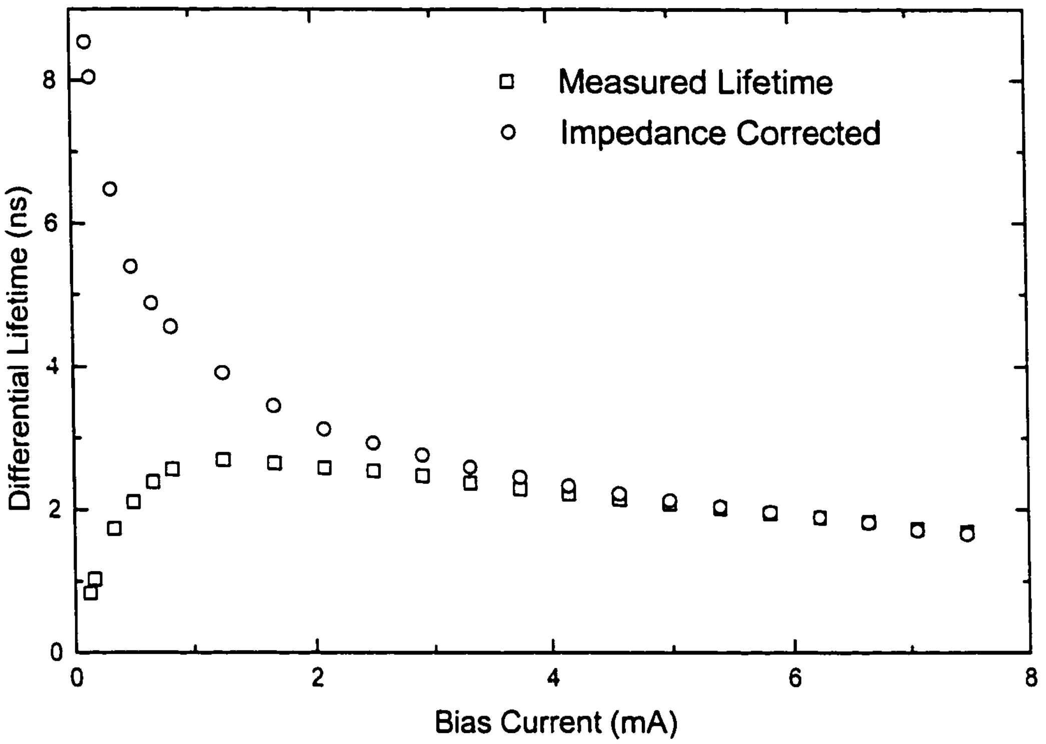

Fig. 3.9 - Impedance corrected differential carrier lifetime vs. bias current for shallow well InAsP laser

Using this correction equation we obtain the impedance corrected curve as also shown in figure 3.9. Here we see that the largest correction occurs at low bias, as expected, and that the corrected data shows no saturation to currents as low as 0.16 mA. However, equation (3.12) is not always valid. The electrical impedance model used for the laser diode does not take into account the parasitic bond wire inductance, typically on the order of 0.5 nH, which can introduce error into the correction. In addition, it is necessary to measure the diode series and differential resistance at each bias level to correctly obtain the lifetime, making this technique time consuming. Another disadvantage of this technique is the large impedance mismatch that occurs at the laser diode. This mismatch causes some of the incident electrical power to be radiated out and mistakenly picked up by the receiver. The cross-talk generated can be larger than the detected optical signal in these sub-threshold measurements thus affecting the measured response.

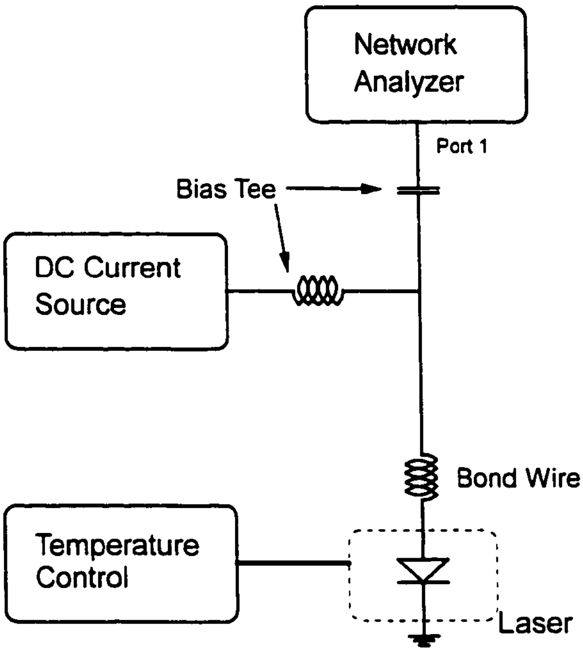

Fig 3.10 - Experimental setup of small signal impedance measurement used to obtain carrier lifetime

3.3) Small Signal Electrical Impedance

Another alternative for measuring the differential carrier lifetime is the purely electrical technique of measuring the differential electrical impedance of the laser diode, also described in Refs. [8],[9]. This technique uses a network analyzer to obtain the laser diode impedance from the measured reflection coefficient as shown in figure 3.10. Calibration is completed using standard correction routines available on the network analyzer that involve placing a short, open and 50 Ω load in the laser mount. The main advantage of this technique is simplicity, since there is no optical to electronic conversion equipment setup, alignment, and calibration are all easier. In addition only one measurement needs to be conducted, the impedance measurement, where as in the impedance corrected optical technique, we needed both the optical response and the DC impedance measurements.

The impedance measurements are done as a function of frequency and bias current and the differential lifetime is obtained from a fit of the data to an impedance equation derived from the electrical model of the laser diode, fig. 3.8.

$$Z_L(\omega) = R_s + \frac{R_d}{1 + j\omega R_d C_d} + j\omega L \qquad \text{where} \qquad \tau' = R_d C_d \tag{3.13}$$

The only difference between (3.11) and (3.13) is the inclusion of the bond wire inductance, L, which as we will see, is important at high frequency. Extracting the lifetime from the impedance data requires a fit with a model that contains four parameters, the diode series and differential resistance, the parasitic inductance, and the differential carrier lifetime. Fig 3.11 shows the measured impedance from a shallow well InAsP laser at both low bias, i.e. 0.2 mA, and near threshold (8.0 mA) along with the fit to (3.13). The low frequency impedance saturates at R_s+R_d while the high frequency rise, particularly evident in the near threshold curve, is due to the bond wire inductance. The differential carrier lifetime is mostly determined by the mid frequency transition between these two extremes. However, the large number of fitting parameters determined from one set of data, reduces the accuracy of the fitting parameters. We can also see that to properly fit this model it is necessary to make measurements at much higher frequencies (2 GHz) than is required in the optical technique (~200 MHz). This can be a problem, particularly for quantum well (QW) lasers, since transport and capture times can add

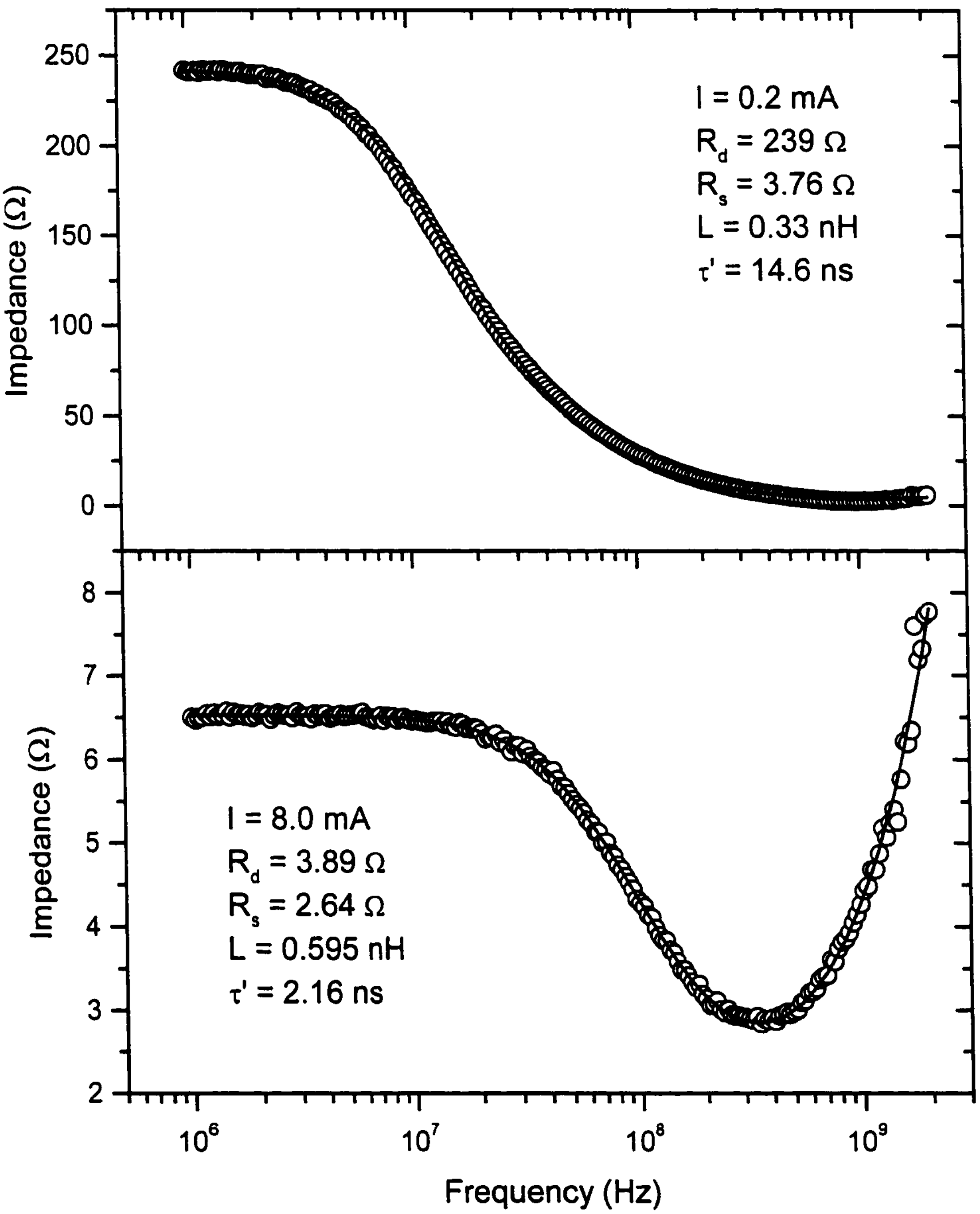

Fig. 3.11 - Fit of laser impedance data from shallow well InAsP laser to (3.13) at low bias and near threshold

additional high frequency poles and zeros to the modulation response making it more difficult to extract the carrier lifetime.

3.4) Impedance Independent Optical

We now introduce our novel technique that eliminates the electrical impedance technique's disadvantages of fitting four model parameters and requiring data to be taken at high frequencies. It also eliminates the impedance corrected optical technique's disadvantage of needing additional measurements to account for laser impedance changes. We do this by adding an impedance stabilization circuit to the traditional small signal optical response technique, thus providing a constant current modulation regardless of the laser impedance. The impedance stabilization circuit, shown in fig.

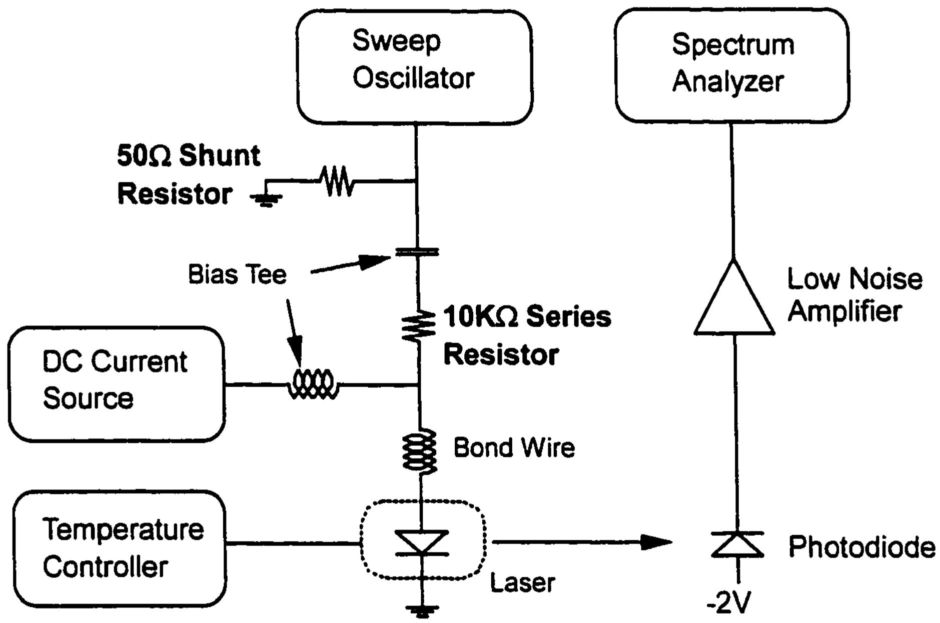

Fig 3.12 - Experimental setup of our impedance independent optical technique with impedance stabilization circuit

3.12, consists of a 10 KΩ series resistor and a 50 Ω shunt resistor. Since the differential resistance of our laser diodes varied from about 3 Ω near threshold to nearly 400 Ω at low bias and low frequencies, the addition of the 10 KΩ resistor in series with the laser kept the modulation current constant to within 5%. The 50 Ω shunt resistor placed before the series resistor, and in close physical proximity (~5 mm) to the laser, provided a matched load for the system. While it is true that most of the power is dissipated in the 50 Ω shunt resistor and very little is delivered to the laser, this is not a problem since this measurement is a small signal measurement and little power is needed. For example, a source power of 0 dBm develops approximately 224 mV across the 50 Ω shunt and therefore 22 μA into the series combination of the 10 KΩ resistor and the laser. Thus, the laser diode stays in the small signal regime even at bias levels as low as 0.2 mA. We also achieved a nearly 20 dB reduction in the level of cross-talk at the receiver with the shunt resistor in place due to the lower radiated power into the nearly matched load. This allowed us to measure the frequency response down to near the −167 dBm noise floor set by the thermal noise of the 50 Ω shunt impedance of the high speed detector.

The modulation responses obtained with our impedance independent optical technique on the shallow well 1.3 μm InAsP/InGaAsP MQW buried heterostructure lasers, described in chapter 2, are shown in fig. 3.13. As in the standard optical technique the response curves have been calibrated by subtracting off the above threshold frequency response in order to remove source, photodiode, amplifier, and cable non-linearity. Excellent fits to the theoretical single pole response were obtained at all bias currents. This indicated that device parasitics were low, or properly calibrated out, and that additional poles or zeros were not present at these relatively low frequencies (<200MHz).

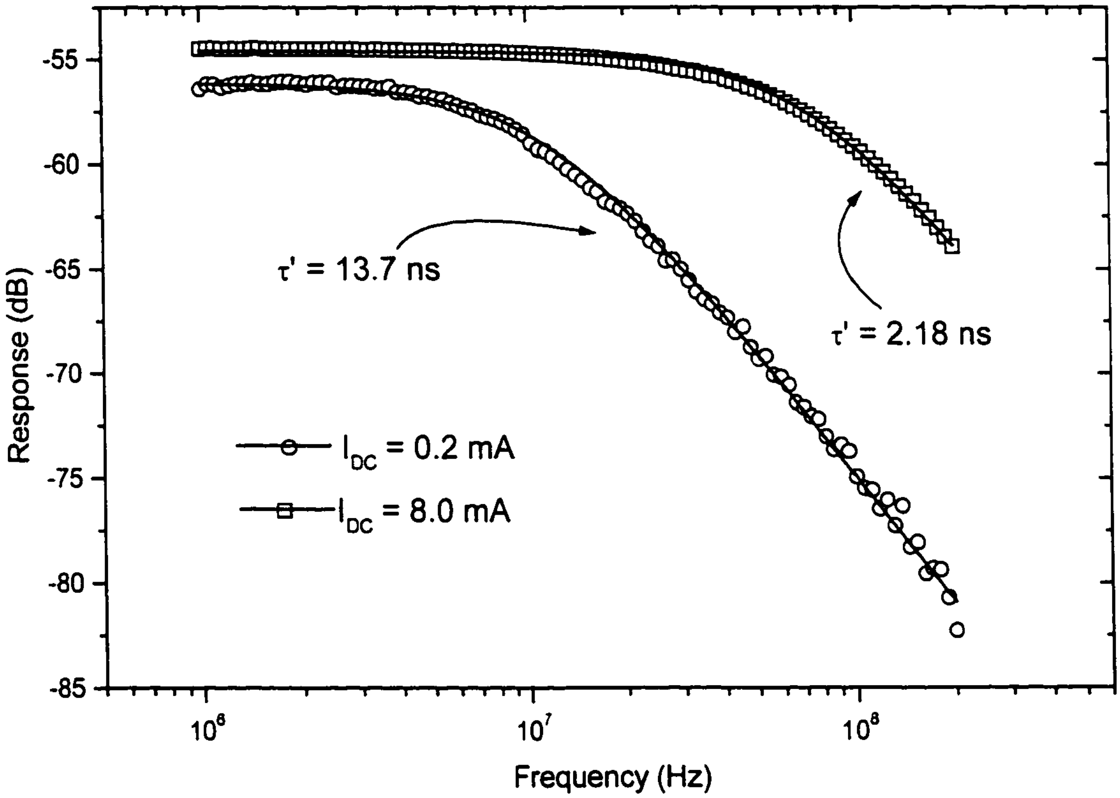

Fig 3.13 - Typical calibrated frequency response curves taken using the impedance independent optical carrier lifetime measurement

As we saw in the last section, the lasers used here required impedance data to be taken to 2 GHz in order to properly fit all four impedance model parameters. Although we saw no evidence that additional high frequency poles and zeros were present in these lasers, even up to 2 GHz, they are a problem in some QW lasers. Carrier transport and capture processes generate additional high frequency structure, as shown in the experiments of S. Weisser, I. Esquivias et. al. [10][11], and make it difficult to extract the carrier lifetime.

Excellent agreement between the lifetime data taken via the electrical impedance technique and our impedance independent optical technique was obtained. As shown in

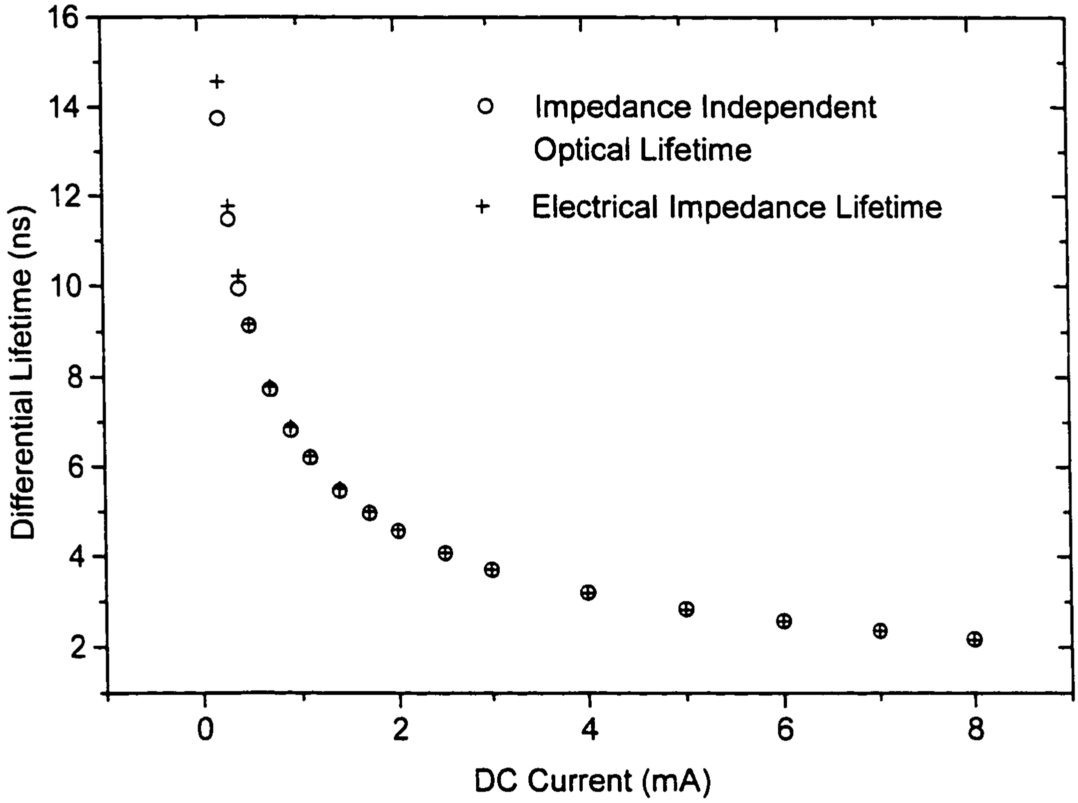

Fig 3.14 - Comparison of carrier lifetimes obtained from the impedance independent optical and electrical impedance techniques

fig. 3.14, both techniques clearly measure the same carrier lifetime, which does not saturate or decrease at low bias. How these lifetimes are used to extract useful information on recombination processes and carrier density is described in the next chapter.

References For Chapter III

[1] R. W. Dixon and W. B. Joyce, "Generalized Expressions for the Turn-On Delay in Semiconductor Lasers," J. Appl. Phys., Vol. 50, No. 7, pp. 4591-4595, 1979.

[2] E. Adomaitia, P. Blixt, and A. Krotkus, "Optoelectronic Measurement of Picosecond Turn-On-Delay in InGaAsP Laser Diodes," Appl. Phys. Lett., Vol. 54, No. 26, pp. 2622-2624, 1989.

[3] N. K. Dutta, N. A. Olsson, H. K. Temkin, R. A. Logan, and T. Tanbun-Ek, "Linewidth Enhancement Factor and High Temperature Performance of 1.48 μm Strained InGaAs-InGaAsP Multiquantum Well Lasers," IEEE J. Quantum Electron., Vol. 27, No. 3, pp. 678-680, 1991

[4] T. Fukushima, A. Kasukawa, M. Iwase, T. Namegaya, and M. Shibata, "Small Turn-On Delay Time in 1.3 μm InAsP/InP Strained Double Quantum-Well Lasers With Very-Low Threshold Current," IEEE Photon. Technol. Lett., Vol. 5, No. 2, pp. 117-119, 1993

[5] R. Olshansky, C. B. Su, J. Manning, and W. Powazinik, "Measurement of radiative and nonradiative recombination rates in InGaAsP and AlGaAs light sources," IEEE J. Quantum Electron., Vol. 20, pp. 838-854, 1984

[6] R. Olshansky, J. LaCourse, T. Chow, and W. Powazinik, "Measurement of radiative, Auger, and nonradiative Currents in 1.3-μm InGaAsP Buried Heterostructure Lasers," Appl. Phys. Lett., Vol. 50, No. 6, pp. 310-312, 1987

[7] Y. Zou, J. S. Osinski, P. Grodzinski, P. D. Dapkus, W. C. Rideout, W. F. Sharfin, J. Schlafer, and F. D. Crawford, "Experimental Study of Auger Recombination, Gain, and Temperature Sensitivity of 1.5μm Compressively Strained Semiconductor Lasers," IEEE J. Quantum Electron., Vol. **29**, No. 6, pp. 1565-1575, 1993

[8] G. E. Shtengel, D.A. Ackerman and P.A. Morton, "True Carrier Lifetime Measurements of Semiconductor Lasers," Electron. Lett., Vol. 31, No. 20, pp. 1747-1748, 1995

[9] G. E. Shtengel, D. A. Ackerman, P. A. Morton, E. J. Flynn, and M. S. Hybertsen, "Impedance-corrected carrier lifetime measurements in semiconductor lasers," Appl. Phys. Lett., Vol. 67, No. 11, pp. 1506-1508, 1995.

[10] S. Weisser, I. Esquivias, P. J. Tasker, J. D. Ralston, B. Romero, and J. Rosenzweig, "Impedance Characteristics of Quantum-Well Lasers," IEEE Photon. Technol. Lett., Vol. 6, No. 12, pp. 1421-1423, 1994.

[11] I. Esquivias, S. Weisser, B. Romero, J. D. Ralston, and J. Rosenzweig, "Carrier Capture and Escape Times in $In_{0.35}Ga_{0.65}As$-GaAs Multiquantum-Well Lasers Determined from High-Frequency Electrical Impedance Measurements," IEEE Photon. Technol. Lett., Vol. 8, No. 10, pp. 1294-1296, 1996

Chapter IV

Rate Equation Analysis and Recombination Coefficients

As shown in chapters II and III, there are several different definitions of carrier lifetime and several different methods of obtaining these lifetimes. The most useful lifetime is the differential carrier lifetime, τ', which obtained as a function of bias current, allows for determination of the carrier recombination coefficients of the active region material. This is accomplished by fitting the measured bias dependence of the differential carrier lifetime to equations obtained from an analysis of the laser sub-threshold rate equations. As we will show, the results of this analysis depend strongly on the rate equation model used and as such the analysis is very different for bulk and quantum well lasers.

4.1.1) Bulk Laser Analysis

The standard analysis of the carrier lifetime was developed for bulk lasers and was derived from the single carrier level rate equations (3.6), which are valid for these lasers [1]-[3]. In chapter III we used these equations to obtain the sub-threshold frequency response of the laser diode. Here we show how to obtain the recombination coefficients from these same equations and the measured differential carrier lifetime versus bias current. While this theory is derived from rate equations that are applicable only to bulk active region lasers, it has been repeatedly applied to QW lasers [4]-[7] by assuming that all injected carriers fall immediately into the wells and stay there until they recombine.

Under this assumption we can extract the recombination coefficients from $\tau'(I)$ using only the bulk carrier rate equation, which we repeat here for convenience.

$$\frac{dn}{dt} = \frac{\eta_{inj} I}{qV} - \frac{n}{\tau} \tag{4.1}$$

Combining the steady state version of this equation (dn/dt=0) with the definition of the recombination rate expressed in (2.10), we can write a relationship between the bias current I and the carrier density n_{eff}.

$$I = \frac{qV}{\eta_{inj}} \frac{n}{\tau} = \frac{qV}{\eta_{inj}} \left(A_{eff} n_{eff} + B_{eff} n_{eff}^{2} + C_{eff} n_{eff}^{3} \right) \tag{4.2}$$

In this equation we have explicitly written the carrier density as well as the recombination coefficient A_{eff}, B_{eff}, and C_{eff} as effective parameters. We do this to distinguish these parameters from the parameters we will obtain in the more complicated QW analysis in the next section. We can also relate the differential carrier lifetime to the carrier density through the definition of the lifetime.

$$\frac{1}{\tau'(n_{eff})} = \frac{dR(n_{eff})}{n_{eff}} = A_{eff} + 2B_{eff} n_{eff} + 3C_{eff} n_{eff}^{2} \tag{4.3}$$

Thus we can measure the differential carrier lifetime as a function of bias current with one of the methods outlined in chapter 3, and by simultaneously fitting equation (4.2) and (4.3), we can obtain not only the recombination coefficients but also the carrier density as a function of bias current $n_{eff}(I)$ through (4.2). This is very important since carrier density, not current, is the fundamental operating parameter upon which nearly all internal laser characteristics depend. Thus while the carrier density cannot be measured directly, the relationship in eqn. (4.2) allows us to move from the measured current to carrier density.

4.1.2) Shallow versus Deep Well

We are now in the position to look at some of the results obtained using the bulk rate equation analysis on the carrier lifetime data collected in this thesis work. The data were taken on the InAsP/InGaAsP MQW lasers described in chapter 2 where we referred to the two different structures as the shallow and deep well lasers based on the level of

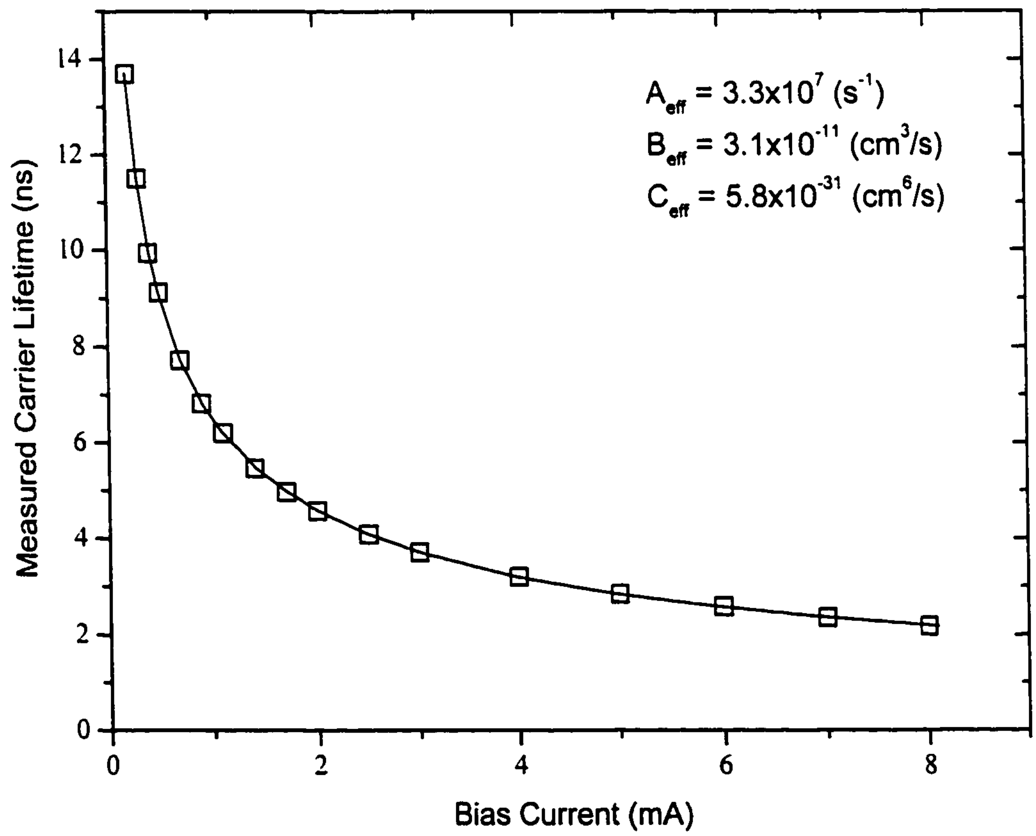

Fig. 4.1 - Measured carrier lifetime vs. bias current for shallow well laser at 20°C with extracted recombination coefficients

confinement in the QW. The lifetime was obtained from the sub-threshold small signal response data collected using the impedance independent optical technique outlined in chapter 3. The carrier lifetime measurements were conducted at bias currents ranging from near threshold down to around 0.2 mA where the spontaneous emission response was still sufficiently above the noise floor of the detection system to obtain reliable data. The measured differential carrier lifetime versus bias current, as well as the fitted recombination coefficients, are shown in fig. 4.1 for the shallow well laser sample. While the fit is excellent some of the extracted recombination coefficients are somewhat unusual. The extracted A coefficient is reasonable at around 3.3×10^{7} s^{-1} indicating excellent well/barrier interface quality as well as material quality. However, the radiative coefficient is found to be 3.1×10^{-11} cm^3/s, which is lower than the typical bulk number of $\sim1\times10^{-10}$ cm^3/s [2],[3],[8]. In addition, the C coefficient, which has a very wide range of reported values in bulk material, 1×10^{-29} to 9×10^{-29} cm^6/s [2],[3],[8], falls considerably outside of this range at 5.8×10^{-31} cm^6/s. While it has been speculated theoretically [9]-[11], and reported experimentally [4], that strain can reduce the Auger recombination rate, our Auger coefficient seems too good to be true. Indeed, as discussed previously, there have been several reports that laser structure, in particular confinement energy, can affect the lifetime measurements and the extracted recombination coefficients in QW lasers [12]-[14]. These reports show that the lifetime is longer in QW lasers with lower barrier heights and/or larger barrier/SCH layers thus leading to lower recombination coefficients. This effect is the result of carriers spilling out of the QW and into the barrier/SCH region. The carriers in the barrier/SCH regions have a much lower carrier density and therefore longer lifetime. Since the barrier/SCH carriers are essentially in thermal equilibrium with the well carriers, i.e. they share a quasi-Fermi level, the measured lifetime is a weighted average of the lifetime of the well and barrier/SCH carriers and is thus longer than the well lifetime. The smaller extracted recombination coefficients are a direct result of the longer measured lifetime.

In order to see if the carrier population in the barrier/SCH region produced invalid recombination coefficients in the analysis of the carrier lifetime data for our lasers, we also collected lifetime data on the deep well laser structure with the results shown in figure 4.2. Lifetime data for the deep well laser was collected on both broad area (BA) devices of 90μm stripe width and buried heterostructure (BH) lasers with 1.4μm width. This was done to increase the current density range over which lifetime data was available and thus improve the sensitivity of the fitting procedure to the recombination coefficients, particularly A and B. With this additional data available we chose to obtain the A and B coefficients from the BA data and the C coefficient from the BH data. This procedure was performed in a self-consistent and iterative manner until a single solution was found. By using this method we were able to obtain each recombination coefficient from the data covering the carrier density range where that mechanism was most important. The results are shown in figure 4.2, where (a) shows the BA carrier lifetime data and (b) is the BH lifetime data. Note that the current density range of the BA data is from ~1mA/cm^2 to ~35mA/cm^2 while the BH lifetime data was obtained from ~30mA/cm^2 to more than 1300mA/cm^2. Thus by making use of the BA data we were able to extend the current density range over which we obtained carrier lifetime data by about a factor of 30. We can see from the figure that the fit is very good across the entire

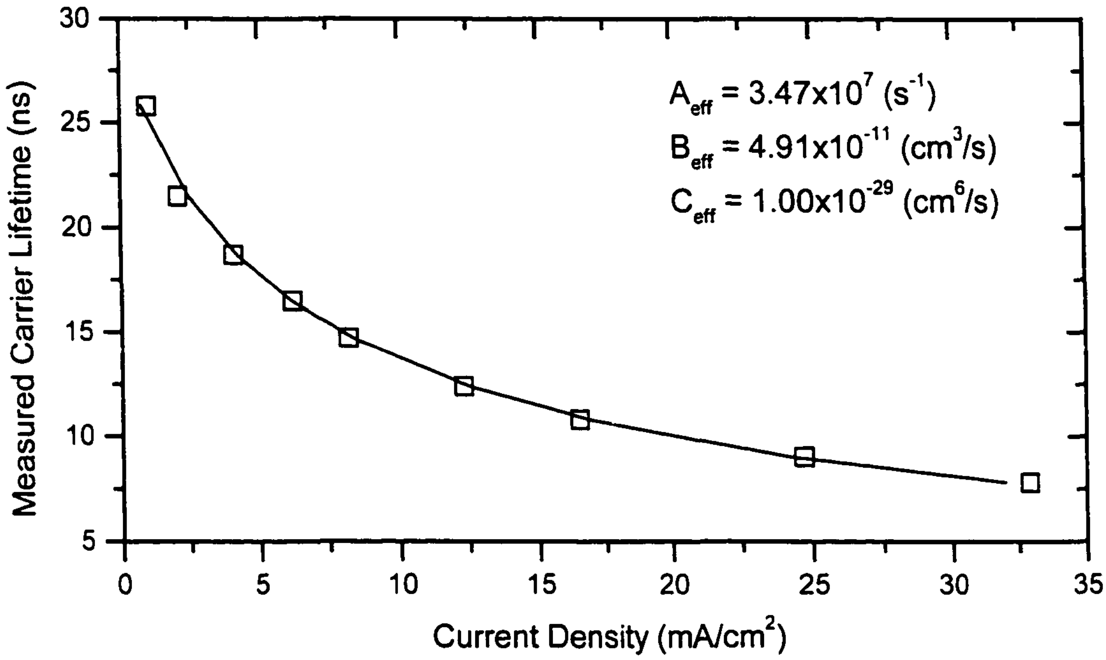

Fig. 4.2(a) - Measured carrier lifetime vs. bias current for deep well BA laser with extracted recombination coefficients

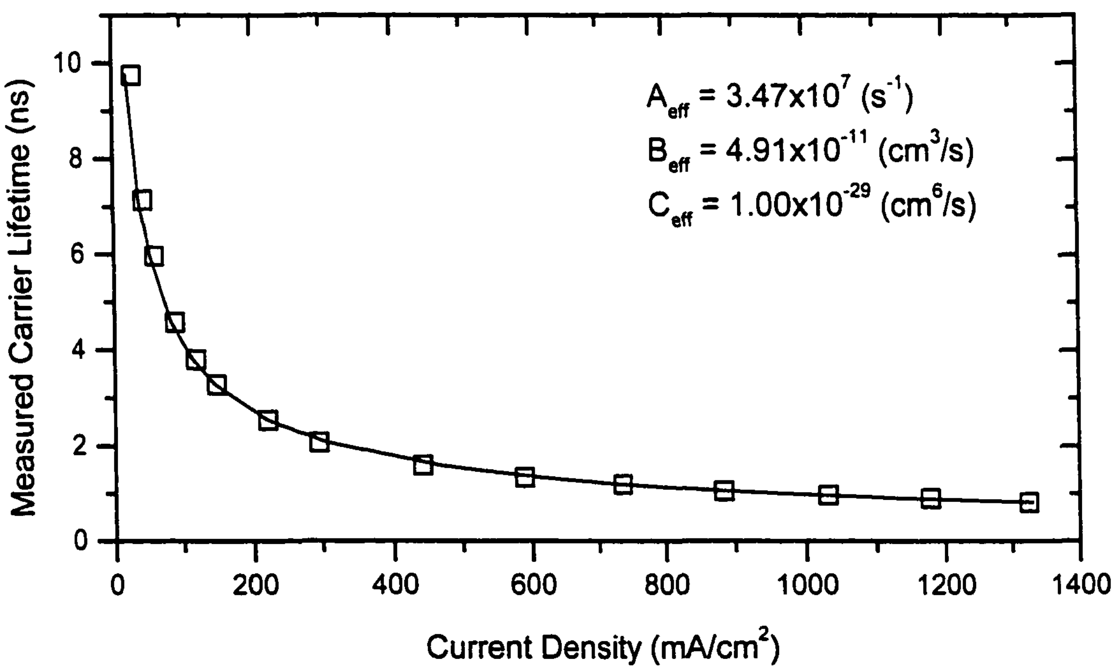

Fig. 4.2(b) - Measured carrier lifetime vs. bias current for deep well BH laser with extracted recombination coefficients

range of current density with a single set of recombination parameters. The A coefficient for the deep well laser was found to be $3.47 \times 10^{7}\ s^{-1}$ which is very close to the value obtained for the shallow well laser of $3.3 \times 10^{7}\ s^{-1}$. The B coefficient, however, increased from $3.1 \times 10^{-11}\ cm^3/s$ in the shallow well to $4.91 \times 10^{-11}\ cm^3/s$ in the deep well and the C coefficient increased dramatically from $5.8 \times 10^{-31}\ cm^6/s$ to a more reasonable $1.00 \times 10^{-29}\ cm^6/s$. These results are consistent with the effect of carrier occupation of the barrier/SCH states. Not only are the measured lifetimes longer and recombination coefficients lower in the shallow QW laser but the recombination coefficients most sensitive to carrier density, i.e. C, are the most affected. This is expected since higher carrier densities mean higher Fermi levels and thus more carriers spilling out of the QW and into the barrier/SCH regions.

4.1.3) Temperature Dependence of Recombination Coefficients

Carrier lifetime measurements were performed on the deep well lasers at temperatures from 10°C to 60°C in order to determine the temperature dependence of the extracted recombination coefficients. The results are shown in figure 4.3, where we see that the A coefficient decreases slightly with temperature, reducing by about 10% across the temperature range studied. The B coefficient appears to decrease slowly, down about 20%, from 10°C to around 40°C but increases slightly at 50°C and 60°C leaving no clear temperature trend. The temperature dependence of the C coefficient is probably the most interesting in that it shows essentially little change across the entire temperature range varying by no more than ±5%. This is consistent with other reports on Auger recombination in long wavelength QW lasers that show no temperature dependence

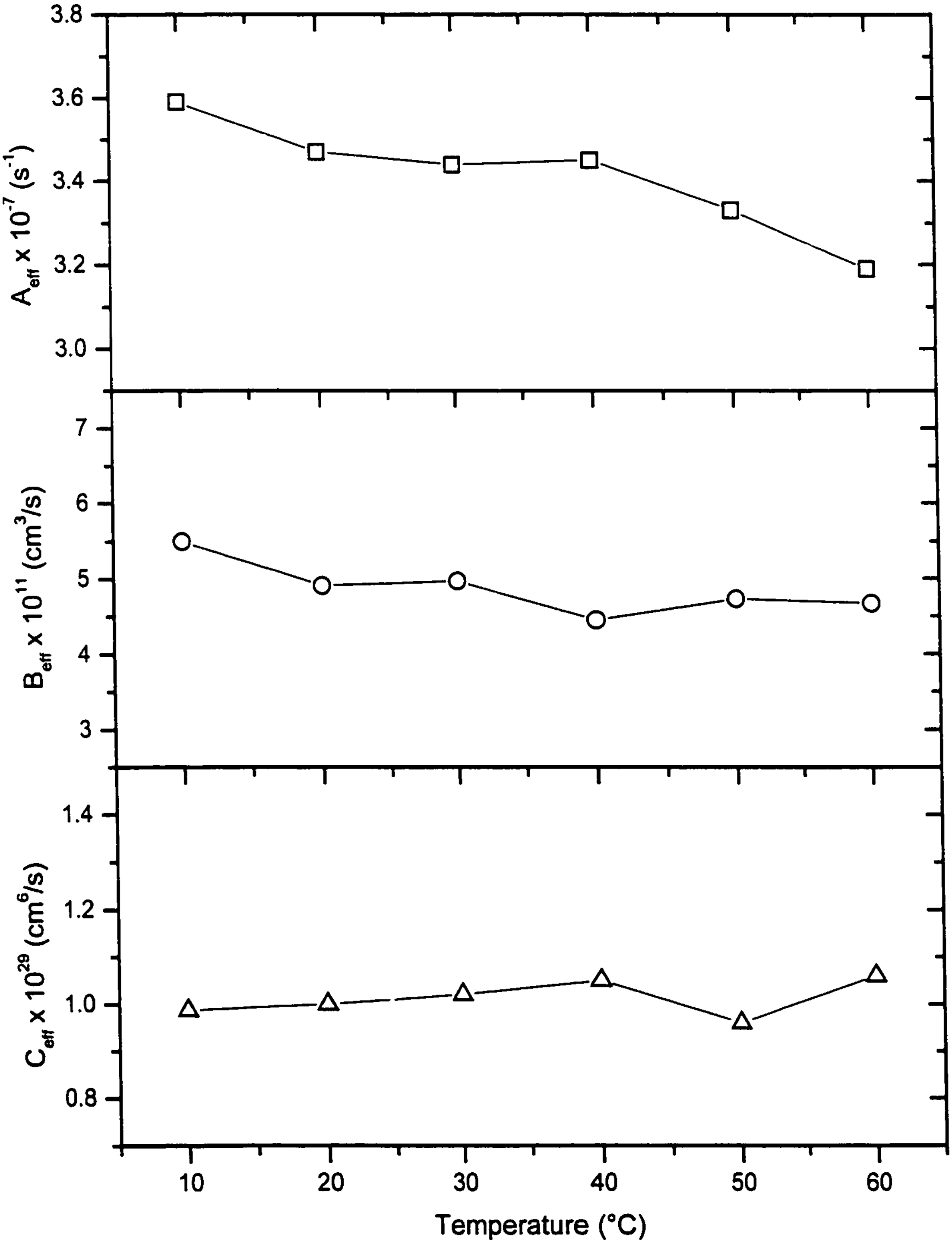

Fig. 4.3 - Temperature dependence of effective recombination coefficients for the deep well laser

[6] or even a negative dependence [4]. The measured results in QW lasers are however in direct contradiction with measurements in bulk long wavelength [3] lasers as well as theoretical predictions that the Auger coefficient should increase with temperature [8]. The unusual temperature dependence of the Auger coefficient can also be attributed to carrier population of the barrier/SCH region. Increasing the temperature is analogous to decreasing the effective barrier height thus increasing the number of carriers in the barrier/SCH region. The result is that the additional carriers spilling out of the well at higher temperatures compensate for the increasing Auger recombination and in our case nearly exactly cancel. While other theories, such as phonon assisted Auger [15], may predict a smaller increase in the Auger recombination with temperature, carrier spillover is the only theory that can explain the negative temperature dependence observed by some groups.

All of these results are consistent with the theory that carriers spilling out of the QW are affecting the carrier lifetime and the recombination coefficients. The smaller the barrier height or the higher the temperature is for a given QW laser, the easier it is for the carriers to escape from the wells and the more dramatic the effect on both the lifetime and the recombination coefficients. While the deep well laser provides a better measure of the intrinsic lifetime and recombination coefficients we don't know how close even these numbers are to the correct values.

4.2) Quantum Well Laser Analysis

In this section we will develop a new theory, specifically for QW lasers, which will not only tell us how close the deep well numbers are, but also provide us with a means for determining the intrinsic well lifetime and recombination coefficients regardless of the laser structure.

4.2.1) Quantum Well Rate Equation Analysis

The standard analysis of the carrier lifetime, described in section 4.1, is based on a single carrier level rate equation (4.1) analysis. In order for this analysis to be valid for a QW laser, all of the carriers would have to be in the well material. While it is true that typical SCH transport and QW capture times are very small compared to the sub-threshold carrier lifetime, carriers arriving at the QW region quickly come into thermal equilibrium with the carriers in the well. Therefore, in QW lasers with finite barrier height operating at nonzero temperature there will be a fraction of carriers that occupy the

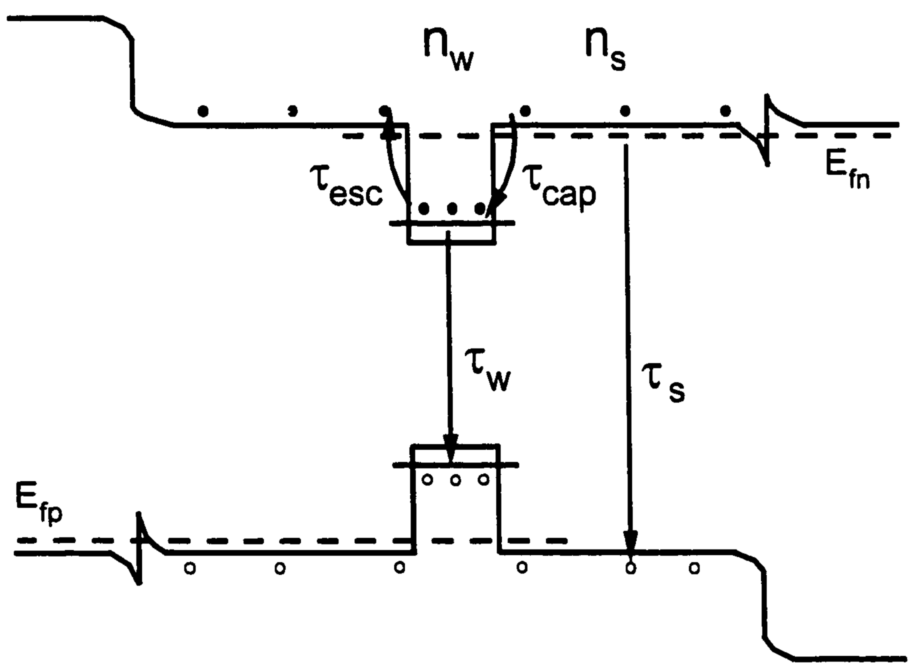

Fig. 4.4 - Schematic diagram of quatum well laser capture, escape, and recombination processes

3D states above and or outside the QW regions. The ratio of the total number of carriers outside the well to that inside is dependent on the barrier height, temperature, injection level, and the ratio of the volume of the well to the volume of the barrier/SCH. Figure 4.4 is an illustration of the capture, escape, and barrier recombination processes that must be included for a proper analysis of a QW laser. From this figure we can write a new set of rate equations that take the 3D carriers into account by adding an additional carrier rate equation for the barrier and SCH region carriers. The sub-threshold laser rate equations then become:

$$\begin{aligned}
\frac{dn_s}{dt} &= \frac{\eta_{inj} I}{qV_s} - \frac{n_s}{\tau_{cap}} - \frac{n_s}{\tau_s} + \frac{n_w}{\tau_{esc}}\frac{V_w}{V_s} \\
\frac{dn_w}{dt} &= \frac{n_s}{\tau_{cap}}\frac{V_s}{V_w} - \frac{n_w}{\tau_w} - \frac{n_w}{\tau_{esc}} \\
\frac{ds}{dt} &= \frac{\beta n_w}{\tau_w} - \frac{s}{\tau_p}
\end{aligned} \tag{4.4}$$

where n_w is the density of carriers in the well, τ_w is their lifetime, V_w is the total volume of the well region, n_s, τ_s and V_s are the density of carriers, their lifetime, and the volume of the barrier/SCH region. Finally τ_{cap} and τ_{esc} are the capture and escape times into and out of the quantum well as shown in figure 4.4. The definitions of all the other terms in equation (4.4) remains the same as described in section 2.1. A small signal analysis of these rate equations yields the theoretical frequency response of the laser.

$$|\Delta s| = \frac{\beta \eta_{inj} \Delta i}{\tau'_w q V_w} \frac{1}{\left| j\omega + \frac{1}{\tau_p} \right|} \frac{1}{\left| \left(j\omega + \frac{1}{T_1} \right)\left(j\omega + \frac{1}{T_2} \right)\tau'_{cap} - \frac{1}{\tau'_{esc}} \right|} \tag{4.5}$$

with $\quad \frac{1}{T_1} = \frac{1}{\tau'_{cap}} + \frac{1}{\tau'_s} \qquad \frac{1}{T_2} = \frac{1}{\tau'_{esc}} + \frac{1}{\tau'_w}$

The differential lifetimes, τ', in (4.5) are defined in the traditional way as the derivatives of the respective recombination, capture, and escape rates with respect to the carrier density. For constant current modulation Δi is not a function of frequency and all frequency dependence is explicitly shown in (4.5). In addition, if $\omega \ll 1/\tau_p$, which is the case for these sub-threshold measurement, we can eliminate the pole due to the photon lifetime, τ_p. From the roots of the denominator we obtain the remaining two poles. However, a numerical analysis of the two roots using typical parameter values for our 1.3 μm InAsP lasers reveal that only one pole, which we call the effective differential carrier lifetime, τ'_{eff}, is found to dominate over the entire frequency and bias current range of the lifetime measurement. It is this lifetime, τ'_{eff}, which we obtain when we fit the measured sub-threshold frequency response to a single pole response function.

$$\frac{1}{\tau'^{\,2}_{eff}} = \frac{A_0 - \sqrt{A_0 - 4A_1}}{2} \tag{4.6}$$

where
$$A_0 = \frac{1}{T_1^2} + \frac{1}{T_2^2} + \frac{2}{\tau'_{cap}\tau'_{esc}}$$

$$A_1 = \frac{1}{T_1^2 T_2^2} - \frac{2}{T_1 T_2 \tau'_{cap}\tau'_{esc}} + \frac{1}{\tau'^{\,2}_{cap}\tau'^{\,2}_{esc}}$$

While we find that only one pole dominates, in accordance with our measurements, the pole is not uniquely determined by the differential lifetime of the carriers in the well. The effective differential lifetime, τ'_{eff}, is a function of the well differential lifetime, τ'_w, the differential well capture, τ'_{cap}, and escape times, τ'_{esc}, and the recombination lifetime of the carriers in the barrier/SCH, τ'_s. To obtain the intrinsic differential carrier lifetime of the well material we can solve the dominant pole expression (4.6) for the differential well lifetime.

$$\tau'_w = \frac{-S_2 - \sqrt{S_2^{\,2} - 4S_1S_3}}{2S_1} \tag{4.7}$$

where
$$S_1 = \frac{1}{\tau_s'^2\tau_{esc}'^{\,2}} - \frac{1}{T_1^{\,2}\tau_{eff}'^{\,2}} - \frac{1}{\tau_{esc}'^{\,2}\tau_{eff}'^{\,2}} - \frac{2}{\tau'_{cap}\tau'_{esc}\tau_{eff}'^{\,2}} + \frac{1}{\tau_{eff}'^{\,4}}$$
$$S_2 = \frac{2}{\tau'_{cap}\tau'_s\tau'_{esc}} + \frac{2}{\tau_s'^2\tau'_{esc}} - \frac{2}{\tau'_{esc}\tau_{eff}'^{\,2}}$$
$$S_3 = \frac{1}{T_1^{\,2}} - \frac{1}{\tau_{eff}'^{\,2}}$$

It is evident from (4.7) that we must know the differential capture and escape times of the carriers as well as the differential carrier lifetime of the barrier/SCH material to extract τ'_w from the measured τ'_{eff}. Numerical analysis of (4.7) reveals that τ'_w is only a weak function of the barrier differential lifetime. Qualitatively this can be explained by realizing that the much lower carrier densities in the barrier/SCH region give rise to a long carrier lifetime and therefore little recombination. Thus the barrier/SCH region acts more like a carrier storage region than a recombination path and the number of carriers there is far more important than their lifetime. Thus accurate determination of the well lifetime is possible without exact knowledge of the barrier recombination coefficients. Furthermore, we show later that the intrinsic well lifetime is mainly a function of the ratio of the differential capture to escape time and not the absolute capture and escape times. This is important since we do not know the absolute capture and escape times but we can obtain an estimate of the ratio of the two from the measured spontaneous emission spectra.

A steady state solution of the carrier rate equations reveals that the ratio of the number of carriers in the barrier/SCH to that in the well, n_s/n_w, is approximately equal to the capture to escape time ratio as given in equation (4.8).

$$\frac{n_s}{n_w} = \tau_{cap}\frac{V_w}{V_s}\left[\frac{1}{\tau_w}+\frac{1}{\tau_{esc}}\right] \approx \frac{\tau_{cap}}{\tau_{esc}}\frac{V_w}{V_s} \tag{4.8}$$

As we will see this approximation is valid for our lasers since τ_w is larger than τ_{esc} and both decrease as the carrier density in the well increases. Since τ_{esc} becomes quite large at low bias levels and/or high barrier heights this approximation will be less accurate, however the correction also becomes small since most of the carriers are in the well and not in the barrier/SCH. The ratio τ_{cap}/τ_{esc} in (4.8) is the DC or steady state ratio of capture to escape time. The ratio required to extract the intrinsic well lifetime is the AC or differential ratio. However, we can make use of previous results that showed that the AC ratio is approximately a factor of two larger than the DC ratio [16]. Therefore if we can find the ratio of the total number of carriers in the barrier/SCH to that in the well we can extract the differential lifetime of the carriers in the well.

The analysis just described requires the ratio of barrier/SCH carriers to well carriers. This ratio is a strong function of laser bias and temperature and therefore must be obtained under the same conditions as the lifetime measurement. We show next that the ratio of well carriers to barrier/SCH carriers can be determined from the measured spontaneous emission spectra. The integrated spontaneous emission intensity is proportional to the density of carriers and the emission spectra provides information on how the carriers are distributed in energy. If we assume the traditional carrier density squared dependence of the integrated spontaneous emission intensity we can write the ratio of the barrier/SCH spontaneous emission to the well emission as:

$$R_t = \frac{V_s B_s n_s^2}{V_w B_w n_w^2} \tag{4.9}$$

where V_s is the total volume of the barrier and SCH regions, B_s and B_w are the quadratic (radiative) recombination coefficients of the barrier/SCH and the well respectively. The carrier densities in the barrier/SCH and well are n_s and n_w respectively. Rearranging (4.8) and combining it with (4.9) yields.

$$\frac{\tau_{cap}}{\tau_{esc}} = \frac{n_s V_s}{n_w V_w} = \sqrt{R_t \frac{V_s B_w}{V_w B_s}} \tag{4.10}$$

Thus by measuring the ratio of barrier/SCH spontaneous emission to well spontaneous emission, R_t, and knowing B_w/B_s we can obtain the ratio of capture to escape times, τ_{cap}/τ_{esc}. While B_s is known to be approximately 1.0×10^{-10} cm^3/s [8], B_w is one of the parameters we are trying to determine. Therefore we must perform our analysis in a self-consistent manner by choosing an initial value for B_w, finding the intrinsic recombination parameters, and then feeding the new B_w back into (4.10) until we converge on a solution.

4.2.2) Spontaneous Emission

The spontaneous emission spectra was collected using the setup shown in figure 4.5. One side of the laser sample was cleaved as close as possible (~80 to 100 μm) to the active region stripe in order to maximize light collection. The laser was then In bonded, p-side up, onto the end of a gold plated brass mount. The side of the laser with the cleave close to the active region was oriented to face off the end of the mount as shown in the expanded view of figure 4.5. As can be seen from the figure, this allowed access not only to the side of the laser but also both facets. The spontaneous emission was collected with a low numerical aperture lens (N.A. = 0.15) from the side of the laser through a ~300μm pinhole in order to remove any light scattered from the facets. The collected light was chopped and focused onto the entrance slit of a 0.5 m single pass grating spectrometer

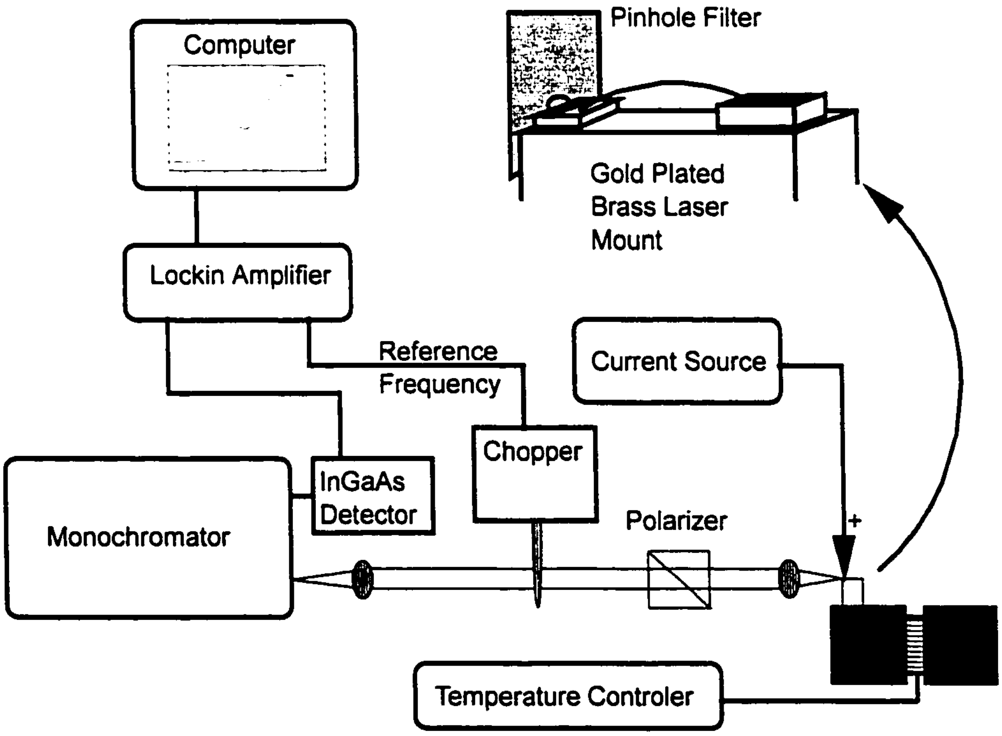

Fig. 4.5 - Experimental setup for measuring the spontaneous emission spectra

equipped with a LN_2 cooled InGaAs detector and lock-in amplifier for signal detection. The input slits of the spectrometer were set at 400 μm while the output slit width was varied from about 200 μm at high bias to 400 μm at low bias in order to maintain maximum dynamic range of the measurement. Both unpolarized and transverse magnetic (TM) polarized spontaneous emission curves were collected using a Calcite prism polarizer thus allowing accurate determination of the heavy hole, light hole, and barrier transition energies. Because of the large spectral window that was covered in these measurements, 4500 Å, all curves were calibrated by measuring the spectral response of a known tungsten-halogen lamp source. Dispersion also made it difficult to properly collect and focus the spontaneous emission across this large spectral range. However, leaving the input slits open at a rather large 400 μm seemed to fix most of this problem.

The solid lines in Fig. 4.6 show typical unpolarized spontaneous emission spectra obtained from our shallow well InAsP MQW lasers at low bias Fig. 4.6(a) and near threshold Fig. 4.6(b). Due to the large overlap of the well heavy hole, light hole, and barrier emission one cannot simply numerically integrate the well and barrier/SCH intensity separately. Therefore we fit the measured spontaneous emission spectra to a spectra calculated by summing over all possible transitions and assuming that the k-selection rule holds. However before we can do this we need to calculate the material, band structure, and band alignment parameters for our laser structure. A sample of the program used to do this is given in appendix A. Material parameters are obtained from Adachi [20] if possible or interpolated from the binary values using Vegard's law. Where possible the temperature dependencies of the material parameters are included. The band alignment and the effects of strain are calculated using the method of Van de

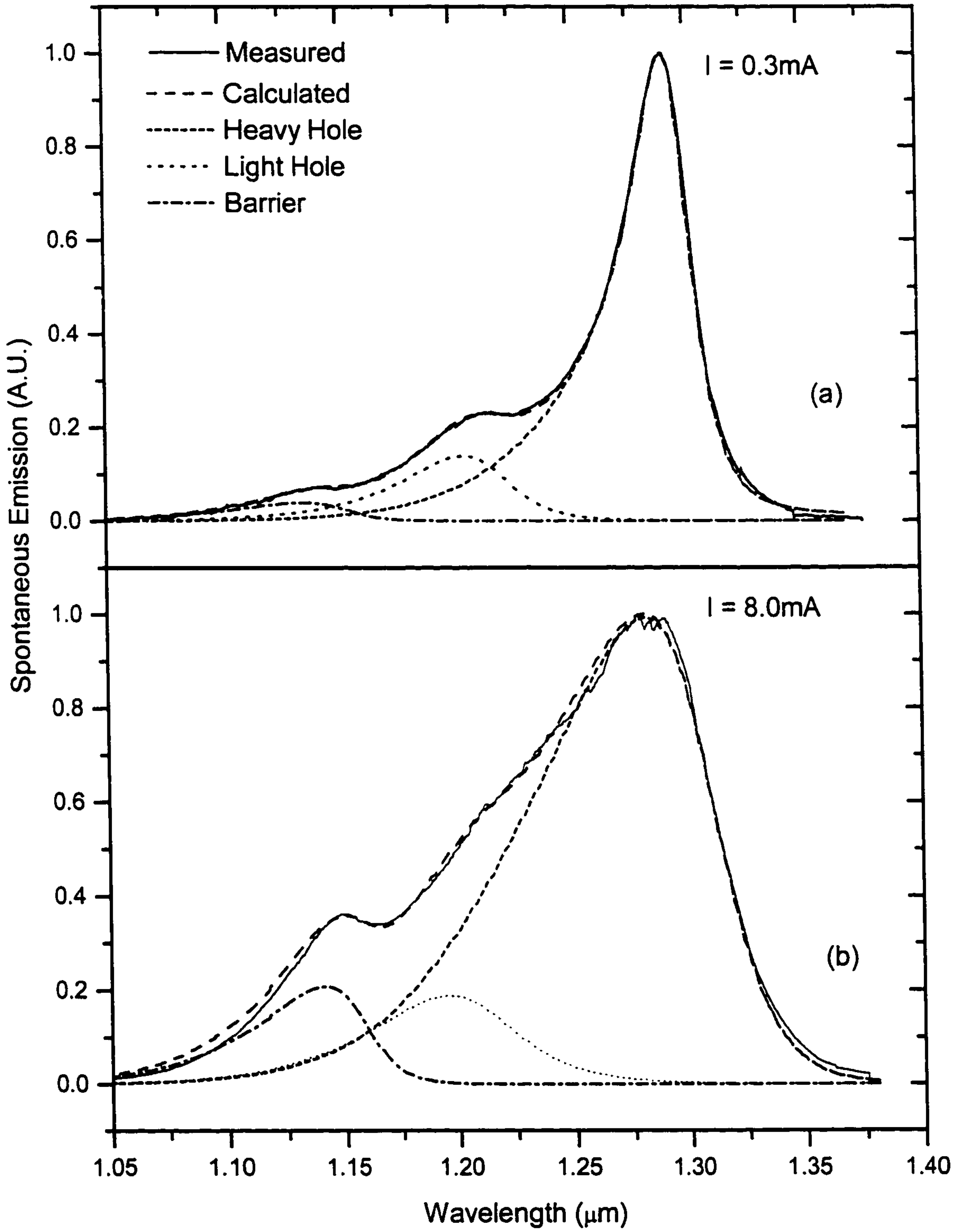

Fig. 4.6 - Spontaneous emission spectra of shallow well laser at T=20°C and (a) low bias (b) near threshold

Walle [17] with slight modifications to the average valence band energies. This was done in order to achieve the generally accepted 40% of the band-gap discontinuity in the conduction band and 60% in the valence band between InP and the quaternary barrier/SCH material. An offset ratio of 65/35 was used between the well and the barrier/SCH as the InAsP is predicted to have more of the band-gap discontinuity in the conduction band [18],[19]. Confinement energies and wave functions were calculated using standard finite barrier QW calculations, with the wave function used only to calculate the spatial overlap between the electron wave function and the various hole wave functions. Finally the refractive index of the layers was calculated using equations from Adachi [20], both for use in the spontaneous emission spectra as well as in calculating the optical confinement factor which will be discussed later.

We can then calculate the spontaneous emission spectra for the QW laser structure obtained from the previous band structure/alignment calculation. In our calculation we found it useful to broaden the density of states function with a hyperbolic secant function to account for alloy and/or well width fluctuations. In addition, we add coulomb enhanced continuum and excitonic effects [21] to the calculation in order to obtain the narrow linewidth seen at low current. We then assume that the total number of electrons is equal to the total number of holes and that the quasi-Fermi levels are flat, i.e. uniform carrier distribution. We use a standard formula for the spontaneous emission rate for both bulk material (barrier/SCH) and the QW active region and assume that the k-selection rule holds. For the QW regions the spontaneous emission rate is of the form [8].

$$R_{sp}^{2D}(E)=\frac{16\pi^2\eta_r q^2 m_r|M_b|^2 P}{m_0^2\varepsilon_0 h^4 c^3 L_w} f_c\left(\frac{m_r}{m_e}(E-E_l)\right) f_v\left(\frac{m_r}{m_h}(E-E_l)\right) E\Phi(E-E_l) \qquad (4.11)$$

where $$|M_b|^2=\frac{m_0^2 E_l(E_l+\Delta)}{6m_c(E_l+\tfrac{2}{3}\Delta)}$$

In this equation Φ is the Heaviside step function, and E_l is the energy separation of the transition of interest, for instance, the first confined electron level to the first heavy or light hole level. The term P is the polarization dependent part of the matrix element, which we assume to be energy independent with the values shown in table 4.1 for both the unpolarized and TM spontaneous emission curves. The meaning of all other parameters is that given in [8]. A similar equation describes the bulk like barrier/SCH states. Adding this bulk term to the QW heavy and light hole bands and then broadening the spectra using a hyperbolic sine line-shape function [22] yields the calculated spontaneous emission spectra. The spontaneous emission at different bias levels can be calculated by changing the Fermi levels and broadening parameters in the

Table 4.1 - Polarization dependence of matrix element for light collected from the side of the laser both with TM polarizer and no polarizer

	Heavy Hole	Light Hole	Barrier
Unpolarized	1/2	5/6	2/3
TM Polarized	0	2/3	1/3

calculation. An example of the Mathcad program used to implement this calculation is given in Appendix B. Clearly there are many model parameters in this calculation, some of which are not known with great accuracy. Fortunately, we only need the appropriate shape of each band in order to find the ratio of integrated barrier/SCH to well emission and this greatly relaxes the calculation requirements.

Fig. 4.6 shows the calculated heavy hole, light hole, and barrier spontaneous emission as well as the sum of these emission bands for comparison to the measured data. Good agreement is achieved at the two bias extremes shown for illustration as well as for all bias levels in between. In the case of low bias, Fig. 4.6(a), the measured and calculated curves are almost indistinguishable from each other, while near threshold, Fig.

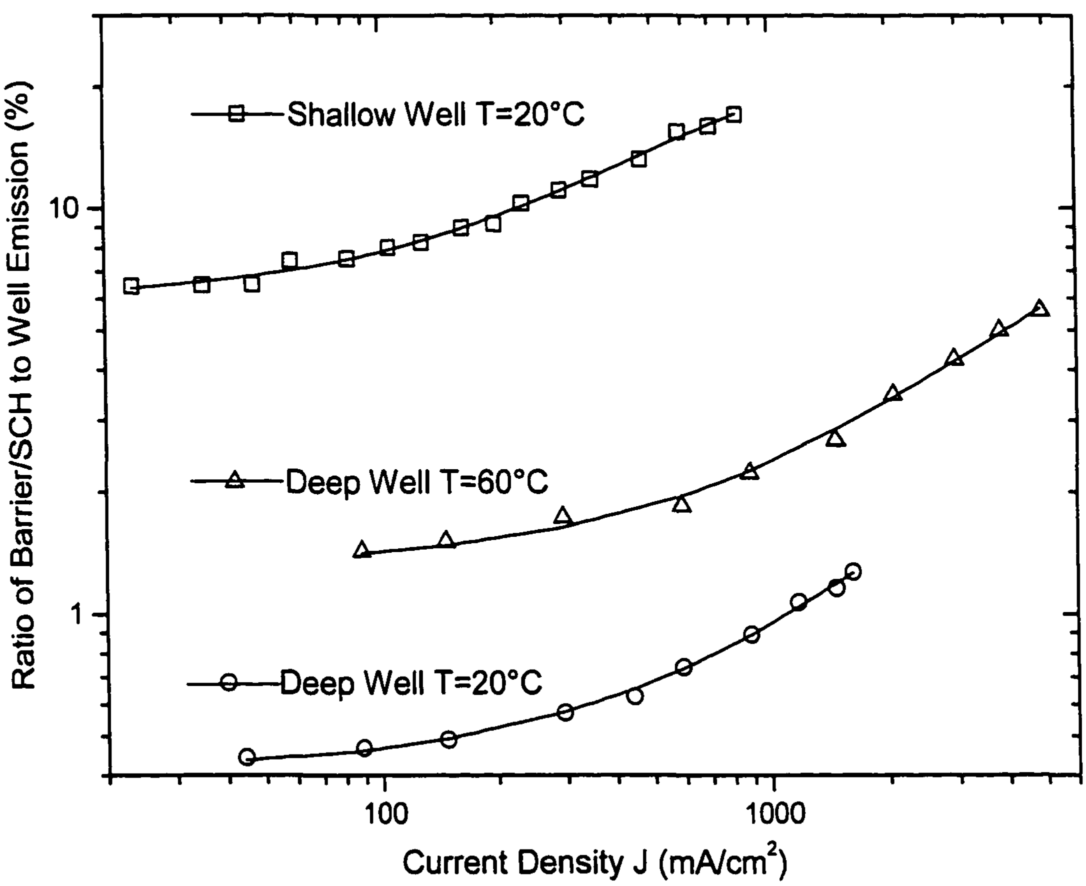

Fig. 4.7 - Ratio of barrier/SCH to well emission for both the shallow well laser at T = 20°C and the deep well laser at T = 20°C and 60°C

4.6(b), the calculated spontaneous emission has slightly increased emission from the high energy tail of the barrier compared to the measured spectra. We have not been able to explain or correct for this effect but it is small and should not add significant error into the determination of R_t. One can easily see from Fig. 4.6 that the amount of emission from the barrier increases significantly with increasing bias current. Figure 4.7 shows the ratio of the integrated barrier/SCH emission to well emission, R_t, for the shallow well laser at 20°C and deep well laser at 20°C and 60°C. We see that, as expected, the shallow well laser has significantly more (~10x) barrier/SCH emission than the deep well laser. In addition the barrier/SCH emission increases both with bias current and temperature.

4.2.3) Intrinsic Recombination Coefficients

With $R_t(I)$ now known we are in a position to determine the intrinsic recombination coefficients from the two carrier level rate equation analysis described in section 4.2.1. Using the generic polynomial relationship between carrier lifetime and the recombination rate:

$$\frac{n}{\tau} = R(n) = An + Bn^2 + Cn^3 \tag{4.12}$$

in the steady state (dn/dt=0) carrier rate equations (4.4), we can obtain the current to carrier density relationship for the QW laser.

$$I = \frac{q}{\eta_{inj}}\left[\, V_w\left(A_w n_w + B_w n_w{}^2 + C_w n_w{}^3\right) + V_s\left(A_s n_s + B_s n_s{}^2 + C_s n_s{}^3\right) \right] \tag{4.13}$$

We can also relate the well differential carrier lifetime to the well carrier density through the standard definition of the lifetime.

$$\frac{1}{\tau_w'} = \frac{dR(n_w)}{n_w} = A_w + 2B_w n_w + 3C_w n_w^{\ 2} \tag{4.14}$$

As in the case of the bulk analysis we can obtain the recombination coefficients from a simultaneous fit of equations (4.13) and (4.14). However, in this case we obtain the intrinsic recombination parameters, A_w, B_w, and C_w. The main difference in our analysis arises from the fact that the intrinsic well lifetime obtained is not the measured lifetime but is calculated from the measured lifetime using the measured ratio of barrier/SCH to well emission and equations (4.7) and (4.10). In order to limit the number of free parameters in our analysis we assume that the nonradiative Shockley-Hall-Read recombination coefficients, A_w and A_s, are more dependent on interface quality than material quality. As such they are inseparable and we set them equal and obtain their value from the fit. The radiative coefficient for the barrier, B_s, is set to 1×10^{-10} cm^3/s as before. The Auger coefficient of the barrier/SCH, C_s, is not well known but we know it should be less than the Auger coefficient of 1.3 μm bulk [3] material since the band-gap is larger. We therefore choose a value of 1×10^{-29} cm^6/s for C_s knowing it will have little effect on the results due to the low carrier densities in the barrier/SCH layers. As mentioned earlier, B_w is one of the parameters we are trying to determine, but it is also used in eqn. (4.10) to calculate the capture to escape ratio, and thus it affects the calculation of the well lifetime from the measured lifetime. We must therefore determine its value in an iterative fashion by making an initial guess at B_w in eqn (4.10), calculating the well lifetime, and obtaining a new value of B_w from the fitting of equations (4.13) and

(4.14). The new value of B_w can be put back into eqn (4.10) and the entire process repeated until we converge on a solution. We found that with a reasonable initial choice for B_w the procedure converged on a solution in just a few iterations.

The intrinsic well differential carrier lifetime versus bias current for the shallow well laser is shown in Fig. 4.8. By comparing the curves in Fig. 4.8 with those obtained using the bulk analysis in figure 4.1, we see that the effective lifetime is longer than the well lifetime by approximately 44% at low bias and by more than a factor a 2.7 at high

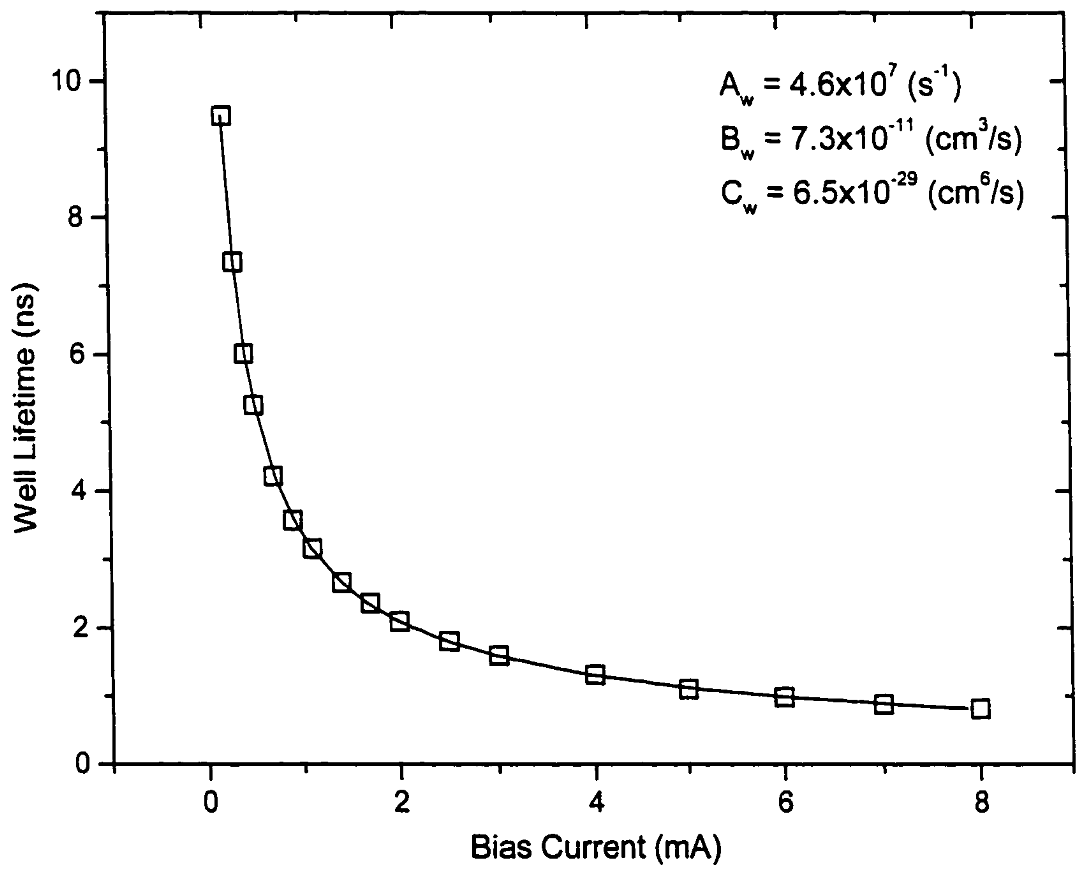

Fig. 4.8 - Intrinsic well lifetime vs. bias current for shallow well laser at 20°C

bias. The fact that the effective lifetime is longer than the intrinsic well lifetime in not surprising since the effective lifetime is a combination of the well lifetime and the longer, due to diluted carrier density, barrier/SCH lifetime. In addition we expect the difference between the effective lifetime and the well lifetime to increase at high bias since the fraction of carrier in the barrier/SCH increases. However, the most important result is the considerable difference in the extracted recombination parameters. The A coefficient is the least affected, it increases by about 30% to 4.5×10^{7} s^{-1}. This value is still fairly low and indicates good quality barrier-well interfaces as well as good material quality in both the well and barrier/SCH layers. The B coefficient increases roughly 60% to a more reasonable 7.2×10^{-11} cm^3/s while the C coefficient increases almost 2 orders of magnitude to 5.1×10^{-29} cm^6/s. Again the trends in the coefficients are as expected since the largest changes are in the coefficients most sensitive to carrier density, i.e. C.

We also obtained the intrinsic recombination parameters for the deep well laser from the well lifetime versus bias current shown in figure 4.9. In contrast to the shallow well BH laser, the effective lifetime, figure 4.2(b), while still longer than the well lifetime, is only longer by ~20% at low bias and ~50% at high bias. This is as expected since the deep well will have more of the carriers in the well the measured effective lifetime should be much closer to the intrinsic well lifetime. The fitting of the lifetime data of figure 4.9 was accomplished using the more complicated QW laser rate equation analysis described earlier in this section. This was combined with the procedure described in the bulk analysis of the deep well laser, where we obtained A_w and B_w from the BA data, fig. 4.9(a), and C_w from the BH data, fig. 4.9(b). Again the fits are very good to both sets of data using only one set of recombination parameters. For the deep

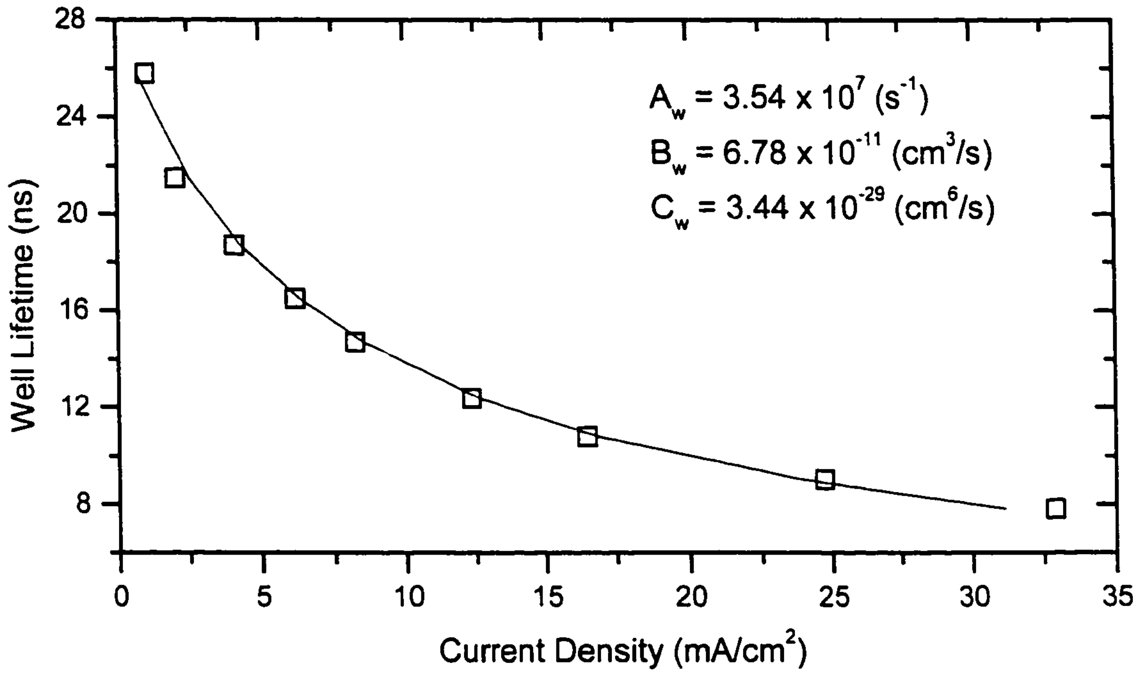

Fig. 4.9(a) - Lifetime vs. bias current of deep well BA laser at T=20°C

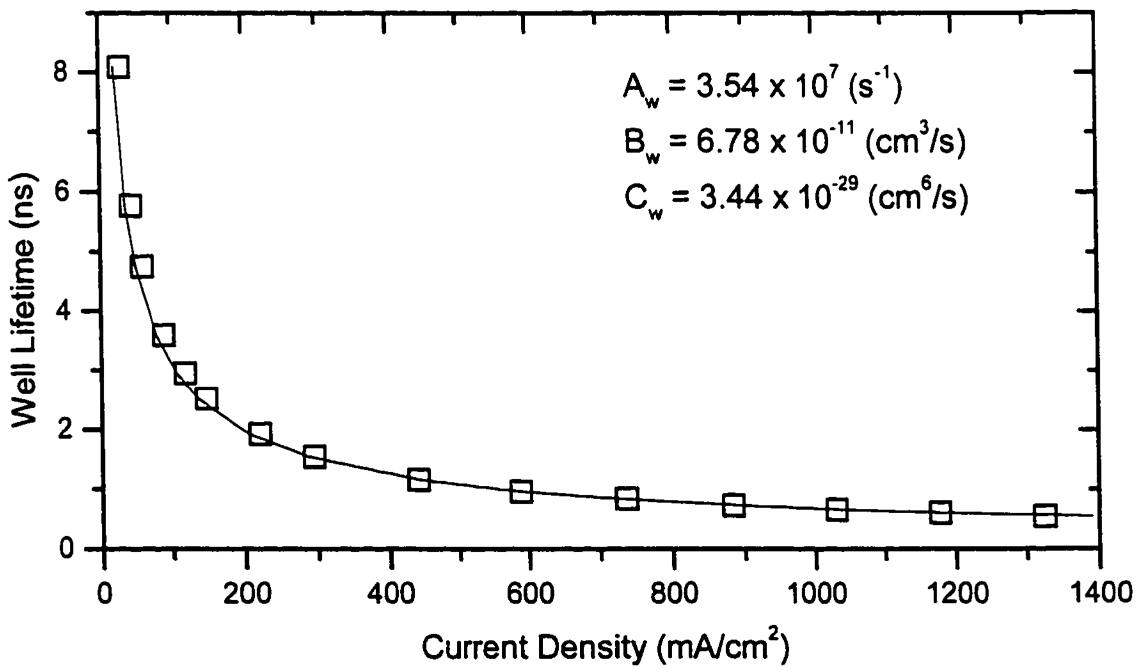

Fig. 4.9(b) - Lifetime vs. bias current of deep well BH laser at T=20°C

well laser the A coefficient was nearly unchanged from the bulk analysis at 3.54×10^{7} s^{-1} while the B coefficient increased ~38% to 6.78×10^{-11} cm^3/s. As in the case of the shallow well laser the largest increase was in the C coefficient, which increased by a factor of ~2.4 to 3.44×10^{-29} cm^6/s. So while the intrinsic recombination coefficients of the deep well laser increase from their effective values, the increases are smaller than in the shallow well laser, as expected. This also shows that even our deep well laser is not deep enough to yield intrinsic recombination parameters directly from the bulk rate equation analysis. Table 4.2 summarizes the comparison of the two different analysis techniques

Table 4.2 – Shallow and Deep well comparison of extracted recombination coefficients using both the bulk and QW analysis

	Shallow Well		Deep Well	
Analysis	Bulk	QW	Bulk	QW
A x 10^{-7}	3.3	4.5	3.5	3.5
B x 10^{11}	3.1	7.2	4.9	6.8
C x 10^{29}	.058	5.1	1.0	3.4

on the carrier lifetime data of the shallow and deep well laser. From this table it is clear that, while the bulk analysis yields very different recombination coefficients for the shallow and deep well laser, the coefficients obtained from the QW analysis are in excellent agreement. This indicates that the effect of the barrier/SCH carrier population has been properly removed thus yielding intrinsic well recombination parameters.

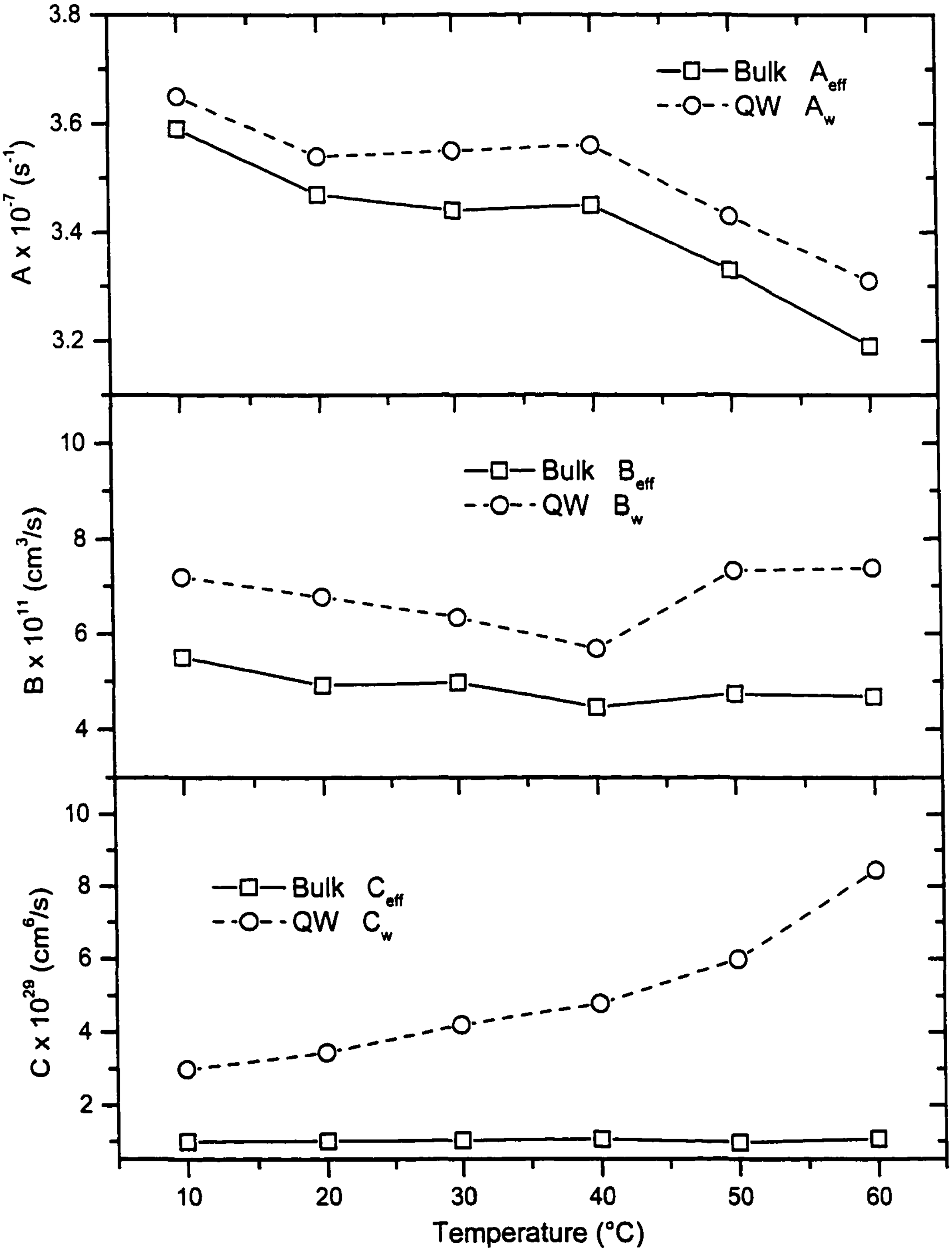

Fig. 4.10 - Temperature dependence of intrinsic recombination coefficients of InAsP/InP deep well laser

4.2.4) Temperature Dependence of Intrinsic Coefficients

As discussed in section 4.1.3 the temperature dependence of the recombination coefficients extracted using the bulk analysis, both in this work and in others, was unusual. In particular the Auger or C coefficient, which indicated either a flat, or negative temperature dependence, was in contradiction with theory. However, as can be seen from figure 4.10, if one uses the new QW analysis to obtain the recombination coefficients, a much different result is realized. In this figure, we see that the temperature dependence of the A_w and B_w coefficients is very similar to the bulk analysis even though their intrinsic values increase slightly at all temperatures. The C coefficient however, goes from being basically constant with temperature in the bulk analysis, to increasing quite significantly in the new QW analysis. The QW analysis thus provides a much more realistic temperature dependence and again validates the usefulness of this new analysis in understanding QW laser materials. Our results show that considerable underestimation of the C coefficient can result if the barrier/SCH population is not taken into account. This is particularly true at higher temperatures or in QW lasers with a shallow well.

We now turn our attention to the recombination currents flowing in our QW lasers. Figure 4.11 shows the fraction of the recombination current that is due to defect, radiative, and Auger in our deep well laser versus the total recombination current at the two temperature extremes studied. We see that even at 10°C, the Auger current is quite high at threshold accounting for nearly 60% of the current, while at 60°C Auger comprises nearly 80% of the current. We also see that the increasing Auger current squeezes out the radiative current leaving only a very small region were radiative

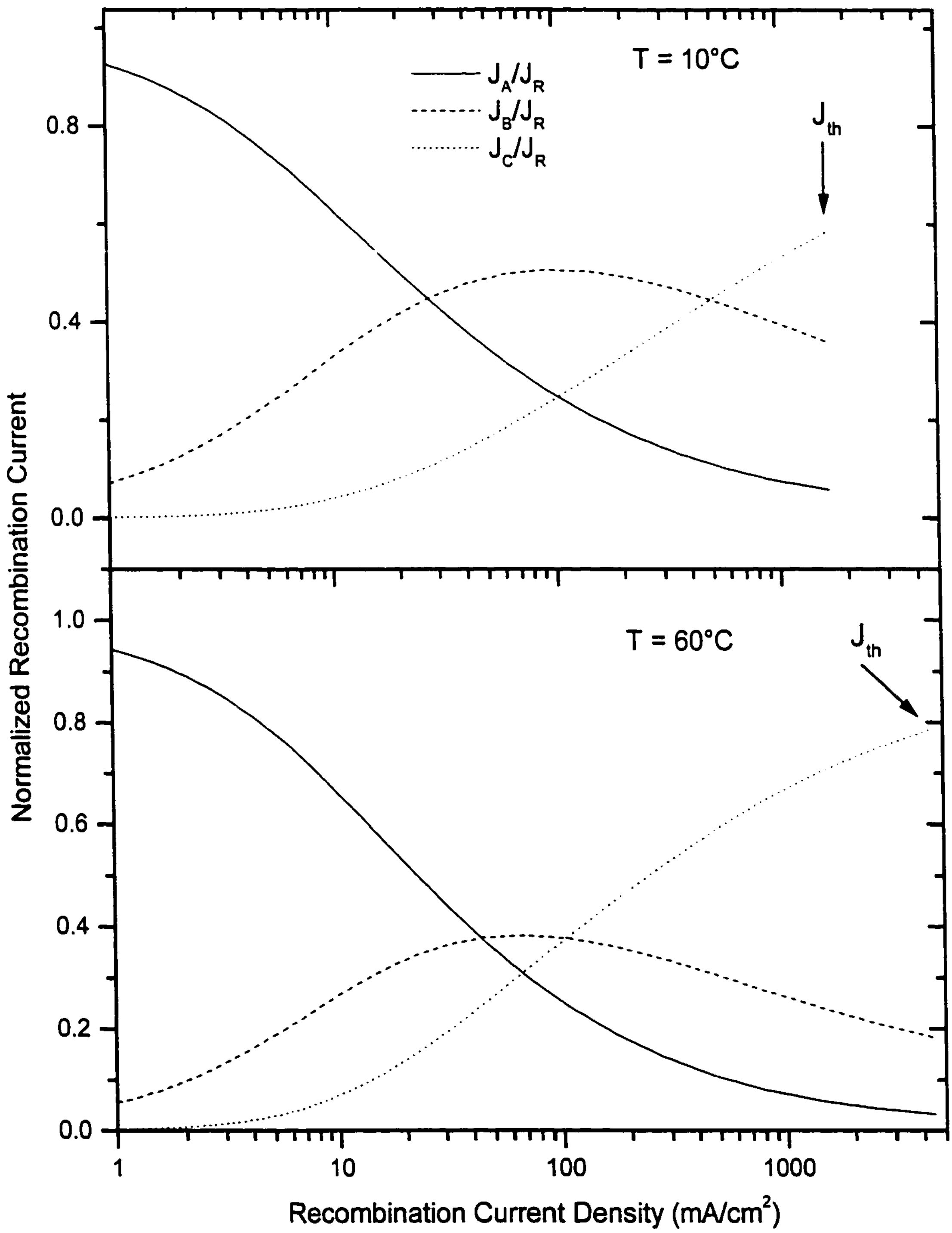

Fig. 4.11 - Fraction of current due to defect (J_A), Radiative (J_B), and Auger (J_C) in our deep well laser at 10°C and 60°C

dominates at 60°C. This may partially account for the unusual rise in the B coefficient seen at 50°C and 60°C as these data points are less sensitive to the radiative coefficient. The importance of using lifetime data from both BA and BH lasers is clearly evident from the figure. Here we see that if we had only used the BH data that goes down to ~30 mA/cm^2, there would have been no region where the defect recombination would dominate. This would have significantly increased the uncertainty of this coefficient and therefore increased the error of the other coefficients as well.

4.2.5) Analysis Sensitivity

We are now in a position to investigate some of the assumptions made earlier in the analysis and determine the sensitivity of our method to some of the parameters that we had to estimate. In section 4.2.1 we stated that the differential well lifetime was mainly a function of the ratio of the capture to escape time and not very sensitive to the absolute values of these times. Table 4.3 shows the intrinsic recombination parameters obtained from the analysis of the shallow well laser lifetime data using capture times ranging from 0.1 ps to 100 ps. In each case the escape times were allowed to vary with bias according to the measured bias dependence of R_t in (4.10). Table 4.3 shows that even with capture times covering three orders of magnitude the change in the intrinsic recombination coefficients is less than 15% illustrating the insensitivity of our technique to the absolute value of the capture and escape times.

Table 4.3 - Extracted well recombination parameters versus capture time for shallow well laser at T=20°C

τ_{cap}	0.1 ps	1.0 ps	10 ps	100 ps
A_w x 10^{-7}	4.47	4.47	4.49	4.70
B_w x 10^{11}	7.19	7.19	7.09	6.23
C_w x 10^{29}	5.05	5.06	5.02	4.76

We also investigated the sensitivity of our analysis to the barrier/SCH recombination parameters fixed in section 4.2.3 to reduce the number of fitting parameters. Table 4.4 shows the intrinsic recombination parameters obtained from the shallow well laser analysis using various values for the barrier/SCH recombination coefficients B_s and C_s. Note that as described previously, A_s is not varied since its value was not fixed in (10b) but was determined from the fitting procedure. From table 4.4 we see that varying C_s from $2.0\text{x}10^{-30}$ cm^6/s to $5.0\text{x}10^{-29}$ cm^6/s resulted in no more than 9% variation in the extracted intrinsic recombination parameters.

Table 4.4 - Extracted well recombination parameters versus barrier/SCH coefficients for shallow well laser at T=20°C

	C_s x 10^{29}			B_s x 10^{10}		
	0.2	1.0	5.0	0.8	1.0	1.2
A_w x 10^{-7}	4.49	4.47	4.36	4.67	4.47	4.31
B_w x 10^{11}	7.09	7.19	7.75	7.37	7.19	6.98
C_w x 10^{29}	5.03	5.06	5.23	6.80	5.06	3.95

The parameter to which our method is most sensitive is B_s. This is not surprising since B_s not only contributes to the current in (4.14) but is also important in determining the capture to escape ratio in (4.10) and thus the ratio of barrier/SCH carriers to well carriers. Fortunately the bulk radiative recombination coefficient is also a parameter that varies little with material composition and quality and therefore we know it more accurately than C_s or τ_{cap}. The typical number for B_s in InGaAsP alloys is $1.0\text{x}10^{-10}$ cm^3/s and we therefore vary B_s from $0.8\text{x}10^{-10}$ cm^3/s to $1.2\text{x}10^{-10}$ cm^3/s. From table 4.4 it is clear that this resulted in little change for the fitted A_w (~8%) and B_w (~5%) coefficients. The C_w coefficient however varied from $3.95\text{x}10^{-29}$ cm^6/s to $6.80\text{x}10^{-29}$ cm^6/s, an increase of about 70%. While this is a fairly large range, it is quite small compared to the approximately two orders of magnitude difference in C_w obtained between the bulk and the QW rate equation analysis for these lasers. It is clear from this procedure that our analysis is reasonably insensitive to the parameters which we have had to estimate and as such should produce relatively accurate intrinsic recombination coefficients.

References For Chapter IV

[1] R. Olshansky, C. B. Su, J. Manning, and W. Powazinik, "Measurement of Raditive and Nonradiative Recombination Rates in InGaAsP and AlGaAs Light Sources," IEEE J. Quantum Electron., Vol., QE-20, No. 8, pp. 838-854, 1984

[2] R. Olshansky, J. LaCourse, T. Chow, and W. Powazinik, "Measurement of radiative, Auger, and nonradiative Currents in 1.3-μm InGaAsP Buried Heterostructure Lasers," Appl. Phys. Lett., Vol. 50, No. 6, pp. 310-312, 1987

[3] G. E. Shtengel, D. A. Ackerman, P. A. Morton, E. J. Flynn, and M. S. Hybertsen, "Impedance-corrected carrier lifetime measurements in semiconductor lasers," Appl. Phys. Lett., Vol. 67, No. 11, pp. 1506-1508, 1995.

[4] Y. Zou, J. S. Osinski, P. Grodzinski, P. D. Dapkus, W. C. Rideout, W. F. Sharfin, J. Schlafer, and F. D. Crawford, "Experimental Study of Auger Recombination, Gain, and Temperature Sensitivity of 1.5μm Compressively Strained Semiconductor Lasers," IEEE J. Quantum Electron., Vol. **29**, No. 6, pp. 1565-1575, 1993

[5] D. A. Ackerman, P. A. Morton, G. E. Shtengel, M. S. Hybertsen, R. F. Kazarinov, T. Tanbun-Ek, and R. A. Logan, "Analysis of T_0 in 1.3 μm Multi-Quantum-Well and Bulk Active Lasers," Appl. Phys. Lett., Vol. 66, No. 20, pp. 2613-2615, 1995

[6] D. A. Ackerman, G. E. Shtengel, M. S. Hybertsen, P. A. Morton, R. F. Kazarinov, T. Tanbun-Ek, and R. A. Logan, "Analysis of Gain in Determining T_0 in 1.3 μm Semiconductor Lasers," IEEE J. Selected Topics Quantum Electron., Vol., 1, No. 2, pp. 250-263, 1995

[7] A. A. Bernussi, J. Pikal, H. Temkin, D. L. Coblentz, and R. A. Logan, "Rate Equation Model of High-Temperature Performance of InGaAsP Quantum Well Lasers," Appl. Phys. Lett., Vol. 66, No. 26, pp. 3606-3608, 1995

[8] G. P. Agrawal and N. K. Dutta, "*Semiconductor Lasers*," 2nd ed., Van Nostrand Reinhold, New York, NY, 1993

[9] A. R. Adams, "Band Structure Engineering for Low-Threshold High Efficiency Semiconductor Lasers," Electron. Lett., Vol. 22, pp. 249-250, 1986

[10] E. Yablonovitch and E. O. Kane, "Reduction of Lasing Threshold Current Density by the Lowering of the Valence Band Effective Mass," J. Lightwave Technol., Vol. 4, pp. 504-506, 1986

[11] E. P. O'Reilly and A. R. Adams, "Band Structure Engineering in Strained Semiconductor Lasers," IEEE J. Quantum Electron., Vol., QE-30, pp. 366-379, 1994

[12] Y. C. Chen, P. Wang, J. J. Coleman, D. Bour, K. K. Lee, and R. G. Waters, "Carrier Recombination Rates in Strained-Layer InGaAs-GaAs Quantum Wells," IEEE J. Quantum Electron., Vol. 27, No. 6, pp. 1451-1454, 1991

[13] A. P. Ongstad, D. J. Gallant, and G. C. Dente, "Carrier Lifetime Saturation in InGaAs Single Quantum Wells," Appl. Phys. Lett., Vol. 66, No. 20, pp. 2730-2732, 1995

[14] T. Yamamoto, T. Odagawa, K. Tanaka, and S. Ogita, "Influence of Separate Confinement Heterostructures on the Effective Carrier Recombination Coefficient in Quantum Well Laser Structures," Appl. Phys. Lett., Vol. 71, No. 11, pp. 1543-1545, 1997

[15] G. Fuchs, C. Schiedel, A. Hangleiter, V. Harle, and F. Scholz, "Auger Recombination in Strained and Unstrained InGaAs/InGaAsP Multiple Quantum-Well Lasers," Appl. Phys. Lett., Vol. 62, No. 4, pp. 396-398, 1993

[16] Chin-Yi Tsai, Chin-Yo Tsai, Yu-Hwa Lo, and L. F. Eastman, "Carrier DC and AC Capture and Escape Times in Quantum-Well Lasers," IEEE Photon. Technol. Lett., Vol. 7, No. 6, pp. 599-601, 1995

[17] C. G. Van de Walle, "Band Lineups and Deformation Potentials in the Model-Solid Theory," Physical Review B, Vol. 39, No. 3, pp. 1871-1883, 1989

[18] R. P. Schneider, JR. And B. W. Wessels, "Photoluminescence Excitation Spectroscopy of $InAs_{0.67}P_{0.33}$/InP Strained Single Quantum Wells," J. Electron. Mater., Vol. 20, No. 12, pp. 1117-1123, 1991.

[19] M. Yamamoto, N. Yamamoto, and J. Nakano, "MOVPE Growth of Strained InAsP/InGaAsP Quantum-Well Structures for Low-Threshold 1.3-μm Lasers," IEEE J. Quantum Electon., Vol. 30, No. 2, pp. 554-560, 1994

[20] S. Adachi, "*Physical Properties of III-V Semiconductor Compounds*," John Wiley and Sons, Ney York, 1992

[21] N. Peyghambarian, S. W. Koch, and A. Mysyrowicz, "*Introduction to Semiconductor Optics*," Prentice Hall, Englewood Cliffs NJ, 1993

[22] W. W. Chow, S. W. Koch, and M. Sargent III, "*Semiconductor-Laser Physics*," Springer-Verlag, Berlin, 1994

Chapter V

Temperature Dependence of Laser Performance

As discussed throughout this thesis one of the most critical problems in long wavelength semiconductor lasers is the rapid change of lasing characteristics, mainly threshold current and slope efficiency, with temperature. While many studies have been conducted on this subject no clear consensus has yet been achieved [1]-[8]. One explanation for the differing opinions could be incorrect measurement of carrier lifetime, due to neglecting the laser impedance [9],[10], along with incorrect determination of recombination coefficients from the lifetime changes with bias, due to ignoring the barrier/SCH carrier populations [11]-[13]. We showed, in section 3.1, the error in the carrier lifetime that is realized when we do not account for changing laser impedance with bias and frequency. In chapter 4, we demonstrated the large error in determining the recombination coefficients that occurs when the barrier/SCH carrier population was ignored. Both of these effects lead directly to incorrect determination of the recombination coefficients in QW lasers and thus incorrect evaluation of the temperature dependence. Up until this point we have been laying the foundation for a proper study of the root cause of this problem by developing new methods for determining carrier lifetime and the recombination coefficients in QW lasers. With these new methods in hand, we can now turn our attention to the larger problem of the temperature dependence of long wavelength lasers.

As we saw in chapter 4, the Auger coefficient C of the shallow well laser changed by more than two orders of magnitude at 20°C when the barrier/SCH carriers were taken into account. Since the correction was already very large, and would only get larger at higher temperatures, we decided to do the temperature study using the deep well lasers. This was in spite of the fact that the deep well lasers had very bad yield and poorer lasing characteristics than the shallow well laser. It was felt that the larger the correction the more error in the determination of the recombination coefficients, and therefore the deep well laser, with its much lower barrier/SCH carrier population, was a better choice for this analysis.

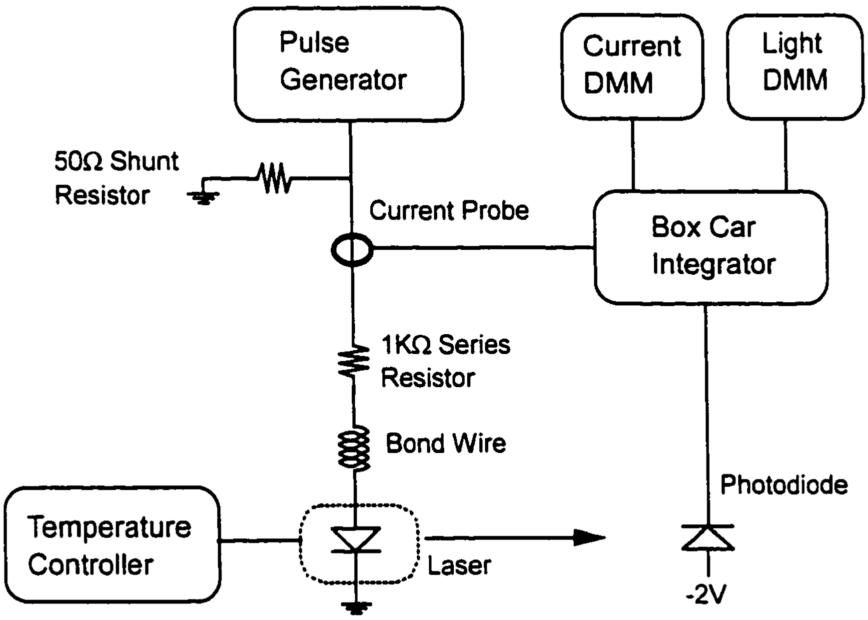

Fig 5.1 - Experimental setup of pulsed light-current measurement

5.1) Threshold Current and Efficiency

Before we can evaluate the cause of the temperature dependence of the threshold current and efficiency we must first measure these laser parameters on the lasers of interest. Both of these parameters can be determined from the light versus current (LI) measurements using the setup shown in figure 5.1. Because these lasers have fairly large threshold currents at high temperature, we must measure the LI relationship using a pulsed drive current. If we use a short pulse with a low duty cycle we can minimize resistive heating of the active region from the current being injected into the laser and keep the active region temperature near the substrate temperature. In our experiments we found that active region heating started to occur on a time scale of about 125 ns. We therefore kept our pulses below 125 ns and used a repetition rate of 10 KHz for a duty

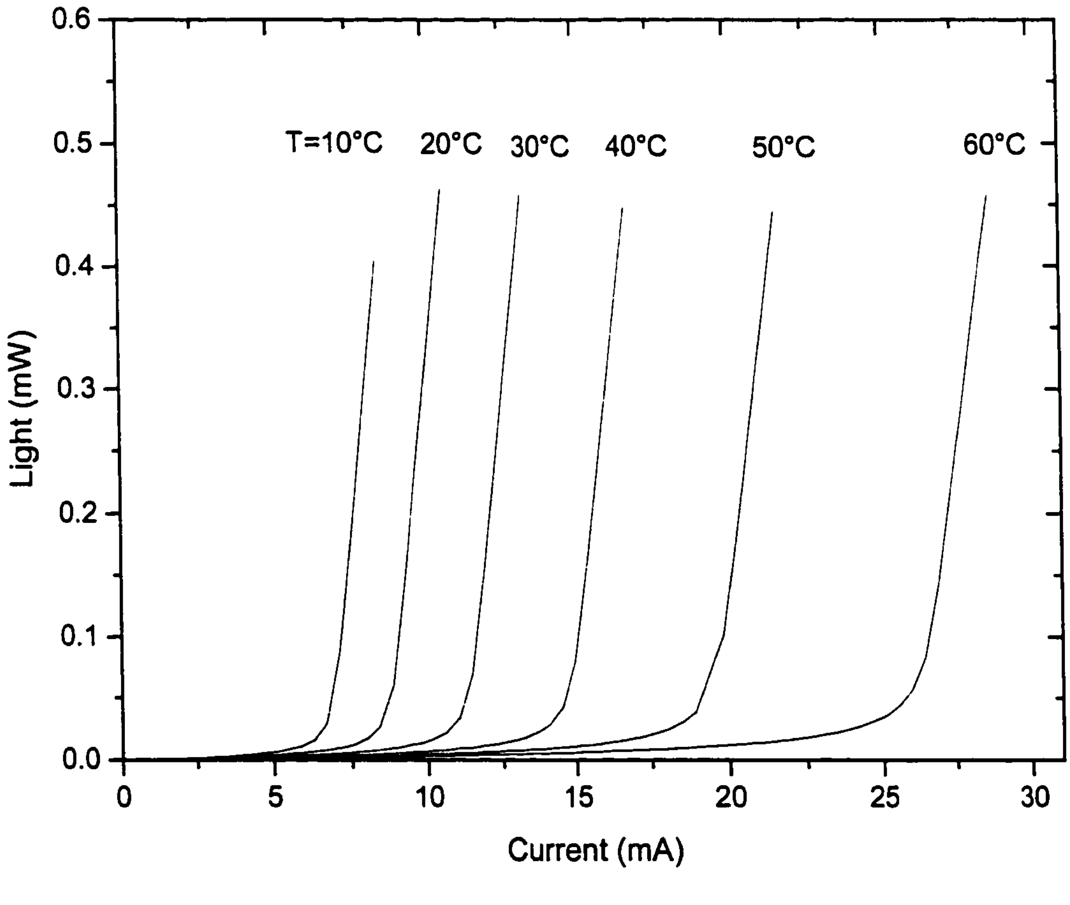

Fig. 5.2 - Light current curves for 500μm deep well InAsP laser

cycle of ~0.1%. The 1 kΩ series resistor in the setup serves to provide a constant impedance and thus a constant current pulse from the voltage pulse generator. The pulse current is obtained from a current probe and then both the light and current signal are fed to a gated box car integrator with a 40 ns gate placed in the middle of each respective signal pulse. The gated integrator first integrates during the gate and then averages a number of pulses, 1000 in our case, yielding a DC signal proportional to the current and light pulse which is fed to a pair of digital multimeters and read by a computer.

The light current curves for a ~500 μm long deep well laser at temperatures from 10°C to 60°C are shown in figure 5.2. The threshold current is obtained by extrapolating the above threshold linear region back to the current at which the light is zero. The external efficiency, η_d, is related to the slope of the light current curve above threshold through [14]:

$$\eta_d = \frac{2q\lambda}{hc}\frac{dL}{dI} \tag{5.1}$$

where q is the electronic charge, h is Planks constant, c is the speed of light, and λ is the wavelength of light. From figure 5.2 we see that the threshold current increases dramatically with increasing temperature and the slope efficiency decreases slightly. With these effects combined the amount of current needed to generate a fixed amount of light, e.g. 0.2 mW, changes from ~7 mA at 10°C to ~27 mA at 60°C. This very large drive current change is what makes it so difficult to design a system using these lasers without temperature control.

The most common figure of merit for the temperature performance of a laser is the characteristic temperature, T_0 [14],[15]. T_0 is obtained by fitting the measured rise in threshold current to the exponential equation (5.2), where we see that a low T_0 corresponds to high temperature sensitivity.

$$I_{th} = I_0 \exp\left(\frac{T}{T_0}\right) \tag{5.2}$$

Fig 5.3 shows the measured increase in threshold current on a log scale of four different length deep well InAsP lasers along with the fit to equation (5.2) and their extracted T_0. From this figure we see that T_0 decreases slightly as the lasers are made shorter. This is because shorter lasers have higher mirror losses leading to higher total losses and thus

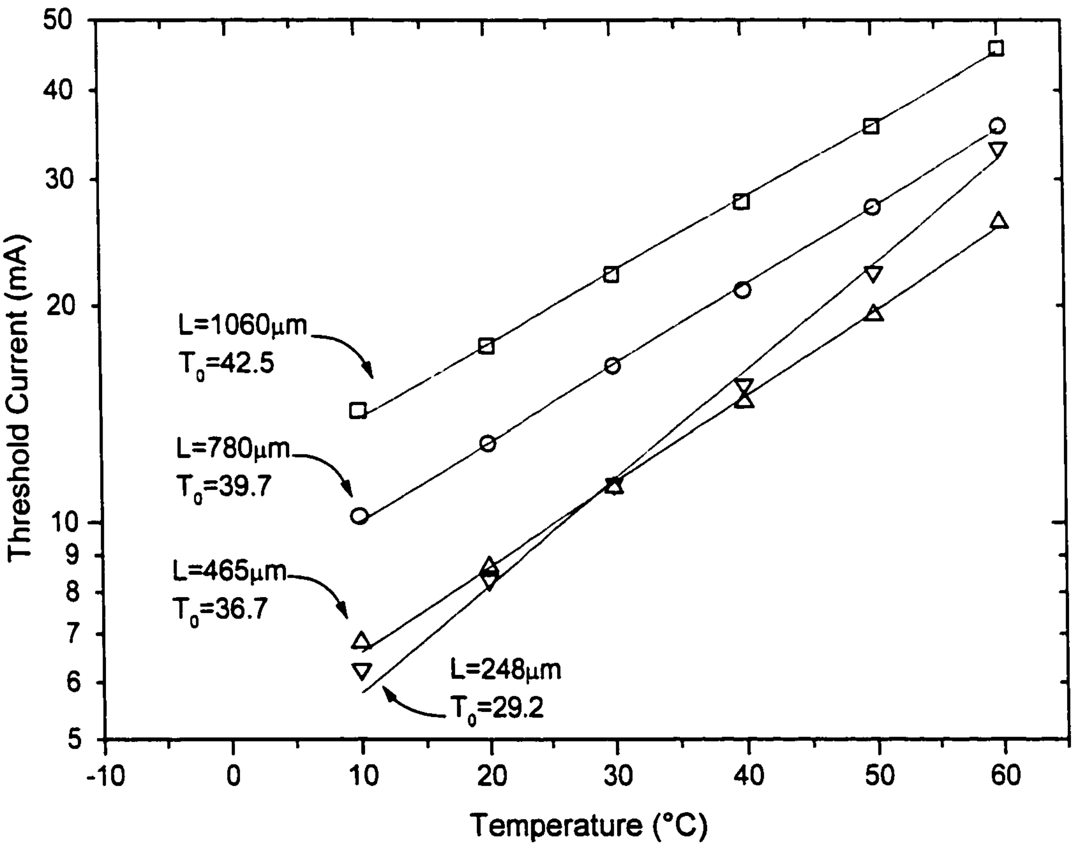

Fig. 5.3 - Temperature dependence of threshold current for four different length InAsP deep well lasers along with exponential fit and T_0

require more gain to lase. More gain means higher carrier densities and Fermi levels and as we have already discussed Auger is very sensitive to carrier density and carrier overflow of the QWs is sensitive to Fermi levels and thus the lower T_0. We also see some interesting behavior from the 248 μm long laser in that the T_0 of this laser decreases so dramatically from that of the 465 μm laser that their curves cross and as such it has a larger threshold current than the longer laser above 30°C. Another interesting feature of this laser is that the threshold trend is also slightly stronger than exponential. It is possible that an additional process has either become important, or possibly even dominant, at the carrier density and Fermi levels present in the 248 μm laser.

The external efficiency of the lasers is also a very important parameter. From the efficiency versus laser length we can determine the internal loss, α_i, and internal efficiency, η_i. This is done through the relationship [14],[16]:

$$\frac{1}{\eta_d} = \eta_i \left(1 + \frac{\alpha_i L}{\ln\left(\frac{1}{R_m} \right)} \right) \tag{5.3}$$

where L is the cavity length and R_m is the mirror reflectivity. If the measurements are done as a function of temperature we can also determine the temperature dependence of these parameters. Fig 5.4 shows the inverse efficiency versus cavity length, for all but the 248m laser, along with a fit to (5.3). We exclude the data from the short laser because we do not want the unusual characteristics of this laser to skew the results. We found that gave better results than including the short laser even though this left only three data points at each temperature. Table 5.1 shows the fitted internal efficiency and internal loss obtained from figure 5.4. From this table we see that η_i decreases with

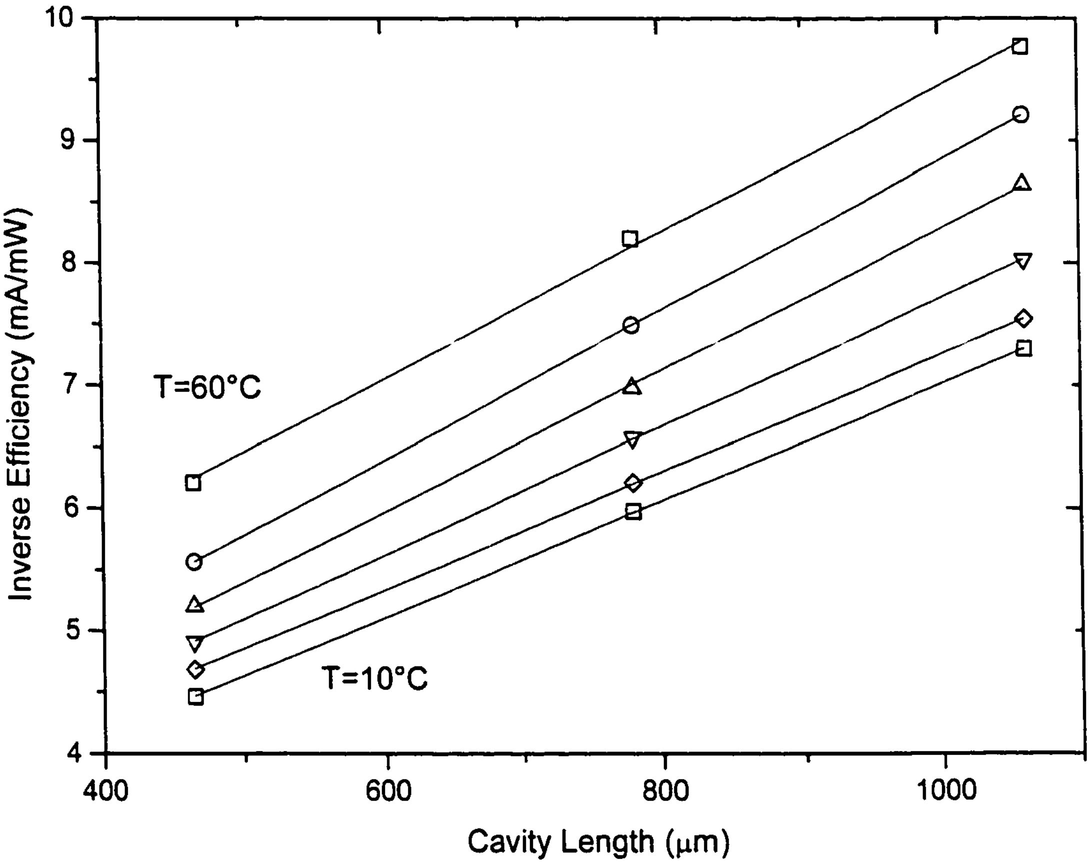

Fig 5.4 - Inverse efficiency versus cavity length for the deep well InAsP lasers

temperature, slowly from 10°C to 40°C and much more steeply above 40°C. This trend is expected since the largest factor in η_i is carrier leakage over the heterobarrier, either across the junction or around the active region, which should increase with temperature. The internal loss α_i, however, shows no clear trend with temperature as it fluctuates between ~25 and ~30 cm^{-1} until it drops to 22 cm^{-1} at 60°C. Usually α_i increases slightly with temperature and carrier density and it is possible that the small number of data

Table 5.1 – Temperature dependence of internal efficiency and loss in deep well InAsP laser

Temperature	η_i	α_i
10	.934	27.2
20	.856	25.1
30	.848	27.1
40	.839	29.6
50	.775	29.0
60	.607	22.2

points is affecting the fit parameters. We can also get an estimate of α_i from the gain data and we will revisit this issue later in section 5.3 when we look at gain curves from these lasers.

5.2) Temperature Calibration

Clearly temperature is a very important measurement parameter that must be controlled during our experiments. While all of our measurements utilize a Thermo-Electric-Cooler (TEC) to control substrate temperature, what we really want is to control active region temperature. For the LI measurements of section 5.1 this was accomplished by using a short, low duty cycle, pulse drive current which did not allow time for resistive heating to occur. However many of our measurements cannot be conducted with pulse drive since they require long measurement times. In the case of the lifetime measurements the spectrum analyzer can be used in a gated fashion but the bandwidth of the measurement would be limited by the gate width, significantly increasing the noise floor. The gain measurements which we will discuss in the next section also require very low noise floor and we therefore use a LN_2 cooled InGaAs detector with very high

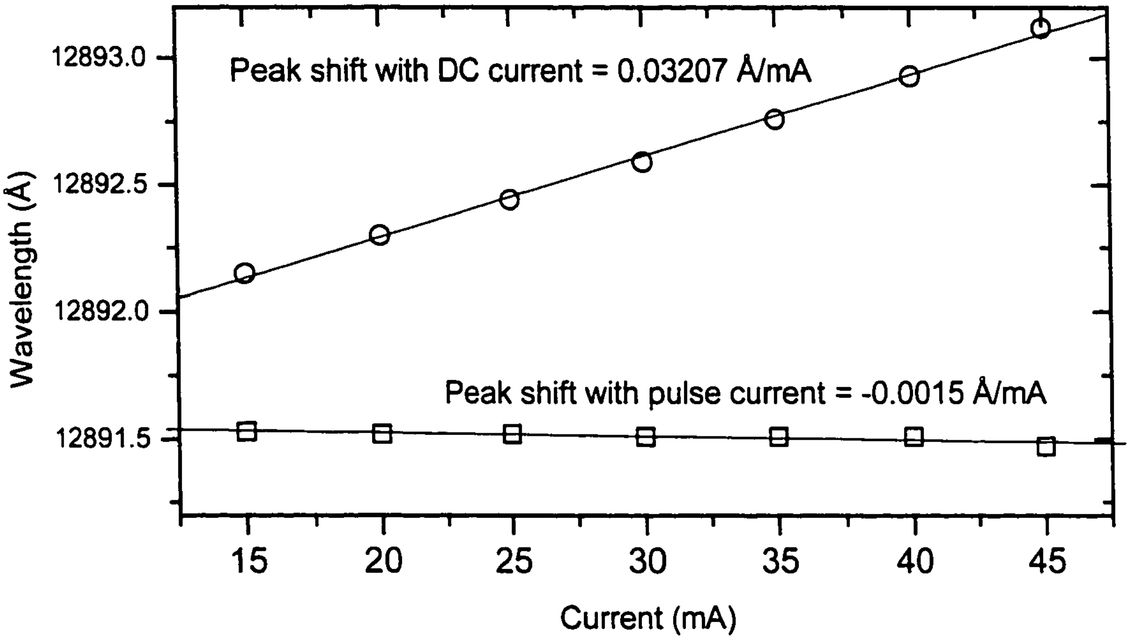

Fig 5.5 - Wavelength shift of Fabry-Perot mode with DC current

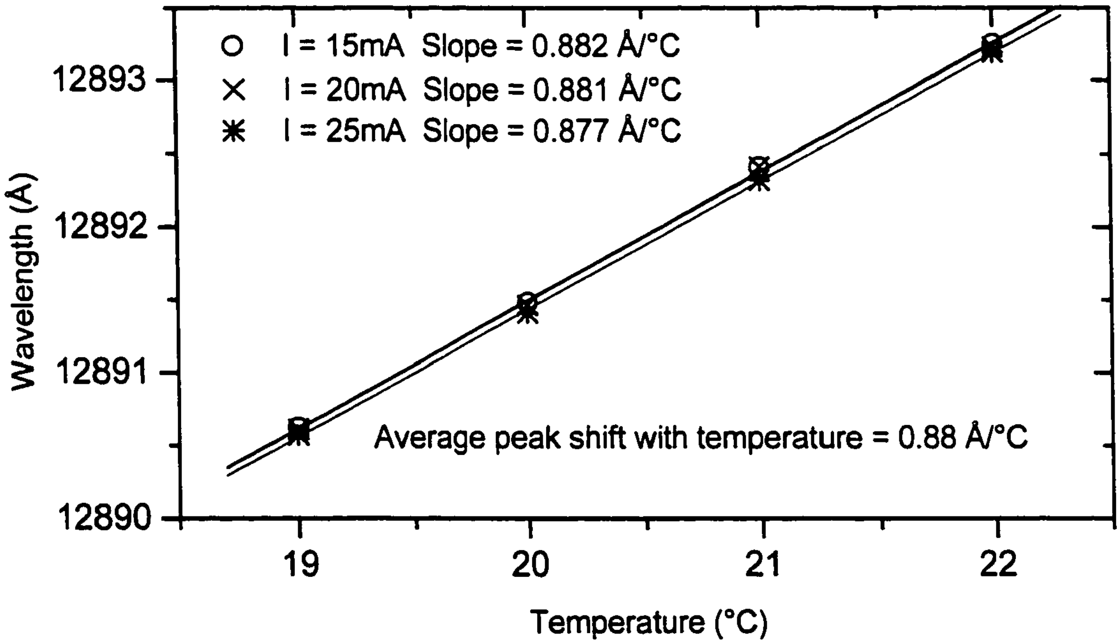

Fig 5.6 - Wavelength shift of Fabry-Perot mode with temperature

transimpedance gain (10^{10}). Thus it is not possible to achieve the noise floor necessary using only a 125ns pulse. Therefore we measure the amount of active region heating that occurs with a given drive current and then adjust the substrate temperature to compensate for any resistive heating.

Figure 5.5 shows the shift of a single Fabry-Perot cavity mode emission peak with injected current. The open circles are the measured shift when injecting a DC current shown along with the linear fit giving a rate of 0.03207 Å/mA. This shift is mostly due to resistive heating, however, since carrier density is not completely pinned above threshold the peak position does shift slightly due to increased carrier density. Therefore we repeat the same measurement using pulsed current to obtain the shift due to changing carrier density only. This is also show in figure 5.5 as open squares along with the linear fit showing a small negative shift of –0.0015 Å/mA. Therefore the total shift due to resistive heating is ~0.0336 Å/mA. Figure 5.6 shows the shift of the same peak with small changes in substrate temperature using three different current pulse heights where small changes in temperature were used to make sure we could track an individual peak. We see that there is little difference in the data from the different current pulses and we use an average shift with temperature of 0.88 Å/°C. Thus we can find the thermal impedance of the laser by dividing the shift due to current heating by the shift with temperature. We obtain 0.038°C/mA for these ~500μm long lasers which we can now use to adjust the substrate temperature and maintain constant active region temperature when the DC bias current is increased. This adjustment was used for all lifetime measurements as well as the gain measurements described next.

5.3) Gain

Material gain is another important laser property that has been blamed for the high temperature dependence of threshold, both through the transparency carrier density and the differential gain [1]-[4]. The most common method for measuring gain in Fabry-Perot lasers was first described by Hakki and Paoli [17]. In this method the net modal gain G is determined from the peak to valley ratio of the amplified spontaneous emission (ASE) and equation (5.4)

$$G = \frac{1}{L}\ln\left(\frac{r^{1/2}-1}{r^{1/2}+1}\right) = \Gamma g - \alpha_m - \alpha_i \tag{5.4}$$

where L is the cavity length, r is the peak to valley ratio of the ASE, Γ is the optical confinement factor, g is the material gain, α_m and α_i are the mirror and internal loss

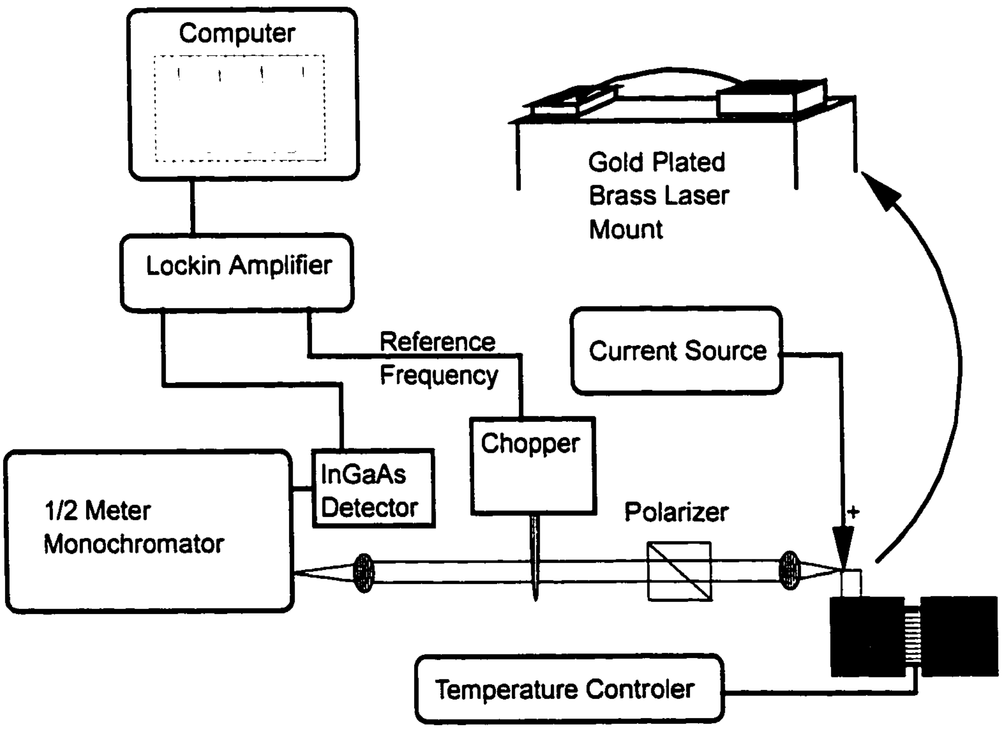

Fig. 5.7 - Experimental setup for measuring the amplified spontaneous emission spectra

respectively. The setup for these measurements is shown in figure 5.7 and is very similar to the spontaneous emission measurement setup discussed in chapter 4. The main differences are that the light is collected from one of the facets of the laser instead of the side, and that the monochromator slit openings are very small, less than 20μm, so that we can properly resolve the cavity resonance peaks. It is important to scan the wavelength slowly so that the peaks are not reduced due to filtering, this is especially important near threshold where the gain is high and the resonance peaks are very narrow. We used a

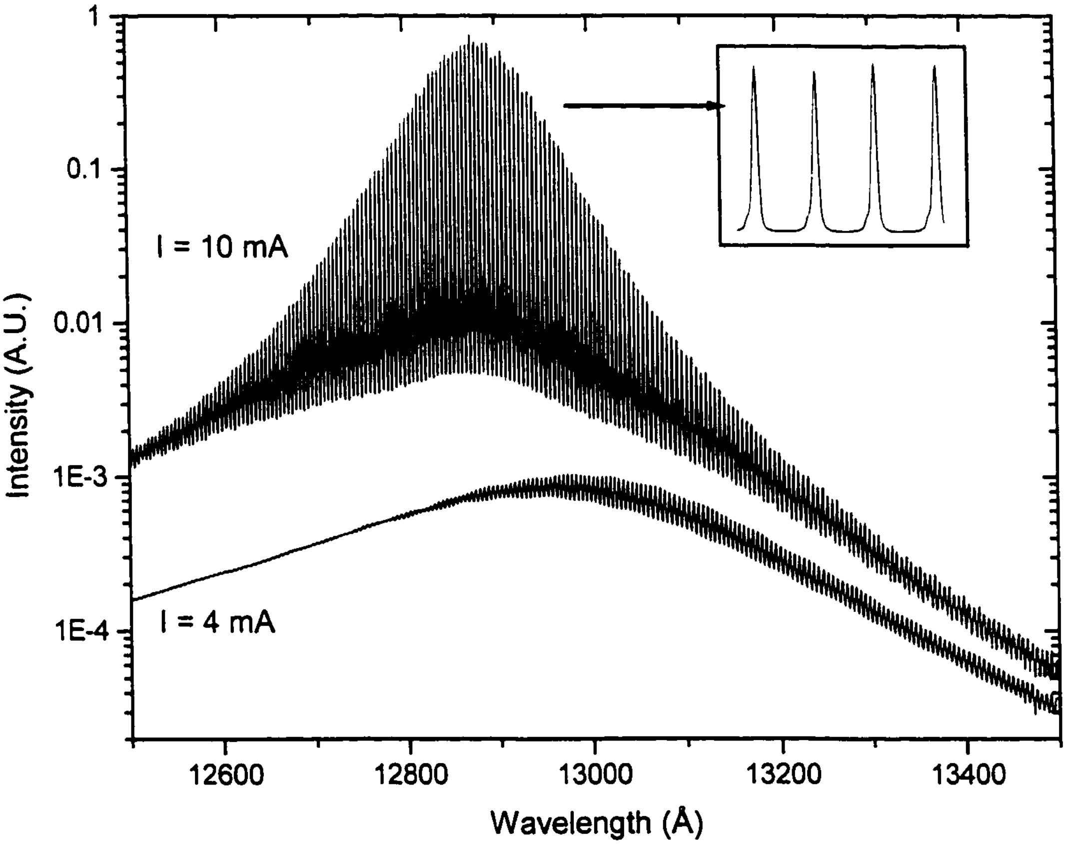

Fig. 5.8 - Amplified spontaneous emission spectra from deep well InAsP laser at T=20°C

scan speed of 0.2 Å/s, a filter time constant of 100 ms (300 ms for lower bias curves), and a sample rate of ~3 samples/s to collect the data.

Examples of the ASE curves collected from a 518 μm long deep well InAsP laser sample at T=20°C and bias currents of 4 mA and 10 mA are shown in figure 5.8. The 10 mA curve is very near threshold while 4 mA is just above transparency. From the 10 mA curve we see the importance of a low noise, high dynamic range, measurement system as the signal intensity changes by more than 4 order of magnitude. These curves are processed using a basic program that fits the peaks and valleys to a parabola to more

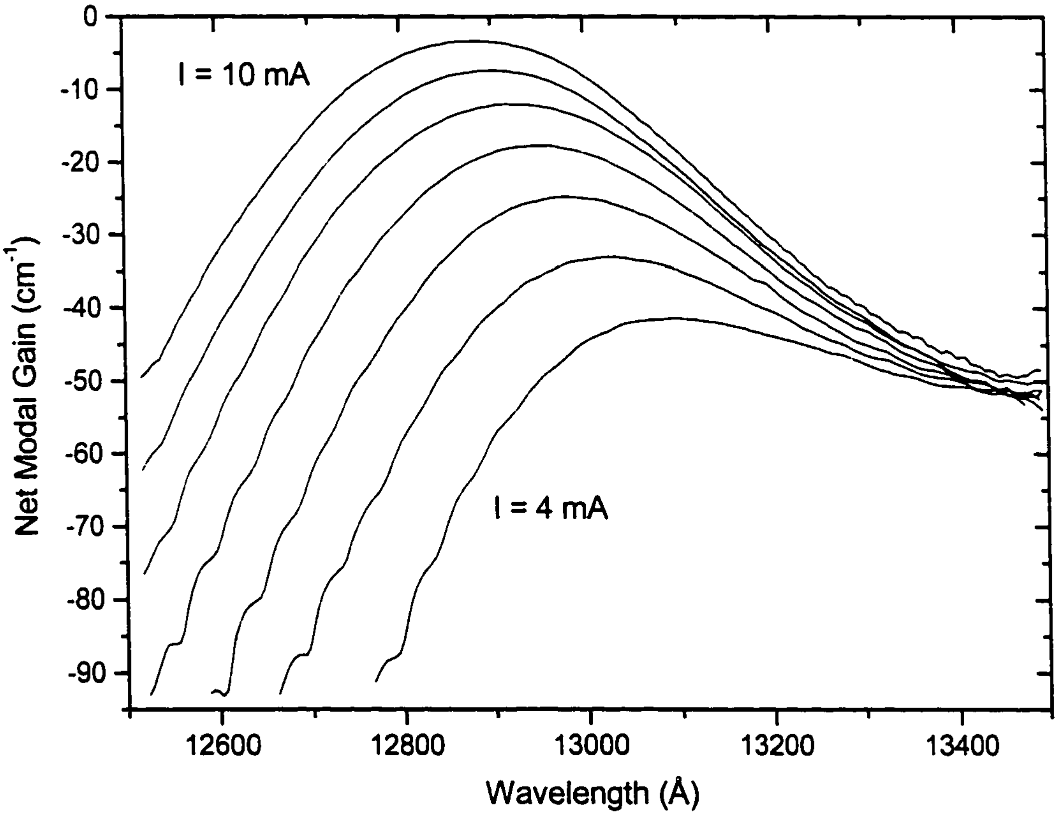

Fig 5.9 - Net modal gain G spectra at bias currents from 4 to 10mA for deep well InAsP laser at T=20°C

accurately find the extrema and then calculates the net modal gain G from (5.4). This is shown in figure 5.9 where we see that the peak gain increases and shifts to lower wavelength as the bias current increases. The peak gain at threshold should be 0 cm^{-1} while we measure -3 cm^{-1}. Most of this discrepancy comes from the finite spectral resolution of the monochromator that reduces the measured peaks and therefore underestimates the true gain. There are other methods of analyzing the ASE spectra to determine the gain which factor out the response of the monochromator [18], but they are more complicated and not deemed necessary here.

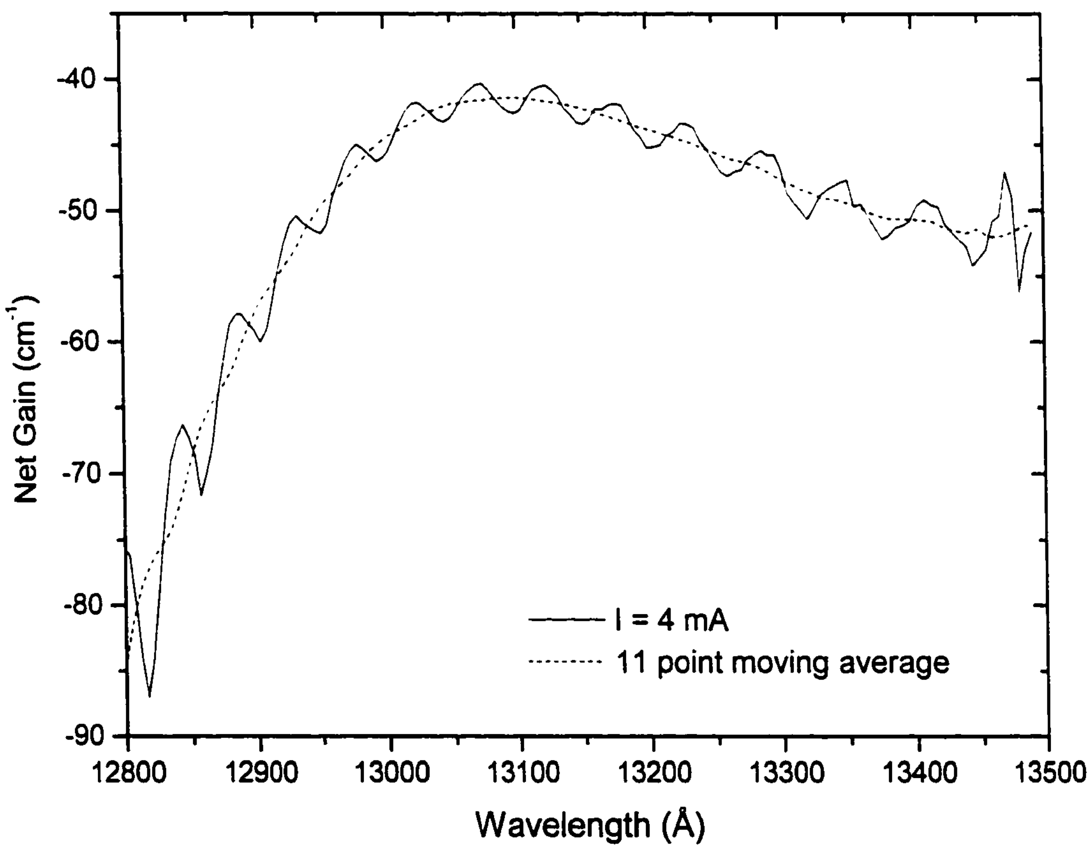

Fig 5.10 - Net modal gain G at 4mA bias current for deep well InAsP laser at T=20°C, both before averaging and after.

There were two major problems that showed up during the gain measurements. The first problem was a noticeable modulation in the gain spectra, particularly at low currents, i.e. near transparency. This is illustrated in figure 5.10 which shows both the unfiltered gain spectra and the same gain spectra that has been put through a moving average filter. The unfiltered curve shows significant modulation with a periodicity of around 50Å. All of the deep well lasers tested suffered from this problem but all had different periods and amplitudes of modulation. We believe that this is due to the presence of cavity defects that partially reflect the light, breaking the cavity up into two or more cavities [19]. The modulation depth would therefore depend on the strength of the reflection and the period would depend on the location of the defect in the cavity. Because the yield on this material was so low we were not able to find a laser that did not exhibit this problem. Thus we chose a laser where the modulation period was short, which enabled us to filter out most of the unwanted modulation as shown in the figure. However, since this problem was most severe at low gain we were still not able to collect gain spectra all the way down to transparency. As we will see later this will have some effect on the accuracy of our determination of the transparency carrier density.

The second problem in these measurements arose from very sharp, anomalous features in the ASE spectra observed above 13,450 Å. Since this was at the long wavelength end of the gain spectra it mostly affected the determination of the losses as we will describe later and was only important above room temperature. Considerable effort was made to eliminate these features including different lens, monochromators, gratings, and detectors all without success. We now believe that these features are water vapor absorption lines and that it is not possible to eliminate them without a closed

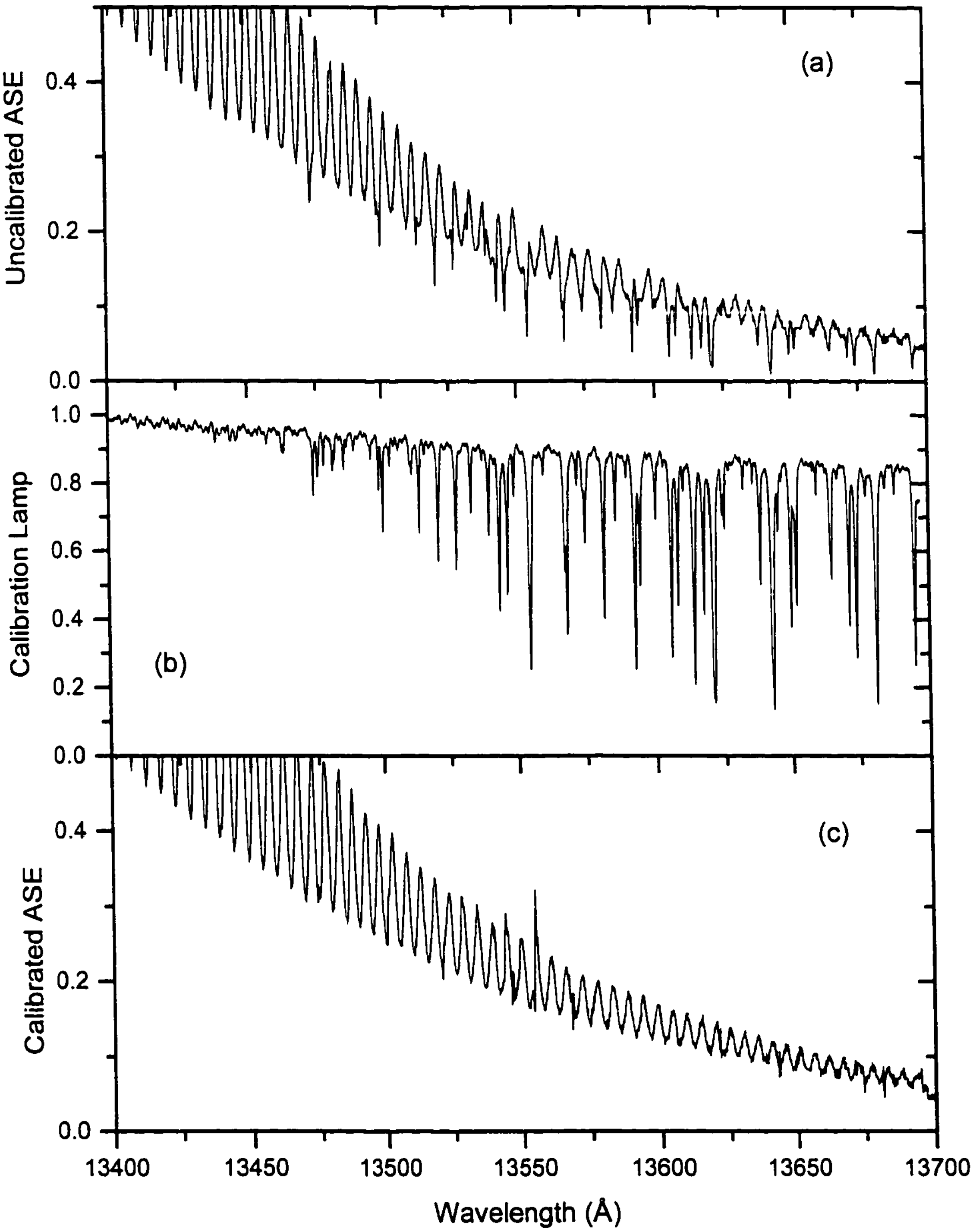

Fig. 5.11 - Calibration of ASE spectra to remove anomalous spikes; (a) uncorrected spectra; (b) water vapor spectra obtained with lamp; (c) corrected gain spectra

system. It was found, however, that the features were reproducible and could be mostly calibrated out using calibration curves from a tungsten-halogen lamp. Figure 5.11 illustrates the effectiveness of this procedure on the long wavelength end of an ASE spectra taken at 60°C. The top panel in figure 5.11 shows the uncorrected ASE spectra in the wavelength range from 13,400 to 13,700 Å, where we see many very sharp drops in the ASE spectra. Since the program written to analyze the ASE spectra is looking for the peaks and valleys it naturally has a difficult time separating the true peaks and valleys from the water vapor lines. The center panel is the calibration curve taken using a tungsten-halogen lamp where we see the same sharp spectra as in the laser ASE spectra. The trick now is to line up the spikes in the two curves and divide the ASE by the calibration curve. While the spikes are very consistent in wavelength the magnitude of the absorption lines is not completely consistent. We speculate that this is due to changes in room humidity and some of this effect was factored out. This was accomplished by picking a single spike from each curve that was easy to isolate visually. The calibration curve was then multiplied by a constant factor and renormalized to unity. The constant multiplier factor was adjusted until the chosen spike was properly calibrated out. This generally did not require a large change in the amplitude of the calibration curve absorption lines but it did provide more complete calibration of all of the spikes in the data. The lower panel in figure 5.11 is an example of a final corrected ASE curve that was used to calculate the gain spectra. We see that most of the spikes have been removed but that the data is still not as clean as the data outside of this spectral region.

The long wavelength saturation of the gain seen in figure 5.9 is an important region of the gain spectra. Since this region is below band-gap there is zero material

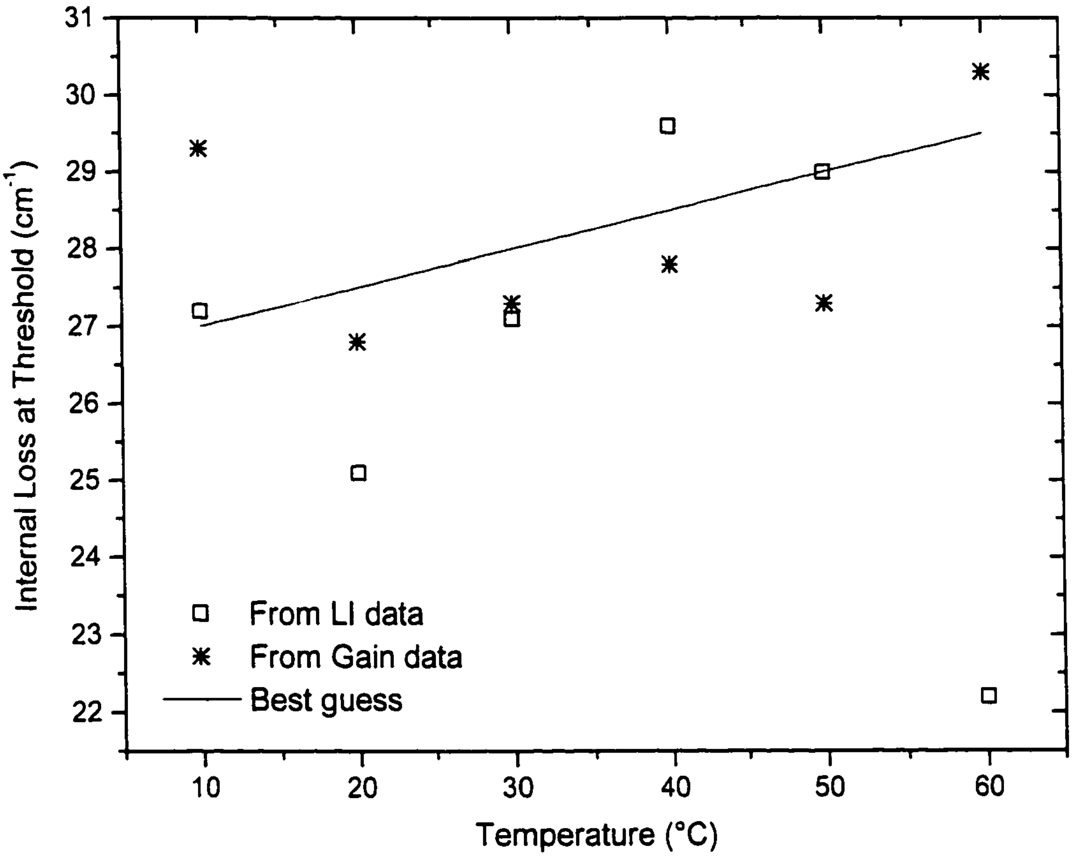

Fig 5.12 - Internal loss as determined from LI (open squares), Gain (stars), and best guess (straight line)

gain/loss and what we measure here is the total loss of the cavity. Thus theoretically, we can determine the internal loss from this figure since it is just the total loss minus the mirror loss, which we can easily calculate. Figure 5.12 shows the internal loss determined from the LI data of section 5.1 (open squares) compared to the internal loss determined from the gain spectra (stars). From figure 5.12 we can see that there is a large scatter in the data and thus large uncertainty in the internal loss obtained from these measurements. In order to get as close as possible to the actual internal loss we also take into consideration information on internal loss from other similar lasers [2] which show a slight positive temperature dependence. Thus the best guess line in figure 5.12 is just that, an educated guess based on our measurements and those of others [2]. We now use these best guess numbers for α_i, shown in table 5.2, and fix this parameter in the fitting of the inverse efficiency data of section 5.1. This provides the internal efficiency values also shown in table 5.2.

Table 5.2 – Temperature dependence of internal efficiency and loss in deep well InAsP laser

Temperature	η_i	α_i
10	.929	27
20	.906	27.5
30	.865	28
40	.819	28.5
50	.775	29.0
60	.724	29.5

The largest difference between these values and table 5.1 is a slightly slower and more consistent drop in η_i. The values shown in table 5.2 are used for both the carrier lifetime analysis of chapter 4 and the analysis of the temperature dependence of the threshold current in the next section.

While the internal loss information is useful, the most important information we can obtain from the gain data is the material gain. From the measured net modal gain, the calculated optical confinement factor, and eqn. (5.4), we can calculate the material gain. The optical confinement factor was calculated using the finite difference method and knowledge of the layer structure, shown in section 2.3, and the index profile, discussed in section 4.2.2. An example of the Mathcad program developed to perform this calculation is given in appendix C where we see that Γ for the deep well laser is found to

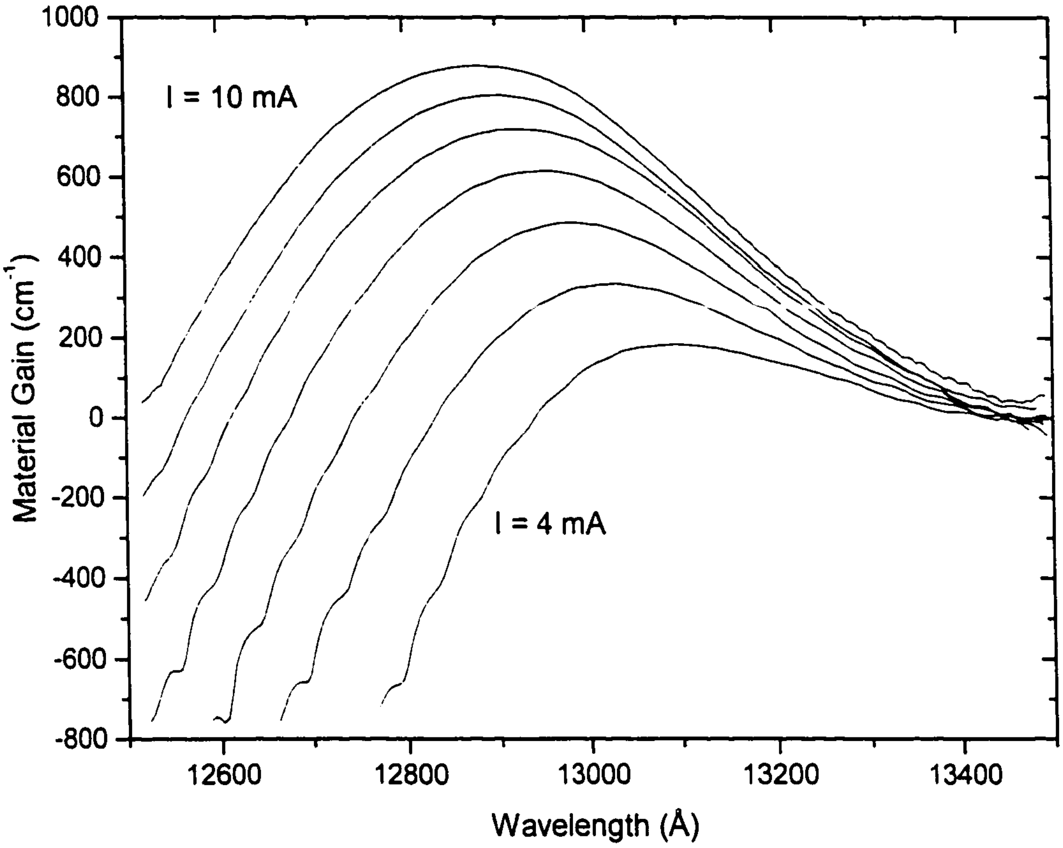

Fig 5.13 - Material gain g spectra at bias currents from 4 to 10 mA for deep well InAsP laser at T=20°C

be 0.05486. Using this Γ and the losses of table 5.2 we calculate the material gain as shown in figure 5.13. Note that we assume α_i is not a function of bias only because we are not able to measure the bias dependence of this parameter using the techniques described here [2]. Lasing will occur from the cavity mode nearest the gain peak and since the cavity modes are very closely spaced (~5 Å) we assume that lasing occurs from the gain peak. Thus the peak material gain is the value we are most interested in.

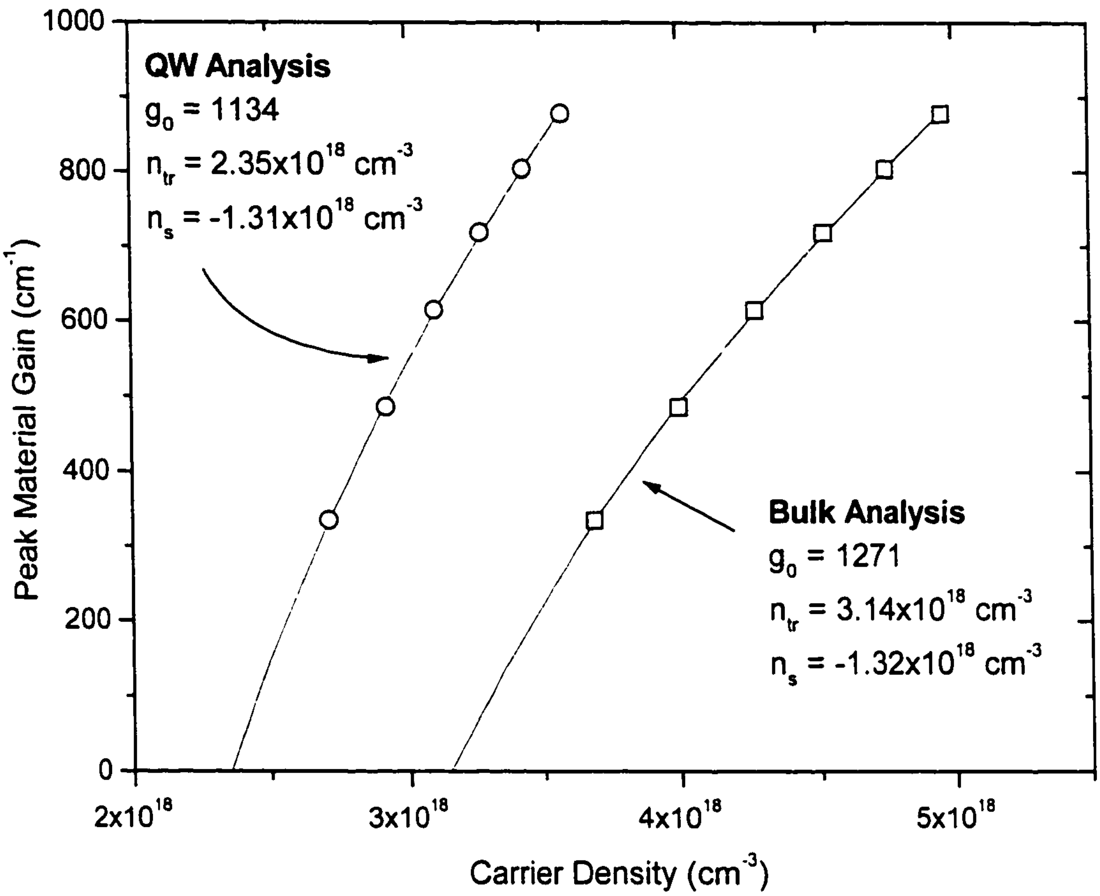

Fig 5.14 - Comparison of peak material gain versus carrier density using QW and bulk analysis in deep well laser at T=20°C

Figure 5.14 shows the peak material gain versus carrier density for the deep well laser at 20°C. In this plot the carrier density is calculated using both the bulk analysis and the new QW analysis. Unfortunately the shape of the gain curve is not linear with carrier density and we need to use a little more complicated gain expression than the simple linear relationship that is traditionally used. This is not unusual for QW lasers, particularly strained QW lasers like ours, which frequently require a logarithmic gain expression as shown in eqn (5.5) [16].

$$g = g_0 \ln\left(\frac{n + n_s}{n_{tr} + n_s}\right) \tag{5.5}$$

In this equation g_0 is an empirical gain coefficient, n_{tr} is the transparency carrier density, and n_s is a shift to force the gain to be equal to the unpumped absorption at n=0. The fits are shown in the figure along with the extracted parameters for both sets of carrier densities. We see that the transparency carrier density, n_{tr}, is lower using the new QW analysis while the other gain parameters are mostly unchanged. Still, considerable error would result in the threshold current model if the bulk analysis gain parameters were used instead of the intrinsic QW parameters. We also see that, due to the modulation discussed earlier, the lowest gain point that we can obtain data for is quite far above transparency (~300 cm^{-1}), making it difficult to accurately extract n_{tr} from the data.

Material gain data was obtained on the deep well InAsP lasers from 10°C to 40°C in order to determine the importance of gain changes due to temperature in the overall temperature dependence of threshold. Figure 5.15 shows the material gain versus well carrier density of these lasers while table 5.3 contains the fitted gain parameters from fitting these data to equation (5.5). From these data we see a steady increase in transparency carrier density from 10°C to 40°C and only small changes in the other gain parameters. Unfortunately while we measured the gain at 50°C and 60°C, the results were very unusual and in direct contradiction with what we would expect from figure 5.15 and theory. The 50°C and 60°C data reversed the trend seen in figure 5.15 and indicated that it was possible to achieve similar gain at 60°C with lower carrier densities than at 50°C or even 40°C. We believe this is due to the drop in internal efficiency measured at 50°C and 60°C and shown in table 5.2. We assumed that the injection efficiency was equal to the measured internal efficiency when we calculated carrier

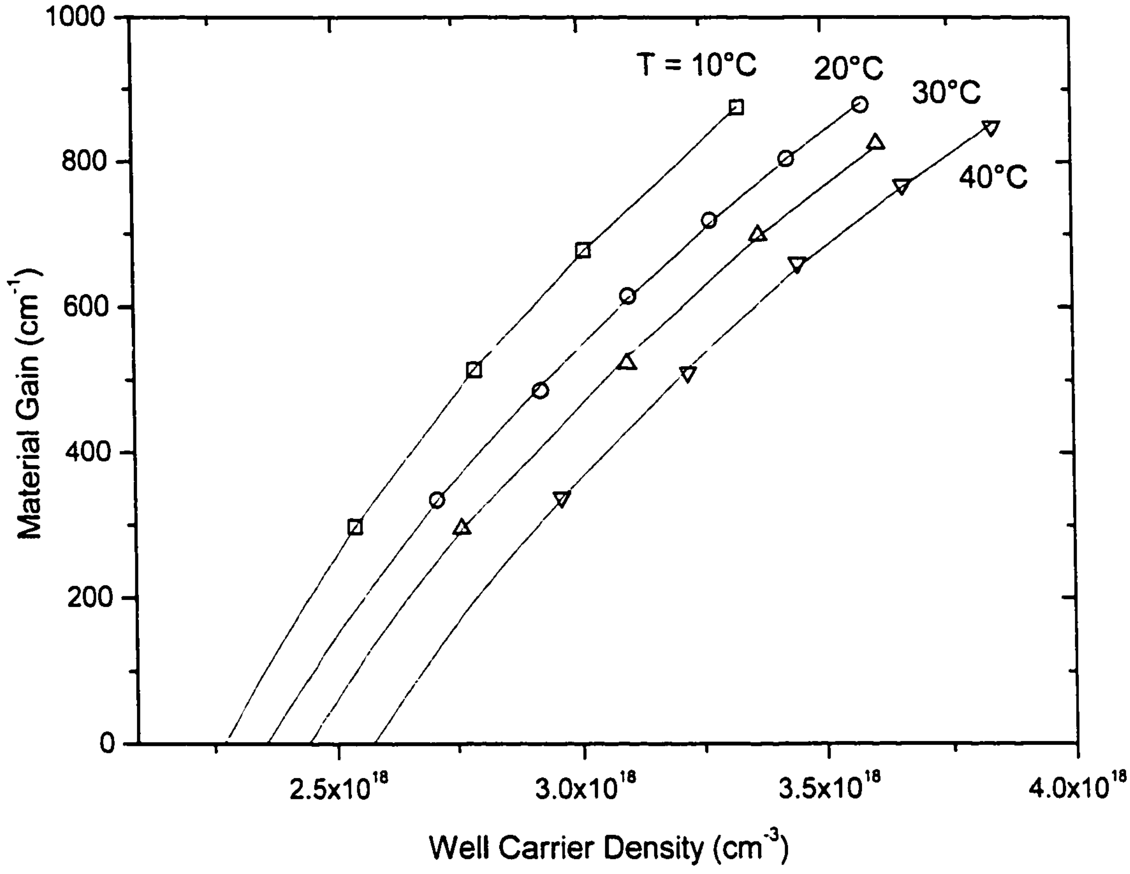

Fig. 5.15 - Temperature dependence of material gain versus well carrier density of deep well InAsP laser

densities from the lifetime data in chapter 4. It has been shown that non-uniform carrier density among the QWs can also lead to reduced efficiency [20], which may mean that we underestimated η_{inj} and overestimated its temperature dependence. This would lead to slightly lower recombination coefficients and higher carrier densities at higher temperatures. There are several other possible causes of this unexpected behavior at higher temperatures and more work is clearly needed to more fully understand this effect. For now we assume the trend above 40°C is not real and limit our temperature analysis to the range of 10°C to 40°C.

Table 5.3 – Temperature dependence of gain parameters in deep well InAsP laser

Temperature	$\eta_{tr} \times 10^{-18}$	g_0	$n_s \times 10^{-18}$
10	2.27	1107	-1.39
20	2.35	1134	-1.31
30	2.44	1086	-1.40
40	2.57	1079	-1.52
50	2.53	841	-1.75
60	2.52	593	-2.16

5.4) Model Analysis

We now have all the information we need to model the temperature dependence of the laser threshold current and to look at what happens when we eliminate expected sources of the problem. To calculate the threshold current at a given temperature we plug the threshold carrier densities for each region into equation (4.13).

$$\begin{aligned} I_{th}(T) = \frac{q}{\eta_{inj}(T)} [\; & V_w\left(A(T)n_{wth}(T) + B_w(T)n_{wth}(T)^2 + C_w(T)n_{wth}(T)^3\right) \\ & + V_s\left(A(T)n_{sth}(T) + B_s n_{sth}(T)^2 + C_s n_{sth}(T)^3\right) \;] \end{aligned} \tag{5.6}$$

Where we have explicitly shown the temperature dependence of the laser parameters we are interested in. Since we have not measured the temperature dependence of the barrier/SCH recombination parameters we have left these as constants. This should not affect the results much since the carrier density in this region is very low and there is little recombination current. The temperature dependence of the intrinsic well recombination coefficients $A_w(T)$, $B_w(T)$, and $C_w(T)$ are obtained from the carrier lifetime measurements (chapter 3) and the QW rate equation analysis of chapter 4. The well threshold carrier density, n_{wth}, can be calculated because we know that at threshold the net modal gain, G, is zero. Thus we can set equation (5.4) to zero and use the gain expression (5.5) to solve for the n_{wth}.

$$n_{wth}(T) = \left(n_{tr}(T) + n_s(T)\right)\exp\left[\frac{\alpha_m + \alpha_i(T)}{\Gamma g_0(T)}\right] - n_s(T) \qquad (5.7)$$

Using the well threshold carrier density from this equation and the relationship between the well and barrier/SCH carrier density in equation (4.10) we can determine the barrier/SCH carrier density. Thus all terms in (5.6) and (5.7) are known and we can calculate the threshold current from 10°C to 40°C.

The top panel of figure 5.16 shows the measured threshold current (solid squares) along with a fit to the exponential equation (5.2). Also in the top panel is the calculated threshold current from the model described above (open circles). We see that the slope, T_0, of the calculated data agrees very well with the measured T_0 but that the calculated threshold currents are shifted higher by about 10 to 15%. As mentioned earlier, without gain data at lower gain it is very hard to accurately determine n_{tr}. As it turns out a difference of only 3.5% in n_{tr} completely removes the discrepancy between the measured and calculated threshold currents. This small change is well within the accuracy of the fitted n_{tr} and the new calculated threshold currents are shown as open diamonds in the figure. The agreement is now excellent and all further analysis is done assuming these slightly lower transparency carrier densities.

The advantage of the model is that we can now remove the suspected causes of the temperature dependence one at a time and see what happens to the threshold current and T_0. The lower panel in figure 5.16 shows the results when the temperature

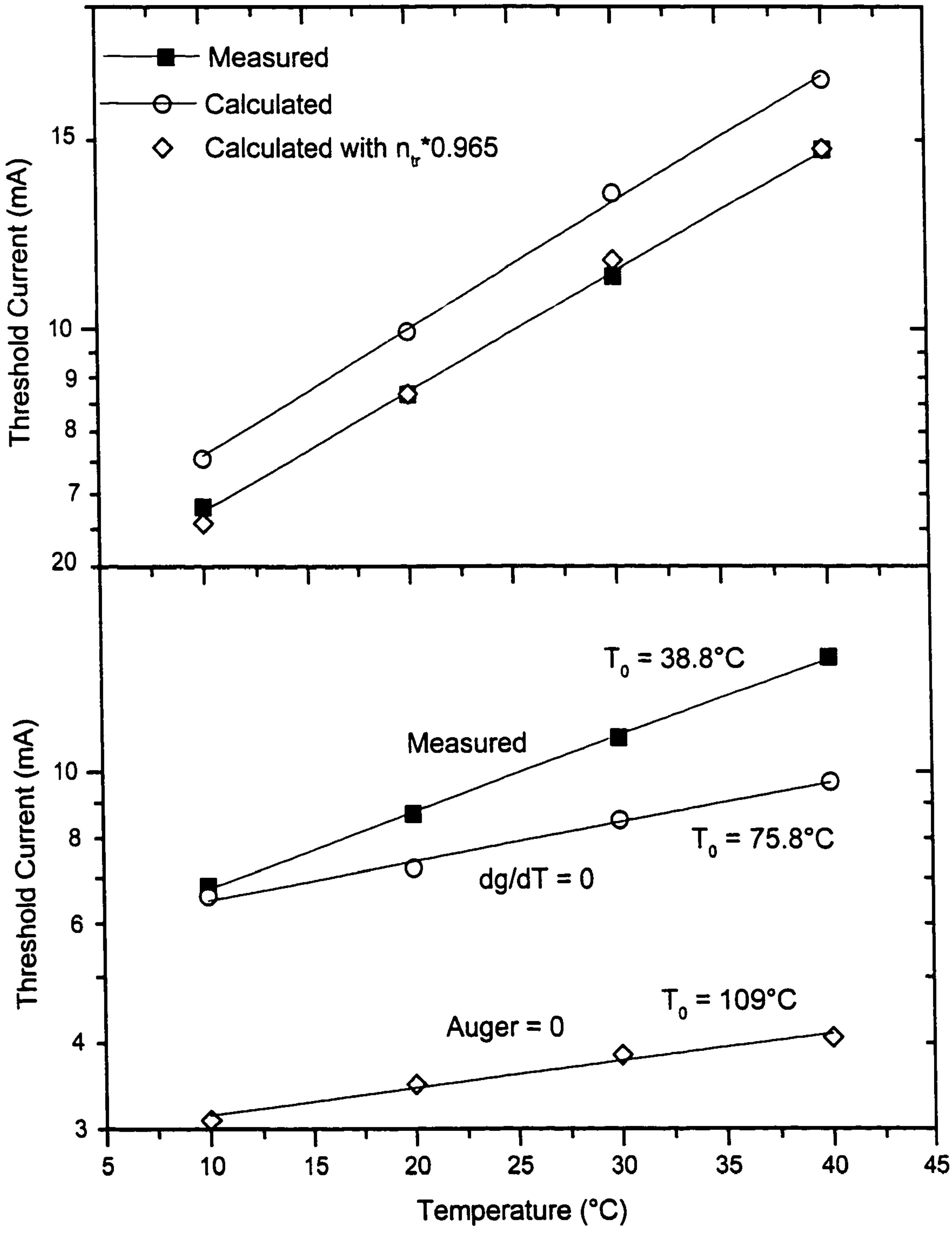

Fig. 5.16 - Model calculations of temperature dependence of threshold current and analysis of parameter sensitivity

dependence of the gain was eliminated and when Auger recombination was removed. We are interested in the effect Auger has on the temperature dependence of threshold current and Auger current increases both when C increases and when the threshold carrier density increases. Because of this we need to set the Auger rate to zero, not just its temperature dependence, in order to see its full effect on T_0. When investigating the effect of the other parameters on T_0 we set their temperature dependence to zero by using the 10°C values for all temperatures in the calculation. In the figure we see that compared to the measured data, setting either the Auger or the temperature dependence of the gain to zero results in considerable improvement in T_0. Removal of Auger has the largest effect yielding a T_0 of 109°C. The removal of Auger also results in considerable lowering of the threshold currents at all temperatures. This is expected since we saw in chapter 4 that even at 10°C Auger accounted for almost 60% of the threshold current. Removal of the temperature dependence of the gain did not lower the threshold current at low temperature but did provide considerable improvement in T_0, doubling it to 75.8°C.

Table 5.4 – Results of model analysis of temperature dependence of threshold

	I_0 (mA)	T_0 (°C)
Measured	5.21	38.8
Calculated	5.21	37.2
n_{tr}*0.965	5.08	37.3
$C = 0$	2.86	109
$dg/dT = 0$	5.68	75.8
$d\eta_{inj}/dt = 0$	5.36	44.5
$d\alpha_i/dt = 0$	5.16	39.3
$dR_t/dt = 0$	5.10	37.8
$\alpha_i/5$	3.28	43.2
$n_{tr}/1.25$	2.20	43.2

We also investigated the effect of the removal of the temperature dependence of several other parameters on T_0. The results of this analysis are summarized in table 5.4. Removing the temperature dependence of η_{inj} only increased T_0 to 44.5°C but we did notice that changes were beginning to occur at 40°C and it is possible that this parameter would be more important at higher temperatures. Changes in α_i do not seem to affect the results much either, but our model is somewhat limited since we did not measure the carrier density dependence of α_i. We also tried removing the temperature dependence of the ratio of well to barrier/SCH carriers by fixing R_t. Even though the barrier/SCH carrier population dramatically affects the carrier lifetime and the recombination coefficients it has little effect on the threshold current. This is because the barrier/SCH carrier density is still quite low and the lifetime of these carriers is long, thus few of these carriers recombine and contribute to the current. This situation could change at higher temperatures or with lasers that have lower QW barriers. Finally we looked at what would happen if the deep well laser material were improved. The deep well lasers had much higher internal losses than the very similar shallow well lasers, so we divided α_i by 5 to bring it down near what has been achieved in this material system in the past [21]-[24]. We see that the threshold currents do drop significantly but that the T_0 remains low. A similar result was obtained by lowering the transparency carrier density. Thus the parameters that control the temperature dependence of threshold in these lasers are Auger recombination and gain. We can also state that while Auger does dominate over gain in this temperature range, they are close enough that at higher temperatures this may not be the case, and to completely understand temperature dependence of this material system both processes must be considered.

References For Chapter V

[1] D. A. Ackerman, P. A. Morton, G. E. Shtengel, M. S. Hybertsen, R. F. Kazarinov, T. Tanbun-Ek, and R. A. Logan, "Analysis of T_0 in 1.3 μm Multi-Quantum-Well and Bulk Active Lasers," Appl. Phys. Lett., Vol. 66, No. 20, pp. 2613-2615, 1995

[2] D. A. Ackerman, G. E. Shtengel, M. S. Hybertsen, P. A. Morton, R. F. Kazarinov, T. Tanbun-Ek, and R. A. Logan, "Analysis of Gain in Determining T_0 in 1.3 μm Semiconductor Lasers," IEEE J. Selected Topics Quantum Electron., Vol., 1, No. 2, pp. 250-263, 1995

[3] Y. Zou, J. S. Osinski, P. Grodzinski, P. D. Dapkus, W. C. Rideout, W. F. Sharfin, J. Schlafer, and F. D. Crawford, "Experimental Study of Auger Recombination, Gain, and Temperature Sensitivity of 1.5μm Compressively Strained Semiconductor Lasers," IEEE J. Quantum Electron., Vol. **29**, No. 6, pp. 1565-1575, 1993

[4] A. A. Bernussi, J. Pikal, H. Temkin, D. L. Coblentz, and R. A. Logan, "Rate Equation Model of High-Temperature Performance of InGaAsP Quantum Well Lasers," Appl. Phys. Lett., Vol. 66, No. 26, pp. 3606-3608, 1995

[5] J. Braithwaite, M. Silver, V. A. Wilkinson, E. P. O'Reilly, and A. R. Adams, "Role of Radiative and Nonradiative Processes on the Temperature Sensitivity of Strained and Unstrained 1.5 μm InGaAs(P) Quantum Well Lasers," Appl. Phys. Lett., Vol. 67, No. 24, pp. 3546-3548, 1995

[6] S. J. Sweeney, A. F. Phillips, A. R. Adams, E. P. O'Reilly, and P. J. A. Thijs, "The Effect of Temperature Dependent Processes on the Performance of 1.5 μm Compressively Strained InGaAs(P) MQW Semiconductor Diode Lasers," IEEE Photon. Technol. Lett., Vol. 10, No. 8, pp. 1076-1078, 1998

[7] W. Fang, M. Hattendorf, S. L. Chuang, J. Minch, C. S. Chang, C. G. Bethea, and Y. K. Chen, "Analysis of Temperature Sensitivity in Semiconductor Lasers Using Gain and Spontaneous Emission Measurements," Appl. Phys. Lett., Vol. 70, No. 7, pp. 796-798, 1997

[8] T. Higashi, S. J. Sweeney, A. F. Phillips, A. R. Adams, E. P. O'Reilly, T. Uchida, and T. Fujii, "Observation of Reduced Nonradiative Current in 1.3-m AlGaInAs-InP Strained MQW Lasers," IEEE Photon. Technol. Lett., Vol. 11, No. 4, pp. 409-411, 1999

[9] G. E. Shtengel, D.A. Ackerman and P.A. Morton, "True Carrier Lifetime Measurements of Semiconductor Lasers," Electron. Lett., Vol. 31, No. 20, pp. 1747-1748, 1995

[10] G. E. Shtengel, D.A. Ackerman, P.A. Morton, E. J. Flynn, and M. S. Hybertsen, "Impedance-Corrected Carrier Lifetime Measurements in Semiconductor Lasers," Appl. Phys. Lett., Vol. **67**, No. 11, pp. 1506-1508, 1995

[11] T. Yamamoto, T. Odagawa, K. Tanaka, and S. Ogita, "Influence of Separate Confinement Heterostructures on the Effective Carrier Recombination Coefficient in Quantum Well Laser Structures," Appl. Phys. Lett., Vol. 71, No. 11, pp. 1543-1545, 1997

[12] A. P. Ongstad, D. J. Gallant, and G. C. Dente, "Carrier Lifetime Saturation in InGaAs Single Quantum Wells," Appl. Phys. Lett., Vol. 66, No. 20, pp. 2730-2732, 1995

[13] Y. C. Chen, P. Wang, J. J. Coleman, D. Bour, K. K. Lee, and R. G. Waters, "Carrier Recombination Rates in Strained-Layer InGaAs-GaAs Quantum Wells," IEEE J. Quantum Electron., Vol. 27, No. 6, pp. 1451-1454, 1991

[14] G. P. Agrawal and N. K. Dutta, "*Semiconductor Lasers*," 2nd ed., Van Nostrand Reinhold, New York, NY, 1993

[15] P. S. Zory, Jr., "*Quantum Well Lasers*," Academic Press, San Diego, CA, 1993

[16] L. A. Coldren and S. W. Corzine, "*Diode Lasers and Photonic Integrated Circuits*," John Wiley and Sons, New York, NY, 1995

[17] B. W. Hakki and T. L. Paoli, "Gain Spectra in GaAs Double-Heterostructure Injection Lasers," J. Appl. Phys., Vol. 46, No. 3, pp. 1299-1306, 1975

[18] D. T. Cassidy, "Technique for Measurement of the Gain Spectra of Semiconductor Diode Lasers," J. Appl. Phys. Vol. 56, No. 11, pp. 3096-3099, 1984

[19] D. Hofstetter and R. L. Thorton, "Measurement of Optical Cavity Properties in Semiconductor Lasers by Fourier Analysis of the Emission Spectrum," IEEE J. Quantum Electron., Vol. 34, No. 10, pp. 1914-1923, 1998

[20] J. Piprek, P. Abraham, and J. Bowers, "Carrier Nonuniformity Effect on the Internal Efficiency of Multiquantum-Well Lasers," Appl. Phys. Lett., Vol. 74, No. 4, pp. 489-491, 1999

[21] M. Yamamoto, N. Yamamoto, and J. Nakano, "MOVPE Growth of Strained InAsP/InGaAsP Quantum-Well Structures for Low-Threshold 1.3-μm Lasers," IEEE J. Quantum Electon., Vol. 30, No. 2, pp. 554-560, 1994

[22] P. Thiagarajan, A. A. Bernussi, H. Temkin, G. Y. Robinson, A. M. Sergent, and R. Logan, "Growth of 1.3 μm InAsP/InGaAsP Laser Structures by Gas Source Molecular Beam Epitaxy," Appl. Phys. Lett., Vol. 67, No. 25, pp. 3676-3678, 1995

[23] P. Thiagarajan, G. E. Giudice, H. Temkin, G. Y. Robinson, "Low Threshold Current 1.3 μm InAsP/InGaAsP Lasers grown by Gas-Source Molecular Beam Epitaxy," Electron. Lett., Vol. 32, No. 12, pp. 1103-1105, 1996

[24] P. Thiagarajan, "InAsP/InGaAsP Multiple Quantum Well Lasers," Doctoral Dissertation, Colorado State University, 1996

Chapter VI

Conclusions

The objective of this work was to understand the temperature dependence of the threshold current in long wavelength InAsP/InGaAsP semiconductor lasers. We accomplished this by measuring the temperature dependence of the most critical laser material parameters and then developing a model that predicted the lasers' behavior. We then varied the parameters in the model expected to contribute most significantly to the temperature dependence to see how the threshold current was affected.

The bulk of the work presented here was in the development of new measurement techniques and analysis of the carrier lifetime. We showed that the turn on delay technique and the traditional small signal optical technique yielded the same lifetime but that the small signal technique was more useful since it provided the carrier lifetime as a function of bias current. We also investigated the dramatic effect that laser impedance had on the lifetime obtained from the traditional small signal optical response technique. To remove the effect of the changing laser impedance with bias and frequency from the measured lifetime, we studied two previously proposed techniques. The first one incorporated a correction for the laser impedance to the optical technique and the second obtained the lifetime from the measured frequency response of the laser impedance. We also developed a new technique, which we called the impedance independent optical technique, where we added an impedance stabilization circuit to the traditional small signal optical technique. We showed that while all three of these techniques produced the same carrier lifetime, our technique has several advantages over the other two previously reported methods. The main advantage of our technique over the electrical impedance technique is that it requires only two fitting parameters allowing the lifetime to be extracted from data taken at much lower frequencies. The lower frequencies used allow accurate determination of the lifetime in QW lasers by determining the lifetime from data at frequencies below where any possible transport and capture poles and zeros become important. In addition, our technique is simpler, more accurate, and has a lower noise floor than the impedance corrected optical technique.

The most significant contribution of this work was the development of a rate equation analysis of the carrier lifetime as a function of bias current specifically for QW lasers. This analysis has allowed us, for the first time, to extract intrinsic properties of the well material that comprise the laser active region and thus accurately evaluate the contribution of the processes that affect the laser threshold current and its temperature behavior. Previously, this analysis had been performed using equations derived from the bulk laser rate equations even though it was known that this was not valid. Our new rate equation analysis included an additional carrier equation to account for carriers in the barrier/SCH region. This analysis showed that the measured lifetime was not the intrinsic well lifetime but a function of the intrinsic well lifetime, barrier/SCH lifetime, and the QW capture to escape ratio. We also derived an expression from the analysis that allowed us to extract the capture to escape ratio from the measured spontaneous emission spectra, thus allowing the determination of the intrinsic well carrier lifetime as well as the intrinsic recombination coefficients. The new QW analysis provided a very different picture of what goes on inside the laser. While the bulk analysis provided very different lifetimes and recombination coefficients for the shallow and deep well InAsP/InGaAsP lasers, the values obtained from the QW analysis were in good agreement with each other. This indicated that the analysis was properly accounting for and removing the effect of the barrier/SCH carrier population. By comparing the Auger coefficient C obtained from the QW analysis to that obtained from the bulk analysis we found that C was being masked by the barrier/SCH overflow. The QW analysis also revealed that the value of the intrinsic C coefficient in these highly strained QW lasers was higher than previously measured and close to bulk values reported for 1.3 μm lasers. Thus we believe that previous reports of C being very low and even insignificant in strained QW lasers are due to incorrect analysis of the lifetime data and not an intrinsic property of the highly strained system. The same can be said for the temperature dependence of C, which has been reported as either very small or even negative. While using the bulk analysis on our InAsP/InGaAsP lifetime data provides the same conclusion as previously found, the QW analysis reveals that the intrinsic C coefficient has a strong positive temperature dependence. Thus we have not only developed a proper analysis for carrier lifetime in QW lasers but also demonstrated the dramatic effect that not taking the barrier/SCH carrier population has on the measured laser material properties and their temperature dependence.

We also measured material gain versus carrier density on the deep well InAsP/InGaAsP lasers and again found a considerable difference between the material gain parameters determined from the bulk and QW analysis. The QW gain parameters produced lower transparency carrier density and larger differential gain than the bulk analysis. Using the QW gain parameters and the recombination coefficients obtained from the QW lifetime analysis a model of the laser was developed that allowed calculation of the threshold current. We found excellent agreement between the model calculation and measured threshold current versus temperature on the deep well InAsP/InGaAsP lasers tested. The mathematical model allowed us to remove certain parameters and/or their temperature dependence and determine the effect on the temperature dependence of the laser threshold current. Through this analysis we found that the most significant contribution to the temperature dependence of the threshold current is Auger recombination. However we also found that the temperature dependence of the gain is not far behind and should not be ignored. Interestingly, we found that, while the measured laser parameters are significantly affected by the barrier/SCH carrier population, the temperature dependence of the threshold current is not. This is because the lifetime of the carriers in the barrier/SCH region is long, and therefore they do not contribute significantly to the current but act more like a charge storage region. That may explain why even though the deep well lasers have much lower barrier/SCH emission than the shallow well lasers the T_0 is not any better. Thus when designing new laser structures in this material system it may be preferable to concentrate less on carrier confinement and more on optical confinement, leakage, and optical losses.

Despite the progress made here and elsewhere there is still a great deal of work to be done in this area. Because of the poor quality of the deep well lasers we were limited to a very small temperature range in our analysis. It is possible that at higher temperatures other effects will become more important, particularly leakage and barrier/SCH recombination. In our analysis we also made many assumptions, and the effect of these need to be understood. Internal loss as a function of carrier density and temperature need to be measured more directly. The difference between the measured internal efficiency and the injection efficiency as well as the bias dependence of the injection efficiency needs to be understood and included in the analysis. The assumption that the well radiative recombination follows a quadratic recombination law needs to be checked, as does the assumption of uniform carrier density. All of these may have an effect on the accuracy of the analysis performed here and need to be understood.

Appendix A – Band Alignment Calculation

InAsP/InGaAsP (MBE1015) Band diagram Calculations

This program **calculates confined energy levels, effective masses and wave functions in square strained-layer quantum wells of $InAs_{y_w}P_{1-y_w}/In_{1-x_b}Ga_{x_b}As_{y_b}P_{1-y_b}$ materials system, where $In_{1-x_b}Ga_{x_b}As_{y_b}P_{1-y_b}$ is lattice-matched to InP substrate.**

The schematic energy diagram for this system is as follows:

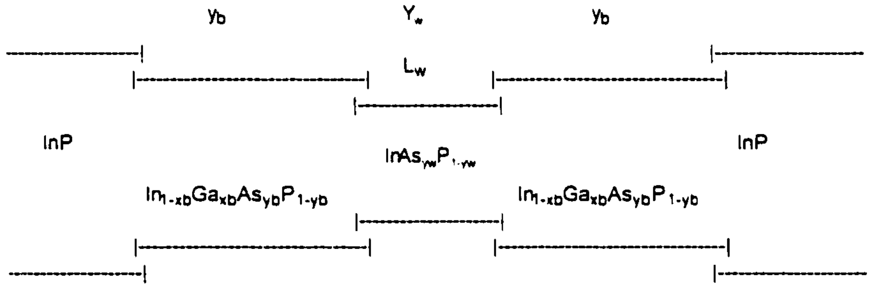

What we need to do in this program is to input

1) quantum well thickness L_W ,

2) As concentration Y_W of quantum well $InAs_{y_w}P_{1-y_w}$ and

3) Band gap E_{gb} of barrier $In_{1-xb}Ga_{xb}As_{yb}P_{1-yb}$ lattice-matched to InP.

$T := 20 + 273$ $\qquad$ $T = 293$ $\qquad$ $dm\_dT := 1.23 \cdot 10^{-3}$

$L_w := 5.0$ $\qquad$ in nanometer (10^9 m), quantum well thickness

$y_w := 0.47$ $\qquad$ As concentration Y_{erAs} of quantum well $InAs_yP_{1-y}$

$\lambda_{gb0} := 1.0611$ $\qquad$ in um. band gap of barrier quarternary $In_{1-x_b}Ga_{x_b}As_{y_b}P_{1-y_b}$ lattice-matched to InP

$$E_{gb} := \frac{1.23985}{\lambda_{gb0}} - 3.87 \cdot 10^{-4} \cdot (T - 293) \qquad E_{gb} = 1.1685$$

$$\lambda_{gb} := \frac{1.23985}{E_{gb}} \qquad \lambda_{gb} = 1.0611$$

$y_b := 0$ $\qquad$ $y_b := \mathrm{root}\left[1.35 - 0.775 \cdot y_b + 0.149 \cdot y_b^2 - \frac{1.23985}{\lambda_{gb0}}, y_b\right]$

$y_b = 0.2459$ $\qquad$ As concentration y_b of barrier $In_{1-x_b}Ga_{x_b}As_{y_b}P_{1-y_b}$ lattice-matched to InP

Part 1: ***Material Parameters***

1) material parameters for binaries InP,GaAs,InAs & GaP, and some constants

$E_{gInP} := 1.35 - 4.0 \cdot 10^{-4} \cdot (T - 293)$	$E_{gGaAs} := 1.425 - 3.95 \cdot 10^{-4} \cdot (T - 293)$	in eV, energy gaps at T,
$\Delta_{soInP} = 0.11$	$\Delta_{soGaAs} = 0.34$	in eV,
$m_{eInP} := 0.077 \cdot (1 + dm\_dT \cdot (T - 293))$	$m_{eGaAs} := 0.067 \cdot (1 + dm\_dT \cdot (T - 293))$	in emu, electron effective masses
$m_{lhzInP} := 0.121 \cdot (1 + dm\_dT \cdot (T - 293))$	$m_{lhzGaAs} := 0.094 \cdot (1 + dm\_dT \cdot (T - 293))$	in emu,
$m_{hhzInP} := 0.46 \cdot (1 + dm\_dT \cdot (T - 293))$	$m_{hhzGaAs} := 0.45 \cdot (1 + dm\_dT \cdot (T - 293))$	in emu,
$m_{soInP} := 0.17 \cdot (1 + dm\_dT \cdot (T - 293))$	$m_{soGaAs} := 0.15 \cdot (1 + dm\_dT \cdot (T - 293))$	in emu,
$a_{InP} = 5.86875$	$a_{GaAs} = 5.65315$	in A, lattice constants
$C_{11InP} = 10.22$	$C_{11GaAs} = 11.88$	in $*10^{11}$ dyn/cm^2
$C_{12InP} = 5.76$	$C_{12GaAs} = 5.38$	in $*10^{11}$ dyn/cm^2
$\Delta E_{g\Delta pInP} = 8.34$	$\Delta E_{g\Delta pGaAs} = 11.3$	in $*10^6$ eV*cm^2/kg
$a_{cInP} = -5.04$	$a_{cGaAs} = -7.17$	in eV
$a_{vInP} := 1.27$	$a_{vGaAs} := 1.16$	
$b_{vInP} = -1.6$	$b_{vGaAs} = -1.7$	in eV
$\chi_{0InP} = 12.4$	$\chi_{0GaAs} = 13.18$	dc dielectric constants
$E_{vavInP} = -7.04$	$E_{vavGaAs} = -6.92$	Average Valence Band

$E_{gInAs} := 0.36 - 3.5 \cdot 10^{-4} \cdot (T - 293)$	$E_{gGaP} := 2.78 - 4.6 \cdot 10^{-4} \cdot (T - 293)$	in eV, energy gaps
$\Delta_{soInAs} = 0.38$	$\Delta_{soGaP} = 0.08$	in eV,
$m_{eInAs} := 0.023 \cdot (1 + dm\_dT \cdot (T - 293))$	$m_{eGaP} := 0.82 \cdot (1 + dm\_dT \cdot (T - 293))$	in emu, electron effective masse
$m_{lhzInAs} := 0.026 \cdot (1 + dm\_dT \cdot (T - 293))$	$m_{lhzGaP} := 0.14 \cdot (1 + dm\_dT \cdot (T - 293))$	in emu,
$m_{hhzInAs} := 0.34 \cdot (1 + dm\_dT \cdot (T - 293))$	$m_{hhzGaP} := 0.4 \cdot (1 + dm\_dT \cdot (T - 293))$	in emu,
$m_{soInAs} := 0.05 \cdot (1 + dm\_dT \cdot (T - 293))$	$m_{soGaP} := 0.24 \cdot (1 + dm\_dT \cdot (T - 293))$	in emu,
$a_{InAs} = 6.05838$	$a_{GaP} = 5.4512$	in A, lattice constants
$C_{11InAs} = 8.329$	$C_{11GaP} = 14.39$	in $*10^{11}$ dyn/cm^2
$C_{12InAs} = 4.526$	$C_{12GaP} = 6.52$	in $*10^{11}$ dyn/cm^2
$\Delta E_{g\Delta pInAs} = 9.81$	$\Delta E_{g\Delta pGaP} = 11.0$	in $*10^6$ eV*cm^2/kg
$a_{cInAs} = -5.08$	$a_{cGaP} = -7.14$	in eV
$a_{vInAs} := 1.00$	$a_{vGaP} := 1.70$	
$b_{vInAs} = -1.8$	$b_{vGaP} = -1.5$	in eV
$\chi_{0InAs} = 14.6$	$\chi_{0GaP} = 11.1$	dc dielectric constants
$E_{vavInAs} = -6.67$	$E_{vavGaP} = -7.40$	Average Valence Band

$m_0 = 9.10956 \cdot 10^{-31}$ $\quad$ $hbar = 1.05459 \cdot 10^{-34}$ $\quad$ $eV = 1.60219 \cdot 10^{-19}$

a) David GERSHONI and Henryk TEMKIN, Journal of Luminescence 44,381-398,(1989)

b) Sadao Adachi, J. Appl. Phys. 53(12), 8775-8792, (1982)

c) G.P.Agrawal and N.K.Dutta, Long-wavelength semiconductor lasers, Chapter 4, p142-171

d) Sado Adachi, Physical Properities of III-V Semiconductor Compounds, 1992

$Q(x,y,B_{ac},B_{ad},B_{bc},B_{bd}) := (1 - x) \cdot y \cdot B_{ac} + (1 - x) \cdot (1 - y) \cdot B_{ad} + x \cdot y \cdot B_{bc} + x \cdot (1 - y) \cdot B_{bd}$ Veguard's Law

2) Material Parameters for lattice matched barrier material

a) relation between x and y for $In_{1-x}Ga_xAs_yP_{1-y}$ lattice-matched to InP substrate

$x_{qua}(y_{qua}) := \dfrac{0.18965 \cdot y_{qua}}{0.41758 - 0.01243 \cdot y_{qua}}$ Adachi '92 $x_b := x_{qua}(y_b)$ $x_b = 0.1125$

$y_{qua}(x_{qua}) := \dfrac{0.41758 \cdot x_{qua}}{0.18965 + 0.01243 \cdot x_{qua}}$ $y_b = 0.2459$

b) Effective masses Adachi '92

$m_{equa}(y_{qua}) := (0.080 - 0.039 \cdot y_{qua}) \cdot (1 + dm\_dT \cdot (T - 293))$ $m_{eb} := m_{equa}(y_b)$ $m_{eb} = 0.0704$

$m_{hhqua}(y_{qua}) := 0.46 \cdot (1 + dm\_dT \cdot (T - 293))$ $m_{hhb} := m_{hhqua}(y_b)$ $m_{hhb} = 0.46$

$m_{lhqua}(y_{qua}) := (0.12 - 0.099 \cdot y_{qua} + 0.03 \cdot y_{qua}^2) \cdot (1 + dm\_dT \cdot (T - 293))$ $m_{lhb} := m_{lhqua}(y_b)$ $m_{lhb} = 0.0975$

$m_{soqua}(y_{qua}) := (0.21 - 0.01 \cdot y_{qua} - 0.05 \cdot y_{qua}^2) \cdot (1 + dm\_dT \cdot (T - 293))$ $m_{sob} := m_{soqua}(y_b)$ $m_{sob} = 0.2045$

c) Bandstructure Parameters

$\Delta E_{g\Delta pb} := Q(x_b, y_b, \Delta E_{g\Delta pInAs}, \Delta E_{g\Delta pInP}, \Delta E_{g\Delta pGaAs}, \Delta E_{g\Delta pGaP})$ energy-gap dependence on hydrostatic pressure dEg/dp(x) $\Delta E_{g\Delta pb} = 8.9683$

$\chi_{0b} := Q(x_b, y_b, \chi_{0InAs}, \chi_{0InP}, \chi_{0GaAs}, \chi_{0GaP})$ DC dielectric constant $\chi_{0b} = 12.7914$

$\Delta_{sob} := Q(x_b, y_b, \Delta_{soInAs}, \Delta_{soInP}, \Delta_{soGaAs}, \Delta_{soGaP})$ spin orbit valence band splitting $\Delta_{sob} = 0.1727$

$\Delta_{soqua}(y_{qua}) := 0.119 + 0.3 \cdot y_{qua} - 0.107 \cdot y_{qua}^2$ $\Delta_{sob} := \Delta_{soqua}(y_b)$ $\Delta_{sob} = 0.1863$

$E_{vavb} := Q(x_b, y_b, E_{vavInAs}, E_{vavInP}, E_{vavGaAs}, E_{vavGaP})$ $E_{vavb} = -6.9865$

$R_{vbcA}(y_{qua}) := \dfrac{0.502 \cdot y_{qua} - 0.152 \cdot y_{qua}^2}{0.502 \cdot y_{qua} - 0.152 \cdot y_{qua}^2 + 0.268 \cdot y_{qua} + 0.003 \cdot y_{qua}}$ Adachi '92 $R_{vbcA}(y_b) = 0.6316$

3) Material parameters of unstrained bulk $InAs_yP_{1-y}$

This section calculates the parameters of unstrained bulk $InAs_yP_{1-y}$ by using the interpolation scheme. y_s is the As concentration of the ternary $InAs_yP_{1-y}$.

$P_{linterp}(P_{InP}, P_{InAs}, Y_{As}) := P_{InP}\cdot(1 - Y_{As}) + P_{InAs}\cdot Y_{As}$ — This is the definition of the linear interpolation.

$a_w := P_{linterp}(a_{InP}, a_{InAs}, y_w)$ — ternary $InAs_yP_{1-y}$ lattice constant: a — $a_w = 5.9579$

$C_{11w} := P_{linterp}(C_{11InP}, C_{11InAs}, y_w)$ — ternary $InAs_yP_{1-y}$ stiffness coefficients: C_{11} and C_{12} — $C_{11w} = 9.3312$

$C_{12w} := P_{linterp}(C_{12InP}, C_{12InAs}, y_w)$ — $C_{12w} = 5.18$

$m_{ew} := P_{linterp}(m_{eInP}, m_{eInAs}, y_w)$ — ternary $InAs_yP_{1-y}$ effective masses m_e, m_{lh}, m_{hh} and m_{so} — $m_{ew} = 0.0516$

$m_{lhw} := P_{linterp}(m_{lhzInP}, m_{lhzInAs}, y_w)$ — $m_{lhw} = 0.0764$

$m_{hhw} := P_{linterp}(m_{hhzInP}, m_{hhzInAs}, y_w)$ — $m_{hhw} = 0.4036$

$m_{sow} := P_{linterp}(m_{soInP}, m_{soInAs}, y_w)$ — $m_{sow} = 0.1136$

$\Delta E_{g\Delta pw} := P_{linterp}(\Delta E_{g\Delta pInP}, \Delta E_{g\Delta pInAs}, y_w)$ — ternary $InAs_yP_{1-y}$ energy-gap dependence on hydrostatic pressure dEg/dp(x) — $\Delta E_{g\Delta pw} = 9.0309$

$a_{vw} := P_{linterp}(a_{vInP}, a_{vInAs}, y_w)$ — $a_{vw} = 1.1431$

$a_{cw} := P_{linterp}(a_{cInP}, a_{cInAs}, y_w)$ — $a_{cw} = -5.0588$

$b_{vw} := P_{linterp}(b_{vInP}, b_{vInAs}, y_w)\cdot 0.704$ — ternary InxGa(1-x)As valence band shear deformation potential — $b_{vw} = -1.1926$

$\chi_{0w} := P_{linterp}(\chi_{0InP}, \chi_{0InAs}, y_w)$ — ternary $InAs_yP_{1-y}$ DC dielectric constant — $\chi_{0w} = 13.434$

$\Delta_{sow} := P_{linterp}(\Delta_{soInP}, \Delta_{soInAs}, y_w)$ — ternary $InAs_yP_{1-y}$ spin orbit valence band splitting — $\Delta_{sow} = 0.2369$

$E_{vavw} := P_{linterp}(E_{vavInP}, E_{vavInAs}, y_w)$ — $E_{vavw} = -6.8661$

The following parabolic interpolation model is used to estimate the ternary $InAs_yP_{1-y}$ energy-gap dependence on the In concentration.(III-V data book, M.Yamamoto IEEE JQE, Vol. 30, No.2, 554(1994))

$E_{gw0} := 1.351 - 1.315\cdot y_w + 0.32\cdot y_w^2$ — $E_{gw0} = 0.8036$

$E_{gw} := E_{gw0} - 2.71\cdot 10^{-4}\cdot(T - 293)$ — $E_{gw} = 0.8036$

We have calculated all the parameters of bulk strain-free ternary $InAs_yP_{1-y}$ which are needed in the computation. — $\frac{1.23985}{E_{gw}} = 1.5428$

Part 2 : Compute band offsets

1) Band offsets between $In_{1-xb}Ga_{xb}As_{yb}P_{1-yb}$ and InP

$E_{vavb} := 0.99571 \cdot E_{vavb}$ Change to achive 40/60 offset

$\Delta E_{gb} := E_{gInP} - E_{gb}$ $\Delta E_{gb} = 0.1815$

$E_{vb} := E_{vavb} + \frac{\Delta_{sob}}{3}$ $E_{vb} = -6.8944$

$E_{vInP} := E_{vavInP} + \frac{\Delta_{soInP}}{3}$ $E_{vInP} = -7.0033$

$\Delta E_{vb} := E_{vb} - E_{vInP}$ $\Delta E_{vb} = 0.1089$

$R_{vbcV} := \frac{\Delta E_{vb}}{E_{gInP} - E_{gb}}$ $R_{vbcV} = 0.6$

$\Delta E_{cb} := \Delta E_{gb} - \Delta E_{vb}$ $\Delta E_{cb} = 0.0726$

$E_{cb} := E_{vb} + E_{gb}$ $E_{cb} = -5.726$

$L_b := 20$

$E_c(x) := E_{gInP} \cdot \Phi(x + 2 \cdot L_b) - \Delta E_{cb} \cdot \Phi\left(x + \frac{L_b}{2}\right) + \Delta E_{cb} \cdot \Phi\left(x - \frac{L_b}{2}\right)$

$E_v(x) := \Delta E_{vb} \cdot \Phi\left(x + \frac{L_b}{2}\right) - \Delta E_{vb} \cdot \Phi\left(x - \frac{L_b}{2}\right)$

$x := -L_b, -L_b + 0.1 .. L_b$

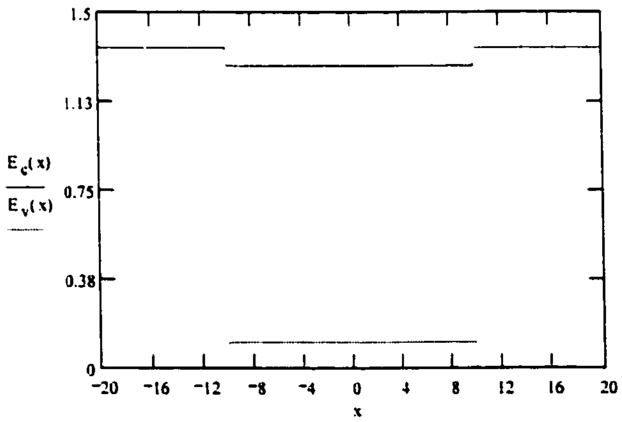

2) Band offsets between $In_{1-xb}Ga_{xb}As_{yb}P_{1-yb}$ and $InAs_{yw}P_{1-yw}$

$E_{vavw} := 0.999805 \cdot E_{vavw}$ Change to achive 45/55 offset of strained system $E_{vavw} = -6.8648$

$\Delta E_{gw} := E_{gb} - E_{gw}$ $\Delta E_{gw} = 0.3648$

$E_{vw} := E_{vavw} + \frac{\Delta_{sow}}{3}$ $E_{vw} = -6.7858$

a) Biaxial in-plane strain

$\varepsilon_{inplane} := \frac{a_{InP} - a_w}{a_w}$ biaxial in-plane strain tensor component (hydrostatic strain) $\varepsilon_{inplane} = -0.01496$

$\varepsilon_{perpen} := -2 \cdot \frac{C_{12w}}{C_{11w}} \cdot \varepsilon_{inplane}$ strain tensor component along the growth direction (uniaxial strain) $\varepsilon_{perpen} = 0.01661$

$\varepsilon_H := 2 \cdot \varepsilon_{inplane} + \varepsilon_{perpen}$ $\varepsilon_H = -0.0133$

$\varepsilon_U := \varepsilon_{perpen} - \varepsilon_{inplane}$ $\varepsilon_U = 0.0316$

$a_{gw} := \left[-\Delta E_{g\Delta pw} \cdot \frac{1}{3} \cdot \left(C_{11w} + 2 \cdot C_{12w} \right) \right] \cdot \frac{1}{9.8} \cdot 0.914$ $In_{1-xw}Ga_{xw}As_{yw}P_{1-yw}$ band-gap hydrostatic deformation potential $a_{gw} = -5.5285$

$\delta E_{gw} := a_{gw} \varepsilon_H$ band-gap change with the hydrostatic strain $\delta E_{gw} = 0.0736$

$E_{gwstr} := E_{gw} + \delta E_{gw}$ ***strain-induced*** $In_{1-xw}Ga_{xw}As_{yw}P_{1-yw}$ ***band-gap*** $E_{gwstr} = 0.8772$

$E_{cwstr} := E_{vavw} + E_{gwstr} + \frac{\Delta_{sow}}{3}$ $E_{cwstr} = -5.9086$

$a_{vw} = 1.1431$

b) Uniaxial strain

The **uniaxial strain** introduces two important effects. *First*, it removes the valence-band degeneracy at the Brillouin-zone center. *Second*, it mixes the (3/2,+-1/2) valence band and the (1/2,+-1/2) split-off valence band.

$\varepsilon_0 := b_{vw} \cdot \varepsilon_U$

the splitting between J=3/2, mj=3/2 (heavy hole) band and the J=3/2, mj=1/2 (light hole) band

$X := \dfrac{\varepsilon_0}{\Delta_{sow}}$

$\delta E_{001} := 2 \cdot b_{vw} \cdot \varepsilon_U$ $\qquad \delta E_{001} = -0.0753$

$X1 := \dfrac{1 + 9 \cdot X}{\left(1 + 2 \cdot X + 9 \cdot X^2\right)^{\frac{1}{2}}} - 1$

$m_{hhdosw} := \dfrac{1}{\dfrac{1}{m_{lhw}} + \dfrac{1}{4} \cdot \left(\dfrac{1}{m_{lhw}} - \dfrac{1}{m_{hhw}}\right) \cdot X1}$ $\qquad m_{hhdosw} = 0.1082$

$E_{vwhh} := E_{vavw} + a_{vw} \cdot \varepsilon_H + \dfrac{1}{3} \cdot \Delta_{sow} - \dfrac{1}{2} \cdot \delta E_{001}$ $\qquad E_{vwhh} = -6.7634$

$\Delta E_{hhstr} := E_{vwhh} - E_{vb}$ $\qquad \Delta E_{hhstr} = 0.1311$

$E_{vwlh} := E_{vavw} + a_{vw} \cdot \varepsilon_H - \dfrac{1}{6} \cdot \Delta_{sow} + \dfrac{1}{4} \cdot \delta E_{001} + \dfrac{1}{2} \cdot \left[\Delta_{sow}^2 + \Delta_{sow} \cdot \delta E_{001} + \dfrac{9}{4} \cdot \delta E_{001}^2\right]^{\frac{1}{2}}$ $\qquad E_{vwlh} = -6.8253$

$\Delta E_{lhstr} := E_{vwlh} - E_{vb}$ $\qquad \Delta E_{lhstr} = 0.0691$

$E_{glhstr} := E_{cwstr} - E_{vwlh}$ $\qquad E_{glhstr} = 0.9167$

$E_{cwstr} := E_{gwstr} + E_{vwhh}$ $\qquad E_{cwstr} = -5.8861$

$E_{ghhstr} := E_{gwstr}$

$\Delta E_{cw} := E_{cb} - E_{cwstr}$ $\qquad \Delta E_{cw} = 0.1602$

$\dfrac{\Delta E_{hhstr}}{\Delta E_{hhstr} + \Delta E_{cw}} = 0.45$ $\qquad E_{gb} = 1.1685$

$\dfrac{\Delta E_{hhstr} + \Delta E_{vb}}{\Delta E_{hhstr} + \Delta E_{vb} + \Delta E_{cw} + \Delta E_{cb}} = 0.5076$

Part 3: Quantum size effects

1) eletron levels in conduction band

Let us to evaluate the electron states in conduction band neglecting the effects of band nonparaboli

$$r_{e1}(E) := \left(\frac{m_{eb}}{m_{ew}} \cdot \frac{E}{\Delta E_{cw} - E}\right)^{\frac{1}{2}}$$

In this calculation,we use the effective mass in $*m_0$, E in eV and L_w in $*10^{-9}$m

$$r_{e22} := \left(\frac{2 \cdot m_0 \cdot eV}{hbar^2}\right)^{\frac{1}{2}} \cdot 10^{-9} \qquad r_{e22} = 5.1231$$

$$r_{e2}(E) := r_{e22} \cdot \left(m_{ew} \cdot E\right)^{\frac{1}{2}} \cdot L_w$$

$$f_e(E) := \left(r_{e1}(E) - \frac{1}{r_{e1}(E)}\right) \cdot \sin\left(r_{e2}(E)\right) - 2 \cdot \cos\left(r_{e2}(E)\right)$$

$$E := 0.001, 0.002 .. \Delta E_{cw} - 0.001$$

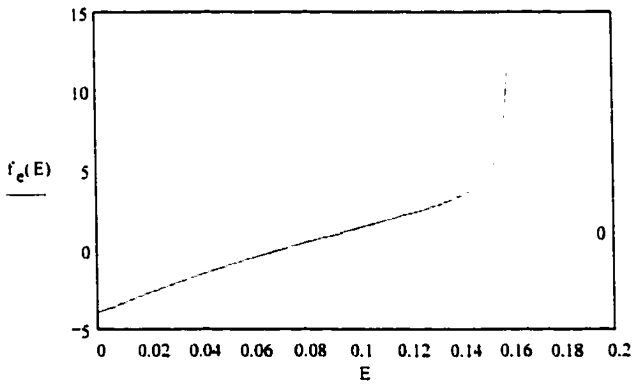

$Npoint := 100$

$Nvar := 0 .. Npoint - 1$

$$E_{e_{Nvar}} := \frac{Nvar + 0.1}{Npoint} \cdot \Delta E_{cw}$$

$$y_{e_{Nvar}} := f_e\left(E_{e_{Nvar}}\right) \qquad y_{e_{Npoint}} := y_{e_{Npoint-1}}$$

$$Nzer_0 := 0$$

$$Nzer_{Nvar+1} := \mathrm{if}\left(y_{e_{Nvar}} \cdot y_{e_{Nvar+1}} < 0, Nzer_{Nvar} + 1, Nzer_{Nvar}\right)$$

$$Nzer_e := Nzer_{Npoint}$$

$Nzer_e$ is the number of energy levels in conduction band

$N1 := 0 .. Nzer_e$

$intervals_{N1} := -0.5 + N1$

$Nth := hist(intervals, Nzer)$ $\quad Nth_0 := Nth_0 - 1$ $\quad Nthzero_0 := 0$

$N2 := 1 .. Nzer_e$ Nth is the distribution of zero points

$Nthzero_{N2} := Nthzero_{N2-1} + Nth_{N2-1}$ Nthzero is the order of points where function changes its sign

$N3 := 1 .. Nzer_e$

$Ezer_{N3-1} := E_{e\,Nthzero_{N3}}$ Ezer may be used for the initial values to find the solution

$N4 := 0$

$X := Ezer_{N4}$

$E_{ezer_{N4}} := root\left(f_e(X), X\right)$

$N4 := if\left(Nzer_e - 2 \ge 0, 1, 0\right)$

$X := Ezer_{N4}$

$E_{ezer_{N4}} := root\left(f_e(X), X\right)$

$N4 := if\left(Nzer_e - 3 \ge 0, 2, 0\right)$

$X := Ezer_{N4}$ $\quad N4 = 0$

$E_{ezer_{N4}} := root\left(f_e(X), X\right)$

$Nlevel_e := length\left(E_{ezer}\right)$ $\quad Nlevel_e = 1$ $\quad E_{ezer} = 0.0701$

Now we have obtained the ***electron energy levels of conduction band*** in ***E_{ezer}*** and the ***number of the energy levels*** in ***$Nlevel_e$***. Note that the ***maxium number*** we calculate is ***three***

2) *light hole levels in valence band*

Let us to calculate the light hole states in valence band of $_{x}Ga_{(1-x)}As$ neglecting the effects of band nonparabolicit

$$r_{lh1}(E) := \left(\frac{m_{lhb}}{m_{lhw}} \cdot \frac{E}{\Delta E_{lhstr} - E}\right)^{\frac{1}{2}}$$

In this calculation,we use the effective mass in $\cdot m_0$. E in eV and L_w in $\cdot 10^{-9}$m

$$r_{lh22} := \left(\frac{2 \cdot m_0 \cdot eV}{hbar^2}\right)^{\frac{1}{2}} \cdot 10^{-9}$$

$$r_{lh2}(E) := r_{lh22} \cdot \left(m_{lhw} \cdot E\right)^{\frac{1}{2}} \cdot L_w$$

$$f_{lh}(E) := \left(r_{lh1}(E) - \frac{1}{r_{lh1}(E)}\right) \cdot \sin\left(r_{lh2}(E)\right) - 2 \cdot \cos\left(r_{lh2}(E)\right)$$

$$E := 0.001, 0.002 .. \Delta E_{lhstr} - 0.001$$

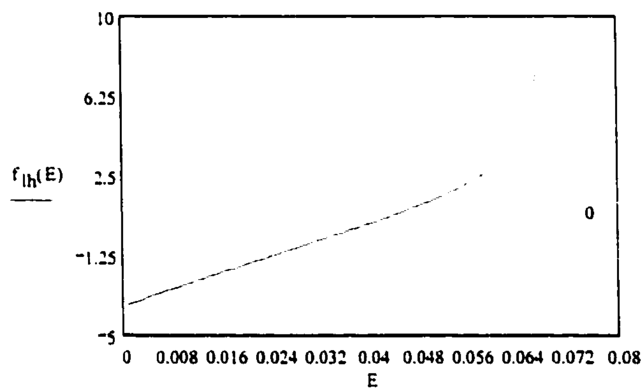

Npoint := 150

Nvar := 0 .. Npoint − 1

$$E_{lh_{Nvar}} := \frac{Nvar + 0.1}{Npoint} \cdot \Delta E_{lhstr}$$

$$y_{lh_{Nvar}} := f_{lh}\left(E_{lh_{Nvar}}\right) \qquad y_{lh_{Npoint}} := y_{lh_{Npoint-1}}$$

$$Nzer_0 := 0$$

$$Nzer_{Nvar+1} := \mathrm{if}\left(y_{lh_{Nvar}} \cdot y_{lh_{Nvar+1}} < 0, Nzer_{Nvar} + 1, Nzer_{Nvar}\right)$$

$$Nzer_{lh} := Nzer_{Npoint}$$

$Nzer_{lh}$ is the number of energy levels in light hole valence band.It may exceed three.

$N1 := 0 .. Nzer_{lh}$

$intervals_{N1} := -0.5 + N1$

$Nth := hist(intervals, Nzer)$

$Nth_0 := Nth_0 - 1$

Nth is the distribution of zero points

$Nthzero_0 := 0$

$N2 := 1 .. Nzer_{lh}$

$Nthzero_{N2} := Nthzero_{N2-1} + Nth_{N2-1}$

Nthzero is the order of points where function changes its sign

$N3 := 1 .. Nzer_{lh}$

$Ezer_{N3-1} := E_{lh\,Nthzero_{N3}}$

Ezer can be used for the initial values to find the solution

$N4 := 0$

$X := Ezer_{N4}$

$E_{lhzer_{N4}} := root(f_{lh}(X), X)$

$N4 := if(Nzer_{lh} - 2 \ge 0, 1, 0)$

$X := Ezer_{N4}$

$E_{lhzer_{N4}} := root(f_{lh}(X), X)$

$N4 := if(Nzer_{lh} - 3 \ge 0, 2, 0)$

$X := Ezer_{N4}$

$E_{lhzer_{N4}} := root(f_{lh}(X), X)$

$Nlevel_{lh} := length(E_{lhzer})$

$Nlevel_{lh} = 1$

$E_{lhzer} = 0.0374$

Now,we have obtained the ***light hole energy levels of valence band*** in ***E_{lhzer}*** and the ***number of the energy levels*** in ***$Nlevel_{lh}$***. Note that the ***maxium number*** we calculate is ***three.***

3) Heavy hole levels in valence band

Let us to calculate the heavy hole states in valence band neglecting the effects of band nonparabol

$$r_{hh1}(E) := \left(\frac{m_{hhb}}{m_{hhw}} \cdot \frac{E}{\Delta E_{hhstr} - E}\right)^{\frac{1}{2}}$$

In this calculation,we use the effective mass in $\cdot m_0$, E in eV and L_w in $\cdot 10^{-9}$m

$$r_{hh22} := \left(\frac{2 \cdot m_0 \cdot eV}{hbar^2}\right)^{\frac{1}{2}} \cdot 10^{-9} \qquad r_{hh22} = 5.1231$$

$$r_{hh2}(E) := r_{hh22} \cdot \left(m_{hhw} \cdot E\right)^{\frac{1}{2}} \cdot L_w$$

$$f_{hh}(E) := \left(r_{hh1}(E) - \frac{1}{r_{hh1}(E)}\right) \cdot \sin\left(r_{hh2}(E)\right) - 2 \cdot \cos\left(r_{hh2}(E)\right)$$

$$E := 0.001, 0.002 .. \Delta E_{hhstr} - 0.001$$

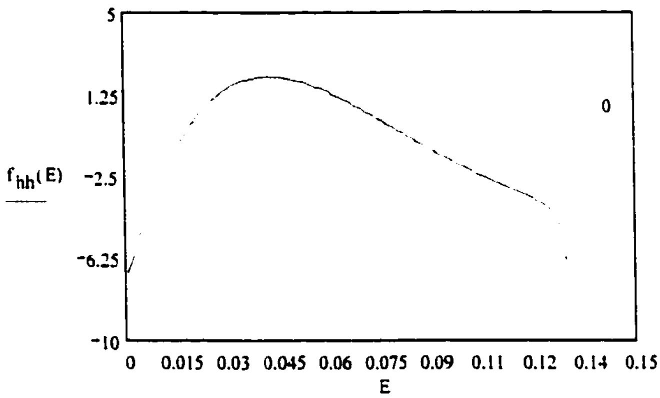

$$Npoint := 200$$

$$Nvar := 0 .. Npoint - 1$$

$$E_{hh_{Nvar}} := \frac{Nvar + 0.1}{Npoint} \cdot \Delta E_{hhstr}$$

$$y_{hh_{Nvar}} := f_{hh}\left(E_{hh_{Nvar}}\right) \qquad y_{hh_{Npoint}} := y_{hh_{Npoint-1}}$$

$$Nzer_0 := 0$$

$$Nzer_{Nvar+1} := \mathrm{if}\left(y_{hh_{Nvar}} \cdot y_{hh_{Nvar+1}} < 0, Nzer_{Nvar} + 1, Nzer_{Nvar}\right)$$

$$Nzer_{hh} := Nzer_{Npoint}$$

$$Nzer_{hh} = 2$$

$Nzer_{hh}$ is the number of energy levels in heavy hol valence band.It may exceed three.

$N1 := 0 .. Nzer_{hh}$

$intervals_{N1} := -0.5 + N1$

$Nth := hist(intervals, Nzer)$

$Nth_0 := Nth_0 - 1$ Nth is the distribution of zero points

$Nthzero_0 := 0$

$N2 := 1 .. Nzer_{hh}$

$Nthzero_{N2} := Nthzero_{N2-1} + Nth_{N2-1}$ Nthzero is the order of points where function changes its sign

$N3 := 1 .. Nzer_{hh}$

$Ezer_{N3-1} := E_{hh\,Nthzero_{N3}}$ Ezer can be used for the initial values to find the solution

$N4 := 0$

$X := Ezer_{N4}$

$E_{hhzer_{N4}} := root\left(f_{hh}(X), X\right)$

$N4 := if\left(Nzer_{hh} - 2 \geq 0, 1, 0\right)$

$X := Ezer_{N4}$

$E_{hhzer_{N4}} := root\left(f_{hh}(X), X\right)$

$N4 := if\left(Nzer_{hh} - 3 \geq 0, 2, 0\right)$

$X := Ezer_{N4}$

$E_{hhzer_{N4}} := root\left(f_{hh}(X), X\right)$

$Nlevel_{hh} := length\left(E_{hhzer}\right)$

$Nlevel_{hh} = 2$

$$E_{hhzer} = \begin{bmatrix} 0.0199 \\ 0.076 \end{bmatrix}$$

Now,we have obtained the ***heavy hole energy levels of valence band*** in $\underline{E_{hhzer}}$ and the ***number of the energy levels*** in $\underline{Nlevel_{hh.}}$ Note that the ***maxium number*** we calculate is ***three***

Part 4: **Results**

1) Band Diagram

$$VB_{lh}(x) := \Delta E_{lhstr}\cdot\Phi\left(x+\frac{L_w}{2}\right) - \Delta E_{lhstr}\cdot\Phi\left(x-\frac{L_w}{2}\right)$$

$$VB_{hh}(x) := \Delta E_{hhstr}\cdot\Phi\left(x+\frac{L_w}{2}\right) - \Delta E_{hhstr}\cdot\Phi\left(x-\frac{L_w}{2}\right)$$

$$CB(x) := E_{gb}\cdot\Phi(x+2\cdot L_w) - \Delta E_{cw}\cdot\Phi\left(x+\frac{L_w}{2}\right) + \Delta E_{cw}\cdot\Phi\left(x-\frac{L_w}{2}\right)$$

$$x := -L_w\cdot\frac{3}{2}, -L_w\cdot\frac{3}{2}+0.05 .. L_w\cdot\frac{3}{2} \qquad x1 := -L_w, -L_w\cdot 0.5 .. L_w$$

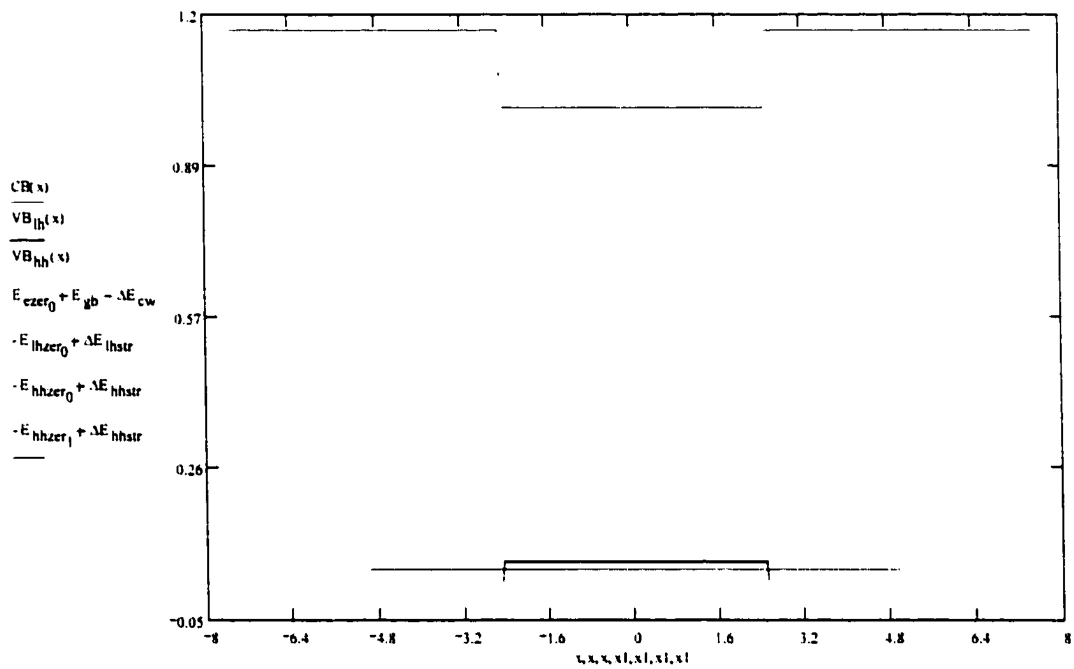

$E_{ezer_0} = 0.0701$ $\quad \Delta E_{cw} - E_{ezer_0} = 0.0901$ $\quad E_{e1hh1} := E_{cwstr} - E_{vwhh} + E_{ezer_0} + E_{hhzer_0}$ $\quad E_{e1hh1} = 0.96719$ $\quad \dfrac{1.23985}{E_{e1hh1}} = 1.2819$

$E_{hhzer_0} = 0.0199$ $\quad \Delta E_{hhstr} - E_{hhzer_0} = 0.1112$ $\quad E_{ezer_0} = 0.0701$ $\quad E_{hhzer_0} = 0.0199$

$E_{lhzer_0} = 0.0374$ $\quad \Delta E_{lhstr} - E_{lhzer_0} = 0.0317$ $\quad E_{e1lh1} := E_{cwstr} - E_{vwlh} + E_{ezer_0} + E_{lhzer_0}$ $\quad E_{e1lh1} = 1.0467$ $\quad \dfrac{1.23985}{E_{e1lh1}} = 1.1846$

$E_{hhzer_1} = 0.076$ $\quad \Delta E_{hhstr} - E_{hhzer_1} = 0.055$ $\quad E_{e1hh2} := E_{cwstr} - E_{vwhh} + E_{ezer_0} + E_{hhzer_1}$ $\quad E_{e1hh2} = 1.0234$ $\quad \dfrac{1.23985}{E_{e1hh2}} = 1.2116$

$E_{e1lh1} - E_{e1hh1} = 0.0795$

Part 5: Calculate Wavefunctions and overlap

$$A := \left(\frac{2\cdot m_0\cdot eV}{hbar^2}\right)^{\frac{1}{2}}\cdot 10^{-9}$$

$$k_{ew}(E) := A\cdot\left(m_{ew}\cdot E\right)^{\frac{1}{2}} \qquad k_{eb}(E) := A\cdot\left[m_{eb}\cdot\left(\Delta E_{cw} - E\right)\right]^{\frac{1}{2}}$$

$$k_{lhw}(E) := A\cdot\left(m_{lhw}\cdot E\right)^{\frac{1}{2}} \qquad k_{lhb}(E) := A\cdot\left[m_{lhb}\cdot\left(\Delta E_{lhstr} - E\right)\right]^{\frac{1}{2}}$$

$$k_{hhw}(E) := A\cdot\left(m_{hhw}\cdot E\right)^{\frac{1}{2}} \qquad k_{hhb}(E) := A\cdot\left[m_{hhb}\cdot\left(\Delta E_{hhstr} - E\right)\right]^{\frac{1}{2}}$$

1) electron wavefunctions

$$B_{el}(E) := \frac{\cos\left(k_{ew}(E)\cdot\frac{L_w}{2}\right)}{\exp\left(-k_{eb}(E)\cdot\frac{L_w}{2}\right)} \qquad C_{el}(E) := \frac{-\sin\left(k_{ew}(E)\cdot\frac{L_w}{2}\right)}{\exp\left(-k_{eb}(E)\cdot\frac{L_w}{2}\right)}$$

$$Y1_{el}(E,x) := \exp\left(k_{eb}(E)\cdot x\right)\cdot\Phi\left(-\frac{L_w}{2} - x\right)$$

$$Y2_{el}(E,x) := \cos\left(k_{ew}(E)\cdot x\right)\cdot\Phi\left(x + \frac{L_w}{2}\right)\cdot\Phi\left(\frac{L_w}{2} - x\right)$$

$$Y3_{el}(E,x) := \exp\left(-k_{eb}(E)\cdot x\right)\cdot\Phi\left(x - \frac{L_w}{2}\right)$$

$$\phi_{el}(E,x) := B_{el}(E)\cdot Y1_{el}(E,x) + Y2_{el}(E,x) + B_{el}(E)\cdot Y3_{el}(E,x)$$

$$CON(E) := \frac{B_{el}(E)^2}{k_{eb}(E)}\cdot\exp\left(-k_{eb}(E)\cdot L_w\right) + \frac{1}{2\cdot k_{ew}(E)}\cdot\sin\left(k_{ew}(E)\cdot L_w\right) + \frac{L_w}{2}$$

$$\phi1_{el}(x) := \frac{\phi_{el}\left(E_{ezer_0}, x\right)}{\sqrt{CON\left(E_{ezer_0}\right)}} \qquad \phi3_{el}(x) := -\frac{\phi_{el}\left(E_{ezer_0}, x\right)}{\sqrt{CON\left(E_{ezer_2}\right)}} \qquad x := -5\cdot L_w, -5\cdot L_w + 0.1 .. 5\cdot L_w$$

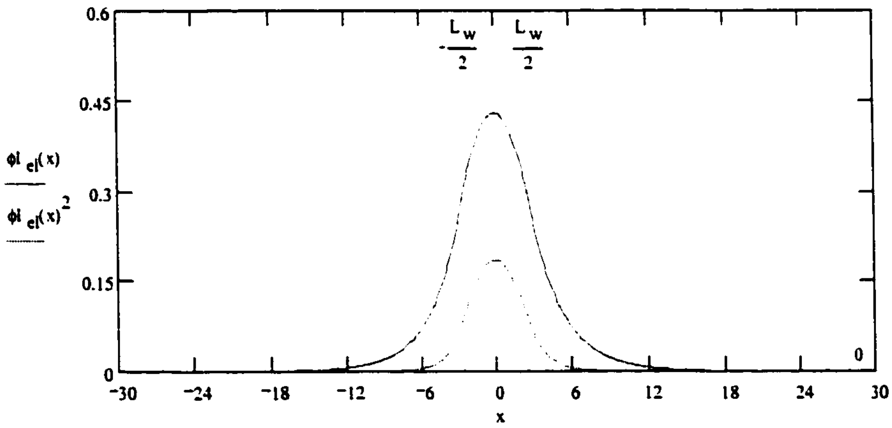

2) light hole wavefunction

$$B_{lh}(E) := \frac{\cos\left(k_{lhw}(E)\cdot\frac{L_w}{2}\right)}{\exp\left(-k_{lhb}(E)\cdot\frac{L_w}{2}\right)} \qquad C_{lh}(E) := \frac{-\sin\left(k_{lhw}(E)\cdot\frac{L_w}{2}\right)}{\exp\left(-k_{lhb}(E)\cdot\frac{L_w}{2}\right)}$$

$$Y1_{lh}(E,x) := \exp\left(k_{lhb}(E)\cdot x\right)\cdot\Phi\left(-\frac{L_w}{2} - x\right)$$

$$Y2_{lh}(E,x) := \cos\left(k_{lhw}(E)\cdot x\right)\cdot\Phi\left(x + \frac{L_w}{2}\right)\cdot\Phi\left(\frac{L_w}{2} - x\right)$$

$$Y3_{lh}(E,x) := \exp\left(-k_{lhb}(E)\cdot x\right)\cdot\Phi\left(x - \frac{L_w}{2}\right)$$

$$\phi_{lh}(E,x) := B_{lh}(E)\cdot Y1_{lh}(E,x) + Y2_{lh}(E,x) + B_{lh}(E)\cdot Y3_{lh}(E,x)$$

$$CON_{lh}(E) := \frac{B_{lh}(E)^2}{k_{lhb}(E)}\cdot\exp\left(-k_{lhb}(E)\cdot L_w\right) + \frac{1}{2\cdot k_{lhw}(E)}\cdot\sin\left(k_{lhw}(E)\cdot L_w\right) + \frac{L_w}{2}$$

$$\phi l_{lh}(x) := \frac{\phi_{lh}\left(E_{lhzero_0}, x\right)}{\sqrt{CON_{lh}\left(E_{lhzero_0}\right)}}$$

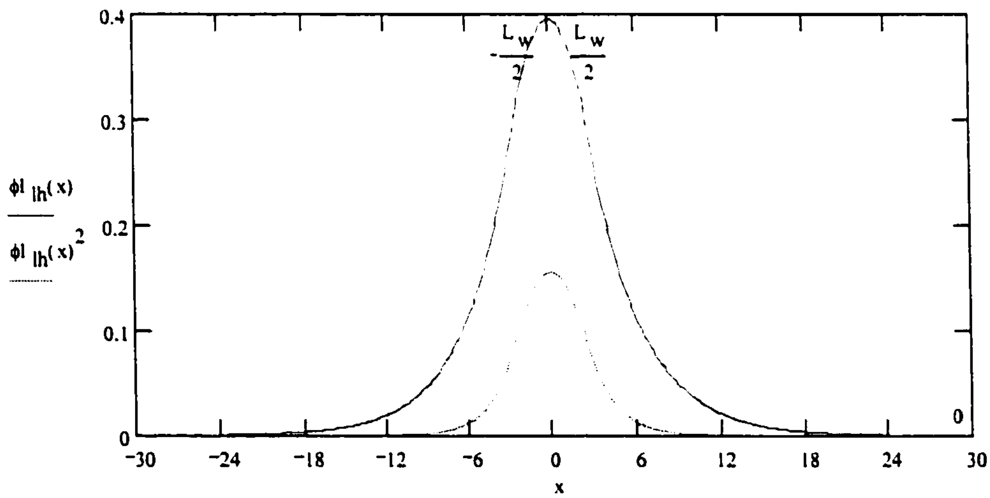

3) heavy hole wavefunctions

$$B_{hh}(E) := \frac{\cos\, k_{hhw}(E)\cdot\frac{L_w}{2}}{\exp\, -k_{hhb}(E)\cdot\frac{L_w}{2}} \qquad C_{hh}(E) := \frac{-\sin\, k_{hhw}(E)\cdot\frac{L_w}{2}}{\exp\, -k_{hhb}(E)\cdot\frac{L_w}{2}}$$

$$Y1_{hh}(E,x) := \exp\, k_{hhb}(E)\cdot x\, \cdot\Phi\, -\frac{L_w}{2} - x$$

$$Y2_{hh}(E,x) := \cos\, k_{hhw}(E)\cdot x\, \cdot\Phi\, x + \frac{L_w}{2}\, \cdot\Phi\, \frac{L_w}{2} - x$$

$$Y3_{hh}(E,x) := \exp\, -k_{hhb}(E)\cdot x\, \cdot\Phi\, x - \frac{L_w}{2}$$

$$\phi_{hh}(E,x) := B_{hh}(E)\cdot Y1_{hh}(E,x) + Y2_{hh}(E,x) + B_{hh}(E)\cdot Y3_{hh}(E,x)$$

$$CON_{hh}(E) := \frac{B_{hh}(E)^2}{k_{hhb}(E)}\cdot\exp\, -k_{hhb}(E)\cdot L_w\, + \frac{1}{2\cdot k_{hhw}(E)}\cdot\sin\, k_{hhw}(E)\cdot L_w\, + \frac{L_w}{2}$$

$$\phi 1_{hh}(x) := \frac{\phi_{hh}\, E_{hhzer_0}, x}{\sqrt{CON_{hh}\, E_{hhzer_0}}}$$

$$\phi 3_{hh}(x) := \frac{-\phi_{hh}\, E_{hhzer_2}, x}{\sqrt{CON_{hh}\, E_{hhzer_2}}}$$

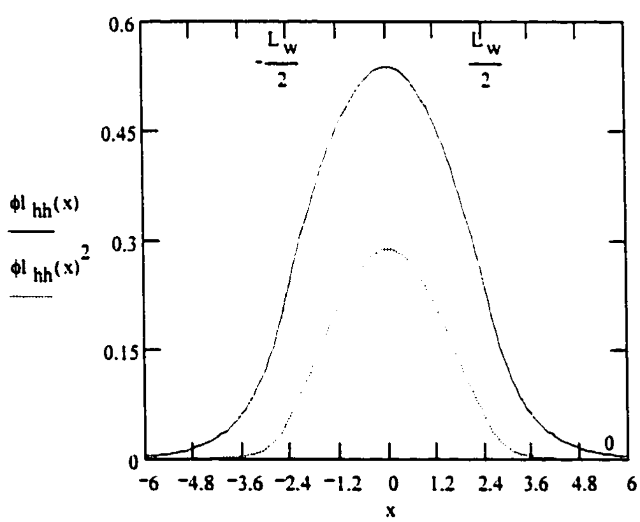

$$Y4_{hh}(E,x) := \sin\left(k_{hhw}(E)\cdot x\right)\cdot\Phi\left(x+\frac{L_w}{2}\right)\cdot\Phi\left(\frac{L_w}{2}-x\right)$$

$$\phi b_{hh}(E,x) := C_{hh}(E)\cdot Y1_{hh}(E,x) + Y4_{hh}(E,x) - C_{hh}(E)\cdot Y3_{hh}(E,x)$$

$$CON2_{hh}(E) := \frac{C_{hh}(E)^2}{k_{hhb}(E)}\cdot\exp\left(-k_{hhb}(E)\cdot L_w\right) - \frac{1}{2\cdot k_{hhw}(E)}\cdot\sin\left(k_{hhw}(E)\cdot L_w\right) + \frac{L_w}{2}$$

$$\phi 2_{hh}(x) := -\frac{\phi b_{hh}\left(E_{hhzero_1},x\right)}{\sqrt{CON2_{hh}\left(E_{hhzero_1}\right)}} \qquad \int_{-5\cdot L_w}^{5\cdot L_w}\overline{\phi 2_{hh}(x)}\cdot\phi 2_{hh}(x)\,dx = 1$$

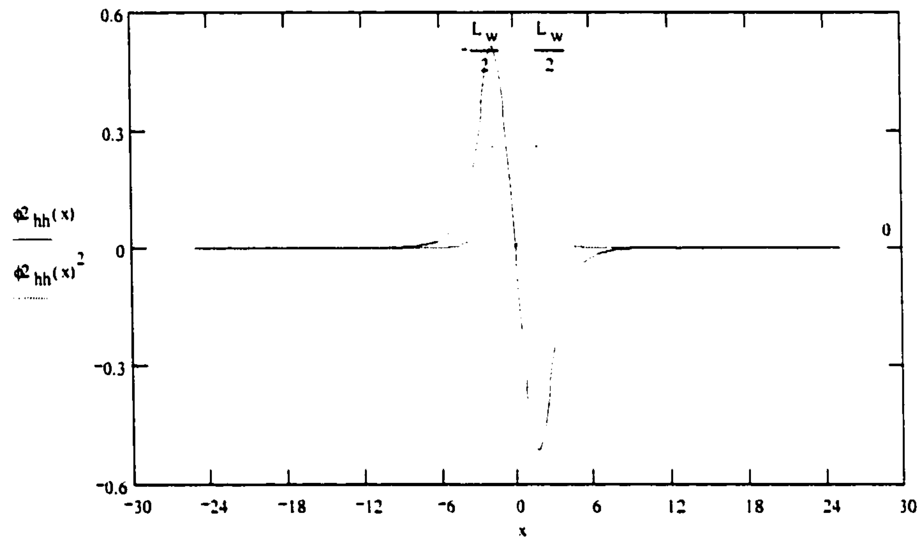

4) Calculate overlap Integrals

$$\int_{-5\cdot L_w}^{5\cdot L_w}\overline{\phi 1_{el}(x)}\cdot\phi 1_{hh}(x)\,dx = 0.9367$$

$$\int_{-5\cdot L_w}^{5\cdot L_w}\overline{\phi 1_{el}(x)}\cdot\phi 1_{lh}(x)\,dx = 0.9898$$

$$\int_{-5\cdot L_w}^{5\cdot L_w}\overline{\phi 1_{el}(x)}\cdot\phi 2_{hh}(x)\,dx = 0 \qquad \int_{-5\cdot L_w}^{5\cdot L_w}\overline{\phi 1_{el}(x)}\cdot\phi 3_{hh}(x)\,dx =$$

Part 5: Calculate Refractive Index of Layers

$q := 1.6\cdot10^{-19}$ $\quad hb := 1.05\cdot10^{-34}$ $\quad hbe := \frac{hb}{q}$ $\quad \Gamma := 0.0$

$\chi_0(\omega, E_g) := \frac{hbe\cdot\omega + i\cdot\Gamma}{E_g}$ $\qquad \chi_{so}(\omega, E_g, \Delta) := \frac{hbe\cdot\omega + i\cdot\Gamma}{E_g + \Delta}$

$f(\chi, \omega, E_g, \Delta) := \chi^{-2}\cdot\left[2 - (1+\chi)^{0.5} - (1-\chi)^{0.5}\cdot\Phi(1-\chi)\right]$

$A(y) := 8.40 - 3.40\cdot y$ $\qquad B(y) := 6.60 + 3.40\cdot y$

$$\eta(\omega, y, E_g, \Delta) := \left[A(y)\cdot\left[f(\chi_0(\omega, E_g), \omega, E_g, \Delta) + \frac{1}{2}\cdot\left(\frac{E_g}{E_g + \Delta}\right)^{1.5}\cdot f(\chi_{so}(\omega, E_g, \Delta), \omega, E_g, \Delta)\right] + B(y)\right]^{0.5}$$

$\omega := \frac{0.6}{hbe}, \frac{0.605}{hbe} .. \frac{1.0}{hbe}$

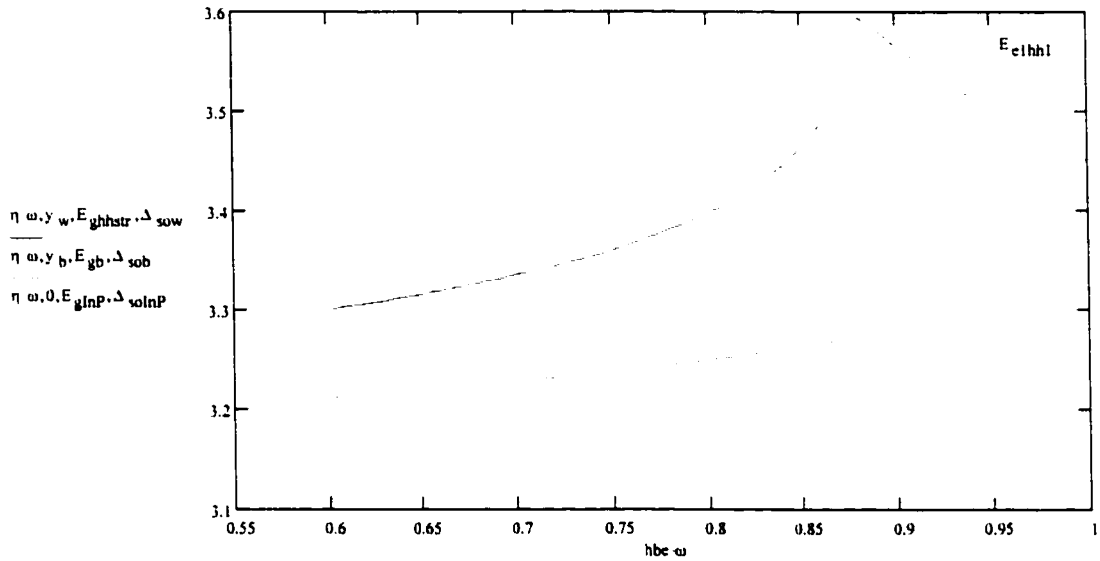

$E_{elhhl} = 0.9672$ $\qquad \frac{1.23985}{E_{elhhl}} = 1.2819$ $\qquad Et := \frac{1.23985}{1.3}$ $\qquad Et = 0.9537$

$\eta\left(\frac{E_{elhhl}}{hbe}, y_w, E_{ghhstr}, \Delta_{sow}\right) = 3.4824$

$\eta\left(\frac{E_{elhhl}}{hbe}, y_b, E_{gb}, \Delta_{sob}\right) = 3.3069$

$\eta\left(\frac{E_{elhhl}}{hbe}, 0, E_{gInP}, \Delta_{soInP}\right) = 3.206$

Appendix B – Spontaneous Emission Calculation

This program pikal\Spon_em\1015\F10\T10\ Sp4m6 calculates the Spontaneous Emission spectra from the InGaAsP MBE1015 laser using band structure from pikal\bandstruct\1015\T10c with T=283K

Physical constants

$\varepsilon_0 := 8.85\cdot 10^{-14}$ $c := 3\cdot 10^{10}$ $m_0 := 9.11\cdot 10^{-31}$ $q := 1.6\cdot 10^{-19}$ $kb := 1.38\cdot 10^{-23}$

$hb := 1.05\cdot 10^{-34}$ $h := hb\cdot 2\cdot \pi$ $hbe := \frac{hb}{q}$ $he := \frac{h}{q}$ $\Gamma_w := 0.05486$ $\Gamma_b := 0.4347$

Environmental Conditions:

$T := 283$

Laser Structure:

$N_w := 6$ Number of Wells

$L_w := 50\cdot 10^{-8}$ Well Width

$L_{sch} := 1100\cdot 10^{-8}$ SCH width

$L_b := 100\cdot 10^{-8}$ Barrier width

$W := 1.4\cdot 10^{-4}$ Laser active region width

$L := 475\cdot 10^{-4}$ Laser active region length

$L_{bsch} := 5\cdot L_b + 2\cdot L_{sch}$ $L_{bsch} = 2.7\cdot 10^{-5}$ Total Barrier and SCH width

$L_{wt} := N_w\cdot L_w$ $L_{wt} = 3\cdot 10^{-6}$ Total well width

$V_w := L\cdot W\cdot L_{wt}$ $V_w = 1.995\cdot 10^{-11}$ Total well volume

$V_b := L\cdot W\cdot L_b$ $V_b = 6.65\cdot 10^{-12}$ Total barrier volume

$V_{bsch} := L\cdot W\cdot L_{bsch}$ $V_{bsch} = 1.795\cdot 10^{-10}$ Total barrier and SCH volume

$\frac{V_{bsch}}{V_w} = 9$ Ratio of barrier and SCH volume to total well volun

$Ec := 0$ $Ev := 0$

$$f(E, Ef) := \frac{1}{e^{\frac{(E-Ef)\cdot q}{kb\cdot T}} + 1}$$

Fermi dirac statistics

Cladding (InP) Properties

$\Delta E_{e1c} := 0.0728 + 0.1133$ First confined level to cladding energy

$m_{ec} := 0.0761 \cdot m_0$ Cladding electron effective mass

$m_{hhc} := 0.4543 \cdot m_0$ Cladding heavy hole effective mass

$m_{lhc} := 0.1195 \cdot m_0$ Cladding light hole effective mass

$\Delta_c := 0.11$ $\eta_c := 3.2078$

$m_{rhhc} := \frac{m_{ec} \cdot m_{hhc}}{m_{ec} + m_{hhc}}$ Cladding reduced effective mass $\frac{m_{rhhc}}{m_0} = 0.065$

$N_{ec} := 2 \cdot \left(\frac{2 \cdot \pi \cdot m_{ec} \cdot kb \cdot T}{h^2}\right)^{\frac{3}{2}} \cdot \frac{1}{100^3}$ Cladding electron effective DOS $N_{ec} = 4.887 \cdot 10^{17}$

$n_c(Efn) := N_{ec} \cdot e^{\frac{q \cdot (Efn - \Delta E_{e1c})}{kb \cdot T}}$ Cladding electron density maxwell/boltzman

Barrier Properties

$E_{gb} := 1.1646 - 0.004$ Barrier band gap

$\Delta E_{elb} := 0.1133$ $\Delta E_{hhb} := 0.0833$ First confined level to barrier energy

$m_{eb} := 0.0695 \cdot m_0$ Barrier electron effective mass

$m_{hhb} := 0.4543 \cdot m_0$ Barrier heavy hole effective mass

$m_{lhb} := 0.0963 \cdot m_0$ Barrier light hole effective mass

$\Delta_b := 0.1863$ $\eta_b := 3.3095$

$$m_{rhhb} := \frac{m_{eb} \cdot m_{hhb}}{m_{eb} + m_{hhb}}$$ Barrier reduced effective mass $\frac{m_{rhhb}}{m_0} = 0.06$

$$M_{bb} := \sqrt{\left(\frac{m_0}{m_{eb}} - 1\right) \cdot \frac{m_0 \cdot E_{gb} \cdot q \cdot \left(E_{gb} + \Delta_b\right) \cdot q}{6 \cdot \left(E_{gb} + \frac{2}{3} \cdot \Delta_b\right) \cdot q}}$$ Barrier Matrix element $2 \cdot \frac{M_{bb}^2}{q \cdot m_0} = 5.43$

$$N_{eb} := 2 \cdot \left(\frac{2 \cdot \pi \cdot m_{eb} \cdot kb \cdot T}{h^2}\right)^{\frac{3}{2}} \cdot \frac{1}{100^3}$$ Barrier electron effective DOS $N_{eb} = 4.265 \cdot 10^{17}$

$$N_{hhb} := 2 \cdot \left(\frac{2 \cdot \pi \cdot m_{hhb} \cdot kb \cdot T}{h^2}\right)^{\frac{3}{2}} \cdot \frac{1}{100^3}$$ Barrier heavy hole effective DOS $N_{hhb} = 7.128 \cdot 10^{18}$

$$N_{lhb} := 2 \cdot \left(\frac{2 \cdot \pi \cdot m_{lhb} \cdot kb \cdot T}{h^2}\right)^{\frac{3}{2}} \cdot \frac{1}{100^3}$$ Barrier light hole effective DOS $N_{lhb} = 6.957 \cdot 10^{17}$

$$G_{eb}(E) := \frac{q \cdot m_{eb} \cdot \sqrt{2 \cdot m_{eb} \cdot E \cdot q}}{\pi^2 \cdot hb^3} \cdot \frac{1}{100^3}$$ Barrier electron DOS

$$N_{eb2} := \frac{q \cdot m_{eb} \cdot \sqrt{2 \cdot m_{eb} \cdot q}}{\pi^2 \cdot hb^3} \cdot \frac{1}{100^3}$$ Barrier electron DOS

$$n_b(Efn) := N_{eb} \cdot e^{\frac{q \cdot \left(Efn - \Delta E_{elb}\right)}{kb \cdot T}}$$ Barrier electron density maxwell/boltzman

$$n_{bi}(Efn) := \int_{Ec}^{Ec + 0.2} G_{eb}(E) \cdot f\left(E, Efn - \Delta E_{elb}\right) dE$$ Barrier electron density full integral

$$p_b(Efp) := N_{hhb} \cdot e^{\frac{q \cdot \left(Efp - \Delta E_{hhb}\right)}{kb \cdot T}}$$ Barrier heavy hole density maxwell/boltzman

Well Properties

$E_{ghhstr} := 0.8799$ Strained heavy hole energy gap

$E_{glhstr} := 0.9215$ Strained heavy hole energy gap

$E_{e1hh1} := 0.97575 - 0.016$ Electron to heavy hole 1 transition energy

$E_{e1lh1} := 1.0538 - 0.013$ Electron to light hole 1 transition energy

$E_{e1hh2} := 1.027$ Electron to heavy hole 2 transition energy

$m_{ew} := 0.051 \cdot m_0$ Well electron effective mass

$m_{hhw} := 0.128 \cdot m_0$ Well heavy hole DOS effective mass

$m_{lhw} := 0.1924 \cdot m_0$ Well light hole effective mass

$\Delta_w := 0.2369$ $\eta_w := 3.4767$

$\Delta lh := E_{e1lh1} - E_{e1hh1}$ Heavy hole to light hole split $\Delta lh = 0.0811$

$\Delta hh12 := E_{e1hh2} - E_{e1hh1}$ Heavy hole 1 to heavy hole 2 split $\Delta hh12 = 0.067$

$$m_{rhhw} := \frac{m_{ew} \cdot m_{hhw}}{m_{ew} + m_{hhw}}$$ Well heavy hole reduced effective mass $\frac{m_{rhhw}}{m_0} = 0.036$

$$m_{rlhw} := \frac{m_{ew} \cdot m_{lhw}}{m_{ew} + m_{lhw}}$$ Well light hole reduced effective mass $\frac{m_{rlhw}}{m_0} = 0.04$

$$M_{bhh} := \sqrt{\left(\frac{m_0}{m_{ew}} - 1\right) \cdot \frac{m_0 \cdot E_{ghhstr} \cdot q \cdot \left(E_{ghhstr} + \Delta_w\right) \cdot q}{6 \cdot \left(E_{ghhstr} + \frac{2}{3} \cdot \Delta_w\right) \cdot q}}$$ Well heavy hole Matrix element $2 \cdot \frac{M_{bhh}^2}{q \cdot m_0} = 5.873$

$over_{ehh1} := 0.9608$ $M_{thh} := over_{ehh1} \cdot M_{bhh}$

$$M_{blh} := \sqrt{\left(\frac{m_0}{m_{ew}} - 1\right) \cdot \frac{m_0 \cdot E_{glhstr} \cdot q \cdot \left(E_{glhstr} + \Delta_w\right) \cdot q}{6 \cdot \left(E_{glhstr} + \frac{2}{3} \cdot \Delta_w\right) \cdot q}}$$ Well Light hole Matrix element $2 \cdot \frac{M_{blh}^2}{q \cdot m_0} = 6.134$

$over_{elh1} := 0.8448$ $M_{tlh} := over_{elh1} \cdot M_{blh}$

$$N_{ew} := \frac{m_{ew} \cdot kb \cdot T}{\pi \cdot hb^2} \cdot \frac{1}{100^2}$$ Well electron effective DOS $N_{ew} = 5.239 \cdot 10^{11}$

$$N_{hhw} := \frac{m_{hhw} \cdot kb \cdot T}{\pi \cdot hb^2} \cdot \frac{1}{100^2}$$ Well heavy hole effective DOS $N_{hhw} = 1.315 \cdot 10^{12}$

$$N_{lhw} := \frac{m_{lhw} \cdot kb \cdot T}{\pi \cdot hb^2} \cdot \frac{1}{100^2}$$ Well light hole effective DOS $N_{lhw} = 1.976 \cdot 10^{12}$

$i := 0..600 \quad k := 100..500 \quad \Delta E := 1.05\cdot10^{-3} \quad Ed_i := E_{e1hh1} - 0.1783 + i\cdot\Delta E$

$\frac{1.23985}{Ed_{500,0}} = 0.949 \quad \frac{1.23985}{Ed_{100,0}} = 1.3987$

$\frac{1.23985}{Ed_{600,0}} = 0.8784 \quad \frac{1.23985}{Ed_{0,0}} = 1.5866$

$\frac{\frac{m_{rhhw}}{m_0}\cdot 13.5}{\eta_w^4} = 3.37\cdot10^{-3} \quad E_b := 0.003 \quad \Delta(E) := \frac{\pi}{\sqrt{\frac{(E+0.0000003)}{E_b}}}$

$$LOR(E,\tau) := \frac{1}{\pi}\left[\frac{\frac{hbe}{\tau}}{\left(\frac{hbe}{\tau}\right)^2 + (E)^2}\right] \qquad HSEC(E,\tau) := \frac{1}{\pi\cdot\frac{hbe}{\tau}}\cdot \mathrm{sech}\left(\frac{E}{\frac{hbe}{\tau}}\right) \qquad GAU(E,\tau) := \int_{E-0.2}^{E+0.2} \frac{1}{\sqrt{2\cdot\pi}\cdot\frac{hbe}{\tau}}\cdot e^{-\frac{(E21-E)^2}{2\cdot\left(\frac{hbe}{\tau}\right)^2}}\cdot\Phi(E21)\,dE21$$

$EL := -300..300 \quad EH := -200..200$

$$LDOS2D(E,\tau) := \sum_{EL}\frac{1}{\pi}\cdot\left[\frac{\frac{hbe}{\tau}}{\left(\frac{hbe}{\tau}\right)^2 + \left(\frac{EL}{1000}\right)^2}\right]\cdot\Phi\left(E+\frac{EL}{1000}\right)\cdot\Delta E \qquad LDOS3D(E,\tau) := \sum_{EL}\frac{\sqrt{E+\frac{EL}{1000}}}{\pi}\cdot\left[\frac{\frac{hbe}{\tau}}{\left(\frac{hbe}{\tau}\right)^2 + \left(\frac{EL}{1000}\right)^2}\right]\cdot\Phi\left(E+\frac{EL}{1000}\right)\cdot\Delta E$$

$$LC2D(E,\tau) := \sum_{EL}\frac{1}{\pi}\cdot\left[\frac{\frac{hbe}{\tau}}{\left(\frac{hbe}{\tau}\right)^2 + \left(\frac{EL}{1000}\right)^2}\right]\cdot\Phi\left(E+\frac{EL}{1000}\right)\cdot\frac{e^{\Delta\left(E+\frac{EL}{1000}\right)}}{\cosh\left(\Delta\left(E+\frac{EL}{1000}\right)\right)}\cdot\Delta E$$

$$LC3D(E,\tau) := \sum_{EL}\frac{\sqrt{E+\frac{EL}{1000}}}{\pi}\cdot\left[\frac{\frac{hbe}{\tau}}{\left(\frac{hbe}{\tau}\right)^2 + \left(\frac{EL}{1000}\right)^2}\right]\cdot\Phi\left(E+\frac{EL}{1000}\right)\cdot\frac{\Delta\left(E+\frac{EL}{1000}\right)\cdot e^{\Delta\left(E+\frac{EL}{1000}\right)}}{\sinh\left(\Delta\left(E+\frac{EL}{1000}\right)\right)}\cdot\Delta E$$

$$HDOS2D(E,\tau) := \sum_{EH}\frac{1}{\pi\cdot\frac{hbe}{\tau}}\cdot\mathrm{sech}\left[\frac{\frac{EH}{1000}}{\frac{hbe}{\tau}}\right]\cdot\Phi\left(E+\frac{EH}{1000}\right)\cdot\Delta E \qquad HDOS3D(E,\tau) := \sum_{EH}\frac{\sqrt{E+\frac{EH}{1000}}}{\pi\cdot\frac{hbe}{\tau}}\cdot\mathrm{sech}\left[\frac{\frac{EH}{1000}}{\frac{hbe}{\tau}}\right]\cdot\Phi\left(E+\frac{EH}{1000}\right)\cdot\Delta E$$

$$HC2D(E,\tau,x) := \sum_{EH}\frac{1}{\pi\cdot\frac{hbe}{\tau}}\cdot\mathrm{sech}\left[\frac{\frac{EH}{1000}}{\frac{hbe}{\tau}}\right]\cdot\Phi\left(E+\frac{EH}{1000}\right)\cdot\left[\frac{x\cdot e^{\Delta\left(E+\frac{EH}{1000}\right)}}{\cosh\left(\Delta\left(E+\frac{EH}{1000}\right)\right)} + (1-x)\right]\cdot\Delta E$$

$$HC3D(E,\tau) := \sum_{EH}\frac{\sqrt{E+\frac{EH}{1000}}}{\pi\cdot\frac{hbe}{\tau}}\cdot\mathrm{sech}\left[\frac{\frac{EH}{1000}}{\frac{hbe}{\tau}}\right]\cdot\Phi\left(E+\frac{EH}{1000}\right)\cdot\frac{\Delta\left(E+\frac{EH}{1000}\right)\cdot e^{\Delta\left(E+\frac{EH}{1000}\right)}}{\sinh\left(\Delta\left(E+\frac{EH}{1000}\right)\right)}\cdot\Delta E$$

$E := -0.10, -0.09 .. 0.2$ $\tau_{hhdosh} := 0.09 \cdot 10^{-12}$ $\tau_{bdos} := 0.08 \cdot 10^{-12}$ $\tau_{lhdosh} := 0.1 \cdot 10^{-12}$

$\tau_{hhdosl} := 2 \cdot \tau_{hhdosh}$ $\tau_{bdosl} := 2 \cdot \tau_{bdos}$ $\tau_{lhdosl} := 2 \cdot \tau_{lhdosh}$

$x_{hh} := 0.04$ $x_b := 0.0$ $x_{lh} := 0.04$

$$n_{we}(Efn, E) := \frac{N_{ew} \cdot q}{kb \cdot T} \cdot f(E, Efn) \cdot \left[\left(1 - x_{hh}\right) \cdot HDOS2D\left(E, \tau_{hhdosh}\right) + x_{hh} \cdot LDOS2D\left(E, \tau_{hhdosl}\right) \right]$$

Well electron density

$$n_{be}(Efn, E) := N_{eb2} \cdot f\left(E, Efn - \Delta E_{elb}\right) \cdot HDOS3D\left(E, \tau_{bdos}\right)$$

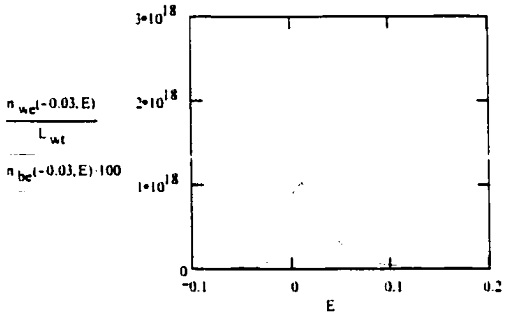

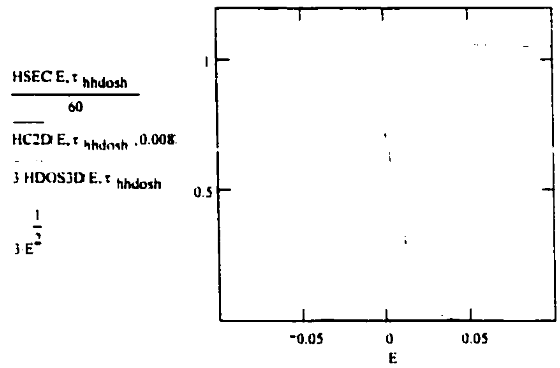

$$n_w(Efn) := \frac{N_{ew} \cdot q}{kb \cdot T} \cdot \int_{-0.2}^{0.2} f(E, Efn) \cdot \left[\left(1 - x_{hh}\right) \cdot HDOS2D\left(E, \tau_{hhdosh}\right) + x_{hh} \cdot LDOS2D\left(E, \tau_{hhdosl}\right) \right] dE$$

$$n_{bi}(Efn) := N_{eb2} \cdot \int_{-0.2}^{0.2} f\left(E, Efn - \Delta E_{elb}\right) \cdot HDOS3D\left(E, \tau_{bdos}\right) dE$$

Barrier electron density full integral

$Efn2 := -0.15, -0.14 .. 0.1$

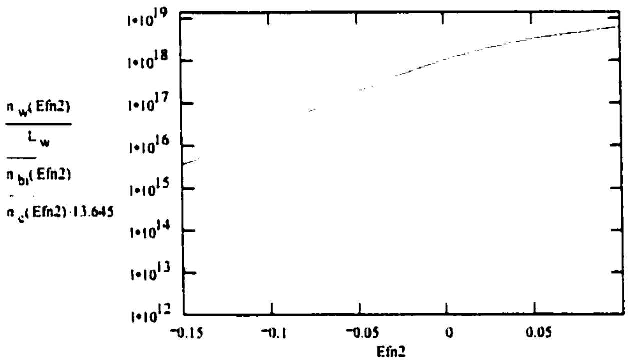

$$p_{hh}(Efp) := N_{hhw} \cdot \ln\left(e^{\frac{q \cdot Efp}{kb \cdot T}} + 1\right)$$

Well heavy hole 1 density

$$p_{hh2}(Efp) := N_{hhw} \cdot \ln\left[e^{\frac{q \cdot (Efp - \Delta hh12)}{kb \cdot T}} + 1 \right]$$

Well heavy hole 2 density

$$p_{lh}(Efp) := N_{lhw} \cdot \ln\left[e^{\frac{q \cdot (Efp - \Delta lh)}{kb \cdot T}} + 1 \right]$$

Well light hole density

Calculate fermi levels and carrier densities $Efp := -0.025$

$p_w(Efp) := p_{hh}(Efp) + p_{lh}(Efp) + p_{hh2}(Efp)$

Total density of well holes $\frac{p_w(Efp)}{L_w} = 9.171 \cdot 10^{17}$

$Pt(Efp) := V_w \cdot \frac{p_w(Efp)}{L_w} + V_{bsch} \cdot p_b(Efp)$

Total number of holes $Pt(Efp) = 3.344 \cdot 10^{7}$

$N(Efn) := V_w \cdot \frac{n_w(Efn)}{L_w} + V_{bsch} \cdot n_{bi}(Efn)$

Total number of electrons

$Efn := 0.02$ $Efn := root(log(N(Efn)) - log(Pt(Efp)), Efn)$

Calculate electon fermi level assuming number of electrons is equal to the number of holes

$N := V_w \frac{n_w(Efn)}{L_w} + V_{bsch} \cdot n_{bi}(Efn)$

Array containg total number of electrons $N = 3.344 \cdot 10^{7}$

$\Delta Ef := E_{e1hh1} + Efn + Efp$

Array containg fermi level separation $\Delta Ef = 0.9613$

$n_{bn} := n_{bi}(Efn)$

Array containg total number of barrier/SCH electrons $\frac{1.23985}{\Delta Ef} = 1.2898$

$n_{wn} := n_w(Efn)$ $E_{e1hh1} = 0.9597$

Array containg total number of well electrons $Efn = 0.02655$

Calculate various quanties at the maximum fermi level

$Efp = -0.025$ Electron fermi level

$Efn = 0.0265$ Hole fermi level

$\frac{n_{wn}}{L_w} = 1.545 \cdot 10^{18}$ $\frac{p_{hh}(Efp)}{L_w} = 8.068 \cdot 10^{17}$ Well and barrier electron density

$n_{bn} = 1.458 \cdot 10^{16}$ $p_b(Efp) = 8.434 \cdot 10^{16}$

$\frac{N}{V_w} = 1.676 \cdot 10^{18}$ $\frac{Pt(Efp)}{V_w} = 1.676 \cdot 10^{18}$ Total Electron and hole density assuming all in well

$\frac{V_w}{L_w} \cdot n_w(Efn) = 3.082 \cdot 10^{7}$ $p_{hh}(Efp) \cdot \frac{V_w}{L_w} = 1.61 \cdot 10^{7}$ Well electron and heavy hole numbers

$V_{bsch} \cdot n_{bn} = 2.617 \cdot 10^{6}$ $V_{bsch} \cdot p_b(Efp) = 1.514 \cdot 10^{7}$ Barrier electron and hole numbers

$\frac{V_{bsch} \cdot n_{bn}}{\frac{V_w}{L_w} \cdot n_{wn}} = 0.085$ Ratio of barrier to well electrons (Rdc)

$\frac{n_w(Efn)}{p_{hh}(Efp)} = 1.915$ Ratio of well electrons to heavy holes

$n_c(Efn) = 7.082 \cdot 10^{14}$

Calculate Spontaneous Emission Spectra including sech broadening and band-gap renormanlization

$$\Delta E_g := \frac{16\cdot 10^{-3}}{10^{18\frac{1}{3}}}\cdot\left(\frac{n_{wn}}{L_w}\right)^{\frac{1}{3}} \qquad \Delta E_g = 0.0185 \qquad x_{ex} := 0.0 \qquad \tau_{ex} := 0.07\cdot 10^{-12}$$

$$A2hh := \left[\frac{16\cdot\pi^2\cdot\eta_w\cdot q^2\cdot m_{rhhw}\cdot\left(M_{thh}\right)^2}{\varepsilon_0\cdot m_0^2\cdot c^3\cdot h^4\cdot L_w}\right]\cdot q\cdot V_w \qquad A2hh = 3.135\cdot 10^{36}$$

$$R2hh_i := A2hh\cdot Ed_i\cdot f\left[\frac{m_{rhhw}}{m_{ew}}\cdot\left(Ed_i - E_{e1hh1}\right), Efn\right]\cdot f\left[\frac{m_{rhhw}}{m_{hhw}}\cdot\left(Ed_i - E_{e1hh1}\right), Efp\right]\cdot\left[\begin{array}{l}(1 - x_{ex})\cdot\left[\begin{array}{l}(1 - x_{hh})\cdot HC2D\left(Ed_i - E_{e1hh1}, \tau_{hhdosh}, x_{ex}\right) \ldots \\ + x_{hh}\cdot LDOS2D\left(Ed_i - E_{e1hh1}, \tau_{hhdosl}\right)\end{array}\right] \ldots \\ + \dfrac{3\cdot x_{ex}\cdot 4\cdot E_b}{HSEC\left(0, \tau_{ex}\right)\cdot \operatorname{acosh}(2)\cdot\dfrac{2\cdot hbe}{\tau_{ex}}}\cdot HSEC\left(Ed_i - E_{e1hh1}, \tau_{ex}\right)\end{array}\right]$$

$$C2hh := \frac{q^2\cdot m_{rhhw}\cdot\left(M_{thh}\right)^2}{\varepsilon_0\cdot m_0^2\cdot c\cdot hb\cdot\eta_w\cdot L_w}\cdot\frac{1}{q} \qquad C2hh = 5.222\cdot 10^3$$

$$\alpha 2hh_i := \frac{C2hh}{Ed_i}\left[1 - f\left[\frac{m_{rhhw}}{m_{ew}}\cdot\left(Ed_i - E_{e1hh1}\right), Efn\right] - f\left[\frac{m_{rhhw}}{m_{hhw}}\cdot\left(Ed_i - E_{e1hh1}\right), Efp\right]\right]\cdot\left[\begin{array}{l}(1 - x_{hh})\cdot HC2D\left(Ed_i - E_{e1hh1}, \tau_{hhdosh}, x_{ex}\right) \ldots \\ + x_{hh}\cdot LDOS2D\left(Ed_i - E_{e1hh1}, \tau_{hhdosl}\right)\end{array}\right]$$

$$\tau_{hh} := 0.11\cdot 10^{-12} \qquad SPhh_k := \sum_{g = k - 100}^{k + 100} R2hh_g\cdot\frac{1}{\pi\cdot\dfrac{hbe}{\tau_{hh}}}\cdot \operatorname{sech}\left[\frac{Ed_k - Ed_g}{\dfrac{hbe}{\tau_{hh}}}\right]\cdot\Delta E \qquad B\alpha 2hh_k := \sum_{g = k - 100}^{k + 100} \alpha 2hh_g\cdot\frac{1}{\pi\cdot\dfrac{hbe}{\tau_{hh}}}\cdot \operatorname{sech}\left[\frac{Ed_k - Ed_g}{\dfrac{hbe}{\tau_{hh}}}\right]\cdot\Delta E$$

$$lh := 0.3$$

$$A2lh := \left[\frac{16\cdot\pi^2\cdot\eta_w\cdot q^2\cdot m_{rlhw}\cdot\left(M_{tlh}\right)^2}{\varepsilon_0\cdot m_0^2\cdot c^3\cdot h^4\cdot L_w}\right]\cdot q\cdot V_w\cdot lh \qquad A2lh = 8.395\cdot 10^{35}$$

$$R2lh_i := A2lh\cdot Ed_i\cdot f\left[\frac{m_{rlhw}}{m_{ew}}\cdot\left(Ed_i - E_{e1hh1}\right), Efn\right]\cdot f\left[\frac{m_{rlhw}}{m_{lhw}}\cdot\left(Ed_i - E_{e1hh1}\right), Efp\right]\cdot\left[\begin{array}{l}(1 - x_{lh})\cdot HC2D\left(Ed_i - E_{e1lh1}, \tau_{lhdosh}, 0\right) \ldots \\ + x_{lh}\left(LDOS2D\left(Ed_i - E_{e1lh1}, \tau_{lhdosl}\right)\right)\end{array}\right]$$

$$C2lh := \frac{q^2\cdot m_{rlhw}\cdot\left(M_{tlh}\right)^2}{\varepsilon_0\cdot m_0^2\cdot c\cdot hb\cdot\eta_w\cdot L_w}\cdot\frac{1}{q} \qquad C2lh = 4.661\cdot 10^3$$

$$\alpha 2lh_i := \frac{C2lh}{Ed_i}\left[1 - f\left[\frac{m_{rlhw}}{m_{ew}}\cdot\left(Ed_i - E_{e1hh1}\right), Efn\right] - f\left[\frac{m_{rlhw}}{m_{lhw}}\cdot\left(Ed_i - E_{e1hh1}\right), Efp\right]\right]\cdot\left[\begin{array}{l}(1 - x_{lh})\cdot HC2D\left(Ed_i - E_{e1lh1}, \tau_{lhdosh}, 0\right) \ldots \\ + x_{lh}\left(LDOS2D\left(Ed_i - E_{e1lh1}, \tau_{lhdosl}\right)\right)\end{array}\right]$$

$$\tau_{lh} := 0.036\cdot 10^{-12} \qquad SPlh_k := \sum_{g = k - 100}^{k + 100} R2lh_g\cdot\frac{1}{\pi\cdot\dfrac{hbe}{\tau_{lh}}}\cdot \operatorname{sech}\left[\frac{Ed_k - Ed_g}{\dfrac{hbe}{\tau_{lh}}}\right]\cdot\Delta E$$

$$A3b := \left[\frac{2\cdot\eta_b\cdot q^2\cdot M_{bb}^{\;2}}{\pi\cdot\varepsilon_0\cdot m_0^{\;2}\cdot c^3\cdot h^2}\cdot\frac{2\cdot m_{rhhb}}{hb^2}\right]^{\frac{3}{2}}\cdot\frac{q^{\frac{3}{2}}}{100}\cdot V_{bsch}\cdot b$$

$b := 1.31$

$A3b = 1.17\cdot 10^{38}$

$$R3b_i := A3b\cdot Ed_i\cdot f\left[\frac{m_{rhhb}}{m_{eb}}\cdot\left(Ed_i - E_{e1hh1}\right), Efn\right]\cdot f\left[\frac{m_{rhhb}}{m_{hhb}}\cdot\left(Ed_i - E_{e1hh1}\right), Efp\right]\cdot HDOS3D\left(Ed_i - E_{gb}, \tau_{bdos}\right)$$

$$C3b := \left[\frac{q^2\cdot h\cdot M_{bb}^{\;2}}{4\cdot\pi^2\cdot\varepsilon_0\cdot m_0^{\;2}\cdot c\cdot\eta_b}\cdot\frac{2\cdot m_{rhhb}}{hb^2}\right]^{\frac{3}{2}}\cdot\frac{b}{100\cdot q^{\frac{1}{2}}}$$

$C3b = 2.391\cdot 10^4$

$$\alpha 3b_i := \frac{C3b}{Ed_i}\cdot\left[1 - f\left[\frac{m_{rhhb}}{m_{eb}}\cdot\left(Ed_i - E_{e1hh1}\right), Efn\right] - f\left[\frac{m_{rhhb}}{m_{hhb}}\cdot\left(Ed_i - E_{e1hh1}\right), Efp\right]\right]\cdot HDOS3D\left(Ed_i - E_{gb}, \tau_{bdos}\right)$$

$\tau_b := 0.08\cdot 10^{-12}$

$$SPB_k := \sum_{g=k-100}^{k+100} R3b_g\cdot\frac{1}{\pi\cdot\frac{hbe}{\tau_b}}\cdot\mathrm{sech}\left[\frac{Ed_k - Ed_g}{\frac{hbe}{\tau_b}}\right]\cdot\Delta E$$

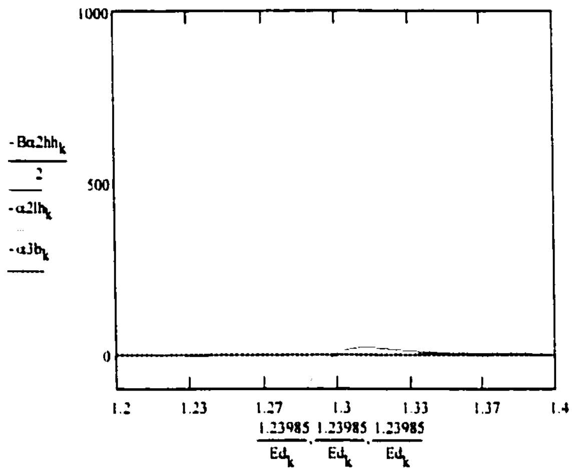

$$\frac{\max(-B\alpha 2hh)}{2} = 20.224$$

$$\Delta M := \frac{12398.5}{13000} - \frac{12398.5}{13007.56}$$

$\Delta M = 5.543\cdot 10^{-4}$

$$TM_k := \left[\frac{2}{3}\cdot\int_0^W \frac{SPlh_k}{W}\cdot e^{-\left(\frac{0}{2}\cdot\Gamma_w\cdot\alpha 2hh_k + \frac{2}{3}\cdot\Gamma_w\cdot\alpha 2lh_k + \frac{1}{3}\cdot\Gamma_b\cdot\alpha 3b_k\right)\cdot x}\,dx \ldots\right.$$
$$\left. + \frac{1}{3}\cdot\int_0^W \frac{SPB_k}{W}\cdot e^{-\left(\frac{0}{2}\cdot\Gamma_w\cdot\alpha 2hh_k + \frac{2}{3}\cdot\Gamma_w\cdot\alpha 2lh_k + \frac{1}{3}\cdot\Gamma_b\cdot\alpha 3b_k\right)\cdot x}\,dx\right]\cdot Ed_k\cdot q\cdot\Delta M\cdot q\cdot 0.9\cdot 10^9$$

$$UnP_k := \left[\frac{1}{2}\cdot\int_0^W \frac{SPhh_k}{W}\cdot e^{-\left(\frac{1}{2}\cdot\Gamma_w\cdot\alpha2hh_k+\frac{1}{6}\cdot\Gamma_w\cdot\alpha2lh_k+\frac{1}{3}\cdot\Gamma_b\cdot\alpha3b_k\right)\cdot x}\,dx \ldots \right.$$
$$+\frac{2}{3}\cdot\int_0^W \frac{SPlh_k}{W}\cdot e^{-\left(\frac{0}{2}\cdot\Gamma_w\cdot\alpha2hh_k+\frac{2}{3}\cdot\Gamma_w\cdot\alpha2lh_k+\frac{1}{3}\cdot\Gamma_b\cdot\alpha3b_k\right)\cdot x}\,dx \ldots$$
$$+\frac{1}{6}\cdot\int_0^W \frac{SPlh_k}{W}\cdot e^{-\left(\frac{1}{2}\cdot\Gamma_w\cdot\alpha2hh_k+\frac{1}{6}\cdot\Gamma_w\cdot\alpha2lh_k+\frac{1}{3}\cdot\Gamma_b\cdot\alpha3b_k\right)\cdot x}\,dx \ldots$$
$$+\frac{1}{3}\cdot\int_0^W \frac{SPB_k}{W}\cdot e^{-\left(\frac{0}{2}\cdot\Gamma_w\cdot\alpha2hh_k+\frac{2}{3}\cdot\Gamma_w\cdot\alpha2lh_k+\frac{1}{3}\cdot\Gamma_b\cdot\alpha3b_k\right)\cdot x}\,dx \ldots$$
$$\left.+\frac{1}{3}\cdot\int_0^W \frac{SPB_k}{W}\cdot e^{-\left(\frac{1}{2}\cdot\Gamma_w\cdot\alpha2hh_k+\frac{2}{3}\cdot\Gamma_w\cdot\alpha2lh_k+\frac{1}{3}\cdot\Gamma_b\cdot\alpha3b_k\right)\cdot x}\,dx\right]\cdot Ed_k\cdot q\cdot\Delta M\cdot q\cdot 0.9\cdot 10^9$$

MSP := READPRN("14A.dat") $\quad$ rmeas := rows(MSP) $\quad$ rmeas = 443 $\quad$ l := 0 .. rmeas − 2

CAL := READPRN("UnPolCal.dat") $\quad CalSP_l := \frac{MSP_{l,1}}{CAL_l}$ $\quad max_{meas} := \max(CalSP)$ $\quad \Delta E = 1.05\cdot 10^{-3}$

MTM := READPRN("TM4A.dat") $\quad$ tmeas := rows(MTM) $\quad$ tmeas = 443 $\quad$ t := 0 .. tmeas − 2 $\quad \alpha = \frac{max_{meas}}{\max(UnP)}$

TMCAL := READPRN("TMCal.dat") $\quad CalTM_l := \frac{MTM_{l,1}}{TMCAL_l}$ $\quad tmax_{meas} := \max(CalTM)$ $\quad \alpha = 3.065\cdot 10^{-4}$

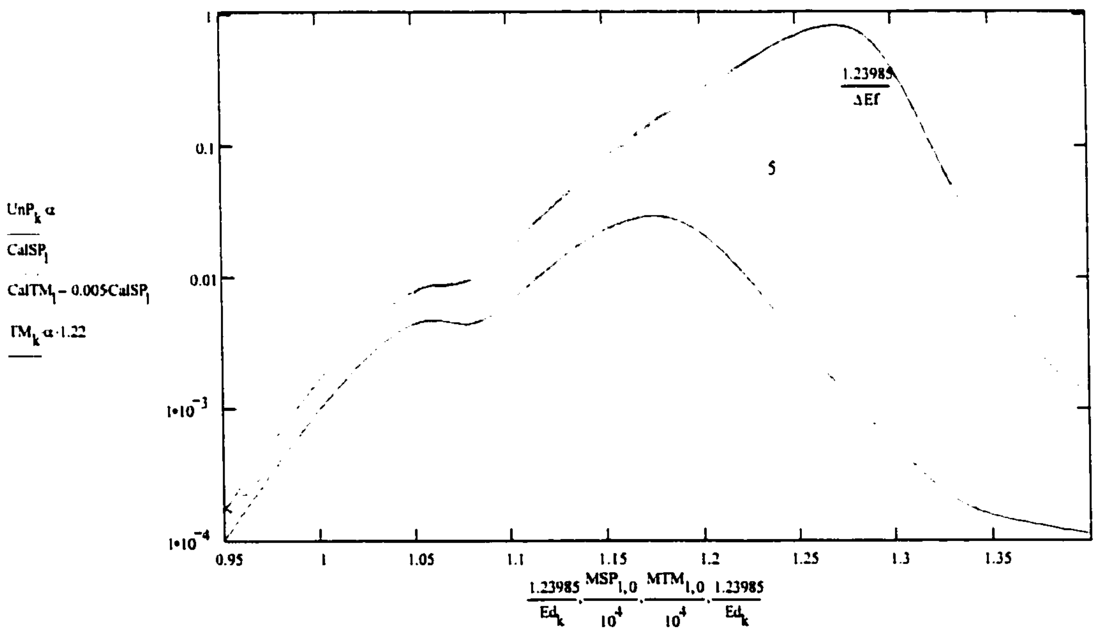

$ISPhh := \sum_k SPhh_k \cdot \Delta E \cdot q \qquad ISPlh := \sum_k SPlh_k \cdot \Delta E \cdot q \qquad ISPB := \sum_k SPB_k \cdot \Delta E \cdot q$

$ISPhh = 4.543 \cdot 10^{15} \qquad ISPB = 2.334 \cdot 10^{13} \qquad \frac{ISPB}{ISPhh} \cdot 100 = 0.5138$

$\frac{ISPhh}{V_w \cdot \frac{n_{wn}}{L_w} \cdot \frac{p_{hh}(Efp)}{L_w}} = 1.827 \cdot 10^{-10} \qquad \frac{ISPB}{V_{bsch} \cdot p_b(Efp) \cdot n_{bn}} = 1.058 \cdot 10^{-10} \qquad V_w = 1.995 \cdot 10^{-11}$

$\frac{ISPhh}{V_w \cdot \left(\frac{n_{wn}}{L_w}\right)^2} = 9.543 \cdot 10^{-11} \qquad \frac{ISPB}{V_{bsch} \cdot n_{bn}^2} = 6.12 \cdot 10^{-10} \qquad V_{bsch} = 1.795 \cdot 10^{-10}$

$\tau_n := \frac{1}{4.0 \cdot 10^7 + 1.0 \cdot 10^{-10} \cdot 1.0 \cdot 10^{18}} \qquad \tau_n = 7.143 \cdot 10^{-9} \qquad n_{bn} = 1.458 \cdot 10^{16}$

$n_c(Efn) = 7.082 \cdot 10^{14}$

$\mu_n := 1010 \qquad \mu_p := 95 \qquad x_p := 1.0 \cdot 10^{-4} \qquad l := 4 \cdot 10^{-3}$

$D_n := \mu_n \cdot \frac{kb \cdot T}{q} \qquad D_n = 24.653 \qquad L_n := \sqrt{D_n \cdot \tau_n} \qquad L_n = 4.196 \cdot 10^{-4} \qquad \frac{1}{L \cdot W} = 601.504$

$\sigma_p := q \cdot \mu_p \cdot 10^{18} \qquad \frac{1}{\sigma_p} = 0.066$

$I_L(Efn) := q \cdot L \cdot W \cdot D_n \cdot \frac{n_c(Efn)}{x_p} \qquad \frac{I_L(Efn)}{L \cdot W} = 27.936$

$L_{nf} := 2 \cdot \frac{kb \cdot T}{q} \cdot \frac{\sigma_p}{\frac{I}{L \cdot W}} \qquad L_{nf} = 1.234 \cdot 10^{-3}$

$J_L(Efn) := q \cdot D_n \cdot n_c(Efn) \cdot \sqrt{\frac{1}{L_n^2} + \frac{1}{L_{nf}^2}} \cdot \coth\left(x_p \cdot \sqrt{\frac{1}{L_n^2} + \frac{1}{L_{nf}^2}}\right) + \frac{1}{L_{nf}} \qquad 1 - \frac{J_L(Efn) \cdot L \cdot W}{I} = 0.949 \qquad J_L(Efn) = 30.788$

Appendix C – Optical Confinement Factor Calculation

$\lambda_0 := 1.3 \cdot 10^{-6}$ $\eta_{well} := 3.4824$ $\eta_{bar} := 3.3069$ $\eta_{clad} := 3.206$

$k_0 := \frac{2 \cdot \pi}{\lambda_0}$ $t_{well} := 0.005 \cdot 10^{-6}$ $t_{bar} := 0.01 \cdot 10^{-6}$

$$\eta := \begin{bmatrix} \eta_{clad} \\ \eta_{bar} \\ \eta_{well} \\ \eta_{bar} \\ \eta_{well} \\ \eta_{bar} \\ \eta_{well} \\ \eta_{bar} \\ \eta_{well} \\ \eta_{bar} \\ \eta_{well} \\ \eta_{bar} \\ \eta_{well} \\ \eta_{bar} \\ \eta_{clad} \end{bmatrix} \qquad w := \begin{bmatrix} 0.8 \cdot 10^{-6} \\ 0.12 \cdot 10^{-6} \\ t_{well} \\ t_{bar} \\ t_{well} \\ t_{bar} \\ t_{well} \\ t_{bar} \\ t_{well} \\ t_{bar} \\ t_{well} \\ t_{bar} \\ t_{well} \\ 0.12 \cdot 10^{-6} \\ 1.0 \cdot 10^{-6} \end{bmatrix}$$

$N := 15$ $\Delta x := 0.005 \cdot 10^{-6} \cdot k_0$

$l := 0 .. N-1$ $i := 0 .. N-1$

$$x_i := \sum_{c=0}^{i} w_c$$

$$w_t := \sum_{l} w_l \qquad w_t = 2.12 \cdot 10^{-6}$$

$$maxpts := \frac{w_t \cdot k_0}{\Delta x} \qquad j := 1 .. maxpts - 2 \qquad maxpts = 424$$

$$V_{0,0} := \eta_0{}^2 - \frac{2}{\Delta x^2} \qquad V_{0,1} := \frac{1}{\Delta x^2}$$

$$V_{j,j-1} := \frac{1}{\Delta x^2}$$

$$V_{j,j} := \left| \begin{array}{l} T \leftarrow \eta_{N-1}{}^2 - \frac{2}{\Delta x^2} \ \text{ if } \frac{\Delta x}{k_0} \cdot (j+1) \le w_t + 10^{-15} \\ \text{for } c \in N-2, N-3 .. 0 \\ \quad \left| \begin{array}{l} T \leftarrow \eta_c{}^2 - \frac{2}{\Delta x^2} \ \text{ if } \frac{\Delta x}{k_0} \cdot (j+1) \le xi_c + 10^{-15} \\ T \end{array} \right. \\ T \end{array} \right.$$

$$V_{j,j+1} := \frac{1}{\Delta x^2}$$

$$V_{maxpts-1,maxpts-2} := \frac{1}{\Delta x^2} \qquad V_{maxpts-1,maxpts-1} := \eta_{N-1}{}^2 - \frac{2}{\Delta x^2}$$

$$ni2 := \text{eigenvals}(V) \qquad n_{low} := 3.2 \qquad n_{hi} := 3.4$$

$$n_{eff} := \left| \begin{array}{l} \text{for } c \in 0 .. maxpts-1 \\ \quad T \leftarrow \sqrt{ni2_c} \ \text{ if } \left[\sqrt{ni2_c} \ge n_{low} \cdot \sqrt{ni2_c} \le n_{hi} \right] \\ T \end{array} \right.$$

$$n_{eff} = 3.24048$$

$$maxV := \max(V)$$

$$U := \text{eigenvec}\left(V, n_{eff}{}^2\right) \qquad P_j := U_j \cdot \overline{U_j} \qquad maxU := \max(P)$$

$$\Gamma := \sum_j \left| \begin{array}{l} T \leftarrow \left(U_j\right)^2 \ \text{ if } V_{j,j} + \frac{2}{\Delta x^2} \ge \eta_{well}{}^2 - 10^{-10} \\ T \leftarrow 0 \ \text{ otherwise} \\ T \end{array} \right.$$

$$\frac{\Gamma}{6} = 9.14091 \cdot 10^{-3} \qquad \Gamma = 0.05485$$

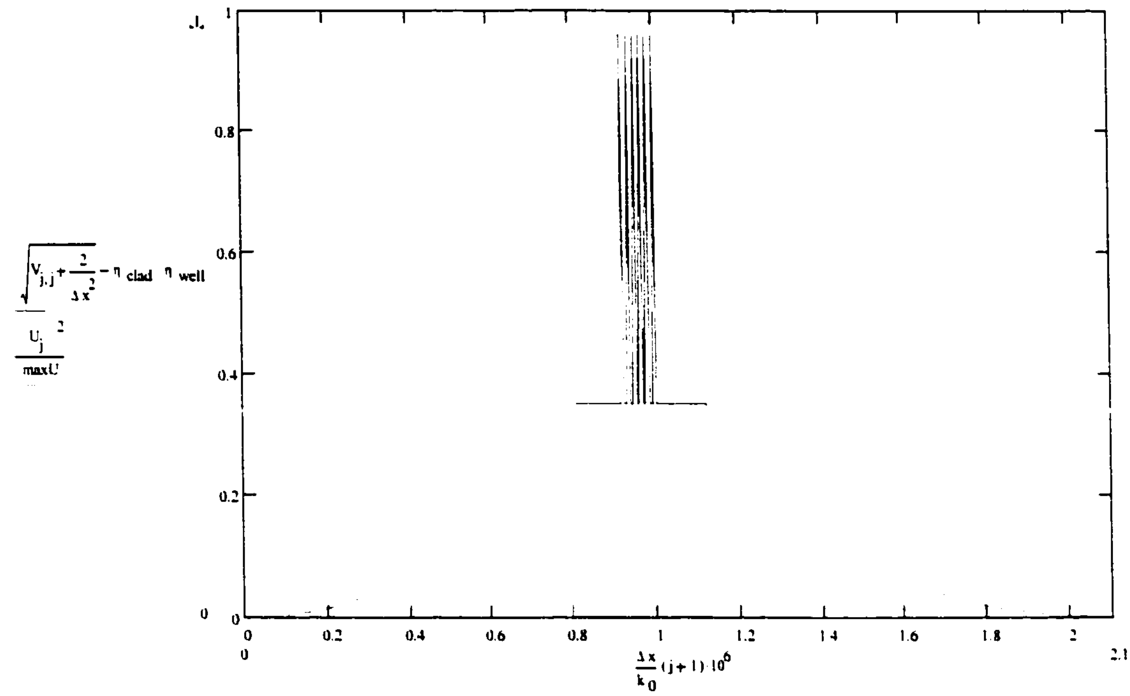

1
0.8
0.6
0.4
0.2
0
0
0.2
0.4
0.6
0.8
1
1.2
1.4
1.6
1.8
2
2.1